2013-09-04

A 500-1900 GHz Spectral Survey of the Orion South Star Forming Region from the Herschel Space Observatory

Tahani, Kianoosh

Tahani, K. (2013). A 500-1900 GHz Spectral Survey of the Orion South Star Forming Region from the Herschel Space Observatory (Master's thesis, University of Calgary, Calgary, Canada). Retrieved from https://prism.ucalgary.ca. doi:10.11575/PRISM/24628

http://hdl.handle.net/11023/908

UNIVERSITY OF CALGARY

A 500-1900 GHz Spectral Survey of the Orion South Star Forming Region from the Herschel Space Observatory

by

Kianoosh Tahani

A THESIS
SUBMITTED TO THE FACULTY OF GRADUATE STUDIES
IN PARTIAL FULFILLMENT OF THE REQUIREMENTS FOR THE
DEGREE OF MASTER OF SCIENCE

DEPARTMENT OF DEPARTMENT OF PHYSICS AND ASTRONOMY

CALGARY, ALBERTA

AUGUST, 2013

“Dedicated to my mother and
the memory of my father.”

Abstract

We will present initial results from a spectral survey toward Orion-S, taken by the HIFI instrument aboard the Herschel space telescope, in which we detect more than 800 spectral lines with $S/N > 3$ sigma originating from 47 different molecular and atomic species as well as a number of unidentified lines. Focusing on the transitions with $S/N > 5$ sigma we fit Gaussian line profiles to each of the observed transitions and have performed rotation/population diagram analysis for all the species for which we observed multiple transitions. This analysis provides us with the physical conditions, shows the presence of both warm (100 K) and cold (30 K) regions. A combination of population diagram analysis and the actual Local Thermodynamic Equilibrium modeling of the line profiles make us confident in the results of the molecular abundances, temperature, and other physical conditions in these two regions.

Acknowledgements

I would like to thank Dr Rene Plume, my supervisor, for accepting me into his research program and for his support and skilled guidance throughout the course of this project. I thank him for his patience not only with my education, but also with the changes in my personal life. During the last two years, Dr Plume has taught me how to research scientifically and how to interpret, write, and present the results. I would also like to acknowledge the individuals and HEXOS team who were integral to the completion of this work. I especially would like to thank Dr Emmanuel Caux for his email correspondence and generous offers of help regarding the CASSIS software package.

I wish to thank the other members of the Department of Physics and Astronomy for creating such a compelling learning environment. I especially would like to thank the main office staff who were supportive and friendly, giving the department an energetic atmosphere. I would also like to acknowledge my committee members who encouraged me to think about my research in a conceptual manner.

Last but not the least, I would like to especially thank my family who has always been supportive, within whom I learnt to love, to be curious, a hard worker and never fear a challenge.

Table of Contents

List of Tables

List of Figures and Illustrations

List of Symbols, Abbreviations and Nomenclature

Symbol	Definition
κ	Absorption coefficient
$\Delta\Omega$	Angular Size
λ	Wavelength
ν	Frequency
ϕ_ν	Gaussian line profile
ρ	Density
τ	Opacity
A_{ul}	Einstein A
B_{ul}	Einstein B
$B(T)$	Planck radiation
bg	Back ground
c_s	Speed of sound
c	Speed of light $2.9979 \times 10^8 ms^{-1}$
CI	One time ionized carbon transition
CII	Two times ionized carbon transition
CASSIS	Astrophysicist software package
CDMS	Cologne Database for Molecular Spectroscopy
CLASS	Astrophysicist software package
CNM	Cold Neutral Medium
dB	decibel
EOP	Emission in Off Position
FIR/submm	Far Infrared / sub-millimetre
FWHM	Full Width Half Maximum

G	Gravitational constant $6.674 \times 10^{-11} Nm^{-2}kg^{-2}$
GILDAS	Grenoble Image and Line Data Analysis Software
GMC	Giant Molecular Cloud
h	Planck's constant $6.6261 \times 10^{-34} Js$
HI	One time ionized hydroge transition
HII	Two times ionized hydroge transition
HEB	Hot Electron Bolometer
HEXOS	Herschel observation of Extra Ordinary Sources
HIFI	Hetrodyne Instrument for the Far Infrared
HIM	Hot Ionized Medium
HIPE	Herschel Interactive Processing Environment
HMSF	High Mass Star Formation
HSO	Herschel Space Observatory
IF	Intermediate Frequency
IR	Infra Red
IRAM	Institute for millimetric radio astronomy
ISM	Inter-Stellar Medium
j_ν	Emission coefficient
JPL	Jet Propulsion Laboratory
k	Boltzmann's constant $1.3807 \times 10^{-23} J/K$
K	Kelvin
LO	Local Oscillator
LMSF	Low Mass Star Formation
LSB	Low Side Band
LTE	Local Thermodynamic Equilibrium
$M_\odot$	One solar mass

M_J	Jean's mass
Myr	Million years
n_{crit}	Critical density
n	Number density
NAP	The national academic press
NIST	National Institute of Standards and Technology
o-	ortho
Obs	Observation
Orion-KL	Orion Kleinmann-Low
Orion-S	Orion South
OVRO	Owens Valley Radio Observatory
p-	para
PACS	Photodetecting Array Camera and Spectrometer
pc	Parsec $3.086 \times 10^{16} m$
PDR	Photo Dissociation Region
PWV	Precipitable Water Vapor
RF	Radio Frequency
rms	Root Mean Square
S_ν	Source function
SIS	Superconductor, Insulator, Superconductor
sys	System
T	Temperature
U	Unidentified
USB	Upper Side Band
V_{lsr}	Velocity with respect to the Local Standard of Rest
WIM	Warm Ionized Medium

WNM	Warm Neutral Medium
YSO	Young Stellar Object
$\mathcal{Z}$	Partition function

Chapter 1

Introduction

1.1 The Interstellar Medium, Giant Molecular Clouds, and Star Formation

Looking at the sky on a clear night we can see stars, but the sky is also full of interstellar matter in the form of dust and gas. The absence of stars in some dark patches of the Milky Way revealed the existence of the interstellar medium (ISM), which blocks starlight from more distant, background objects. 20-30 percent of the mass of our Galaxy is in the ISM which pervades the Milky Way (NAP[1] 2007). Generally speaking, the ISM is assumed to exist in four phases: Cold Neutral Medium (CNM) ($T < 300\ K,\ n = 10^3 - 10^6\, cm^{-3}$), Warm Neutral Medium (WNM) and Warm Ionized Medium (WIM)($T \sim 10^4\ K,\ n = 0.1 - 10\, cm^{-3}$) (Field, Goldsmith, and Habing 1968), and Hot Ionized Medium (HIM)($T = 10^6\ K,\ n = 0.003\, cm^{-3}$)(Mckee, and Ostriker 1977). Most of the space volume in the ISM is occupied by the hot ionized component while most of the mass is contained in the CNM which accounts for less than 10% of the ISM volume (Ferrire 2001). Giant Molecular Clouds (GMC) are assumed to be the coldest and densest regions of CNM, in which the hydrogen is primarily molecular in form, with the typical sizes of 40 pc in diameter, masses of $\sim 10^5 M_\odot$, densities of $\sim 200\ cm^{-3}$, and temperatures of $\sim 10\ K$. Molecular clouds are the sites of active star formation, and although they are complex and chaotic in form they are often simplified into smaller, denser subunits, referred to as clumps and cores. Table 1.1 lists the typical properties of molecular clouds, clumps and cores.

---

[1] The national academic press. www.nap.edu

[2] Cambresy 1999

[3] Loren 1989, and Williams, de Geus & Blits 1994

	Clouds [2]	Clumps [3]	Cores [4]
Mass($M_\odot$)	$10^3 - 10^4$	$50 - 500$	$0.5 - 5$
Size(pc)	$2 - 15$	$0.3 - 3$	$0.03 - 0.2$
Densitycm^{-3}	$50 - 500$	$10^3 - 10^4$	$10^4 - 10^5$
Temperature(K)	~ 10	$10 - 20$	$8 - 12$

Table 1.1: *Properties of clouds, clumps, and cores*

Stars are constantly being formed in galaxies by the repeated gravitational condensation from the ISM (Goldeich & Kwan 1974). Studying molecular clouds and extracting the physical conditions in molecular clouds, such as temperature, density, size scale, mass, and etc., should provide us the key to understanding how GMCs themselves form and where and how star forming structures form within them. The formation of a GMC takes place at very modest densities, and due to uncertainties in the magnetic field strength and the importance of the turbulence motions,two opposite views of the formation process exist. One view indicates that clouds can be assumed in almost equilibrium so their evolution toward star formation is quasi static and taking at least $10Myr$. However, a more recent view supports the idea that clouds are more dynamic and form stars in a transient time, $3 - 5Myr$. One critical time scale is that for conversion of HI to H_2, which for a density of 100 cm^{-3} is $3 \times 10^7 yr$ (goldsmith and Li 2005). The complete process of cloud formation through star formation is likely dominated by the time required to form the GMC, and the initial density inhomogeneities within it. One of the most significant discoveries by the Herschel Space Observatory is that the dominant form of the structures within GMCs is filamentary. These structures are observed in atomic and molecular gas, as well as dust. The filaments will, at some point, become unstable to perturbations, which lead to formation of higher density cores spaced along the filament's axis. This has been supported observationally and numerically (Andre et. al. 2010, Arzoumanian et. al. 2011). These "dense cores are the sites of young stars. The formation of these high density structures within the extended

---

[4] Jijina, Myers & Adams 1999, Caselli et al. 2010, and Motte, Andre & Ner 1998

cloud is a critical step in the star formation process.

Although gravitational collapse explains, in the most basic sense, how stars are formed, the details of the process of star formation are still uncertain and depends critically on the physical conditions in the core. Extracting the detailed physical conditions in dense cores can provide us the key to understanding the mass of the resulting star, the mass that winds up in a disk around the star, and also why in some regions only a few lightly cluster stars form and in other places a tight grouping of stars form instead (Crovisier 1999, van Dishoeck & Blake 1998).

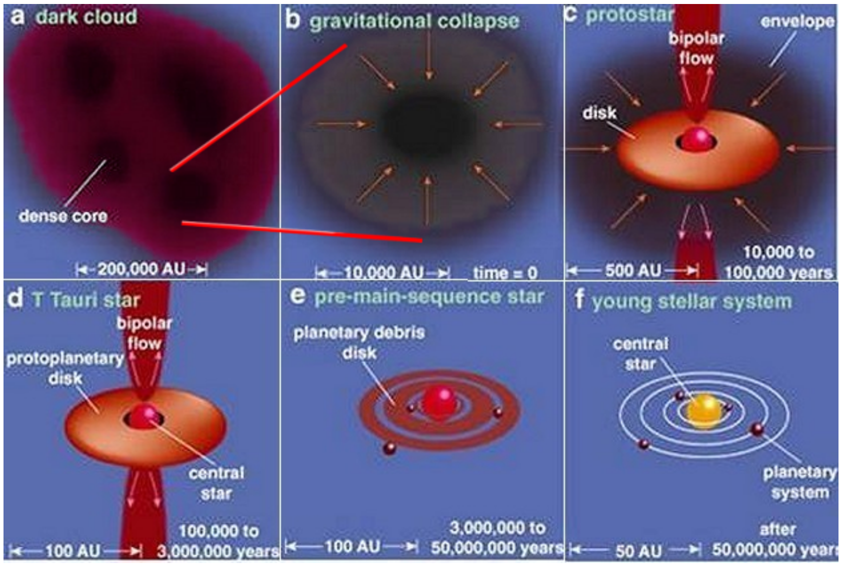

Figure 1.1: *Evolution of a young low mass star. Figure by Spitzer Science center.*

However, a simplified, cartoon version of the star formation process is presented below and in figure 1.1.

- a. Inside the molecular cloud a few dense cores are formed.

- b. The high density core becomes unstable, this is defined as t=0. The rotation of the system causes a flattening the core due to angular momentum.

- c. Gravitational collapse converts potential energy into kinetic energy, which causes the cloud to heat up. About 10^4-10^5 years after the start of collapse the core's density becomes so high that the radiation from the central core can no longer escape into the space. This causes the surrounding cloud to heat up more quickly than before due to the trapping of radiation. At this stage, the protostar radiates primarily in the IR range. While dust and gas collapse toward the center, angular momentum causes the surrounding material to form an accretion disk. Excess angular momentum dissipates via a highly collimated outflow.

- d. At this stage most of the surrounding envelope gas has accreted onto the disk, and the central star is almost at its final mass.

- e. At the age of 10^6-10^7 yr the young star reaches the hydrogen fusion phase.

- f. At this stage the accretion disk has been evaporated and the young main sequence star is surrounded by a planetary system.

The time scale for the gravitational collapse of a dense core due to the free fall in the absence of any other forces to oppose the collapse is given by the "free fall time" (Binney & Tremaine 1987);

$$t_{ff} = \sqrt{\frac{3\pi}{32G\rho}} \tag{1.1}$$

where ρ is the density and G is the gravitational constant, $6.674 \times 10^{-11} Nm^{-2}kg^{-2}$. Since the free fall time is collapse to the center, the time scale needed to establish pressure balance against free fall can be simplified to the time it takes for a sound wave to reach the center (at which point it will push back to re-establish the pressure). If we assume the cloud is a homogeneous sphere, this can be written as:

$$t_{sound} = \frac{R}{c_s} \tag{1.2}$$

where R is the radius of the cloud and c_s is the speed of sound. Whenever $t_{ff} < t_{sound}$ collapse will occur. The Jeans length, λ_J can be defined as the critical radius where the cloud starts to collapse, $t_{ff} = t_{sound}$. By using equations 1.1 and 1.2 we can show that:

$$\lambda_J \propto \frac{c_s}{\sqrt{G\rho}} \tag{1.3}$$

knowing $m = \rho V$ we can also show that the Jeans mass criterion for collapse is:

$$M_J \propto \frac{c_s^3}{G^{3/2}\rho^{1/2}} = \left(\frac{kT}{G}\right)^{3/2} \frac{1}{m^2\, n^{1/2}} \tag{1.4}$$

the last term is substituted by using $c_s = (kT/m)^{1/2}$ and $n = \rho/m$ where m is the mass of the typical constituent particles of the cloud, k is the Boltzmann constant, T is the temperature of the cloud and n is the particle density.

The physical conditions in interstellar gas (clouds, clumps, and cores) also give rise to a wide variety of complex chemical conditions. Prior to star formation, the chemistry of the cores is dominated by low temperature gas-phase ion-molecules and neutral-neutral reactions leading to the formation of small radicals and unsaturated molecules. During the collapse phase, when the density is high, molecules accrete onto dust grains and form an icy mantle (Hollenbach & Tienlens 1997), which can, itself, undergo further chemical reactions (known as grain-surface reactions). A wide variety of different molecules are detected in the ISM. As of October 2012, more than 150 molecules, from simple diatomic molecules to a long carbon chains or organic molecules, have been detected unambiguously in the interstellar medium or circumstellar shells (NASA[5]). How this complexity develops, however, is uncertain.

1.2 High-Mass Star Formation (HMSF)

High mass stars are usually defined as stars of mass $\sim 8M_\odot$ or higher. The $\sim 8M_\odot$ threshold is important since a star of this mass has already begun hydrogen burning before the accretion stage is finished. In addition, at this mass the peak of black-body radiation is shifted into the UV regime so the photons are energetic enough to ionize the surrounded ISM (forming an HII region) (Palla & Stahler 1993; Cesaroni 2005).

Studying HMSF is more challenging since only 1% of stars have masses more than $10M_\odot$ and their formation time scale is shorter by at least a factor of 10. Thus, they are statistically rare and hard to find in their early evolutionary stages (Zinnecker & Yorke 2007). However, the study of high-mass stars is important from a global prospective, since the luminosity, energetics, and heavy element production of the Milky Way (and many galaxies) is dominated by high mass stars.

The details of how high-mass stars form is still uncertain, mainly due to the theoretical difficulties understanding the feedback effects of radiation pressure and protostellar winds on the formation process and the fact that, observationally, we do not yet have statistically relevant samples which provide insight into the numbers, locations, environments, and physical and chemical conditions of high mass star forming regions. The following three scenarios have been proposed on how high-mass stars are being formed:

---

[5] //science.gsfc.nasa.gov/691/cosmicice/interstellar.html

1. *Monolithic collapse*, which is basically a scaled-up version of low-mass star formation in which the accretion rate is believed to be high enough to overcome radiation pressure due to higher pressures believed to exist in the environments of HMSF regions. In this model a single massive star can be formed from a single massive protostellar core (observationally by Plume et. al. 1997 and theoretically Henrik Beuther et. al. 2006).

2. The idea of *competitive accretion* scenario, arises due to the fact that most stars do not form in isolation but in binary stars or cluster stars, and massive stars tends to form in clustered environments. The separation between stars in clusters are usually less than the size of an accreting envelope, so in order for stars to form they must compete for the reservoir of materials. In such clusters each massive protostar increases mass and eventually compete to accrete rest of gas within the neighbouring protostars (Bonnell et al. 2001).

3. *Stellar mergers* have been also proposed, since HMSF is hampered by radiation pressure (Bonnel & Bate 2005). This involves the merger of lower-mass stars in a dense cluster. Thus, in this model massive stars are formed through stellar collision.

1.3 Goals of this thesis - A spectral survey of Orion-South a HMSF region

To undertake this project we use data from the HEXOS (Herschel observation of EXtra-Ordinary Sources) key project (Bergin et al. 2010). A part of the HEXOS key project is to observe Orion-South (Orion-S), to contrast with the high-excitation Orion-KL source. Orion-S is a high-mass star formation region with a more quiescent nature than Orion-KL. Observations toward Orion-S shows the infrared luminosity is different by an order of magnitude with Orion-KL (Genzel & Stutzki 1989). Studying Orion-KL, i.e modelling and extracting the physical conditions, is a significantly more complicate problem since it is so active and we observe around 100,000 transitions. Thus, studying Orion-S should be a simpler problem since there is less line confusion, since the lines are narrower, fewer, and weaker. In addition, studying Orions-S may allow us to study the star formation process in the Orion nebula at an earlier evolutionary stage and compare the chemical composition and physical conditions with that of KL which is a more evolved star forming region.

Orion-S is a highly active star formation region located about $100''$ south of Orion-KL region (a well known star formation region), see figure 1.2. A highly collimated CO outflow, with the length of 0.07 pc and velocities of $-140\,km\,s^{-1}$ toward north-west and $88\,km\,s^{-1}$ to the south-east, centred at the $R.A = 05^h35^m13.550^s$, and $decl. = -05^\circ23'59.14''$ (J2000) within Orion-S ($40'' \times 40''$) suggest that Orion-S should be a site of star formation (Zapata et. al. 2005). Also other powerful molecular outflows have been observed such as an SiO outflow (Ziurys et al. 1990) and another bipolar CO outflow (Zapata et al 2004a, 2004b) correspondingly at low velocities of 10 $km\,s^{-1}$ and 5 $km\,s^{-1}$. All of these are signposts of early stage, embedded star formation.

In Orion-S we wish to obtain the chemical inventory of a known massive star forming region and determine its physical and chemical nature. The ultimate goal of this project (although outside the scope of this thesis) is to compare the chemistry and physical conditions of Orion-S to other low mass star forming regions at similar evolutionary stages, i.e. are there chemical signature of high versus low mass star formation? Furthermore, we can

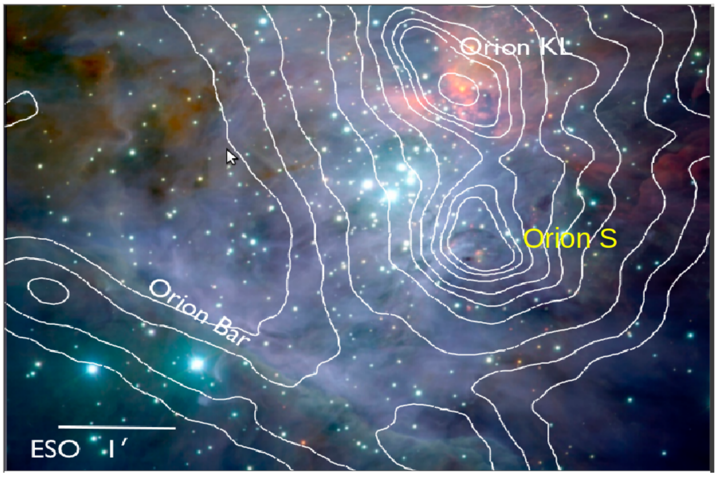

Figure 1.2: *The picture over lay the optical picture of Orion nebula with the* 350μm *map of Orion, which shows the position of Orion-KL, Orion-S, and Orion bar. Figure by R. Plume, private communication.*

take an additional step forward and compare it to other high mass star formation regions in different evolutionary stages, i.e. are there chemical signature of the age of a star formation region?

Data for this thesis were taken with the Herschel Space Observatory (HSO). The HSO is the largest (3400 kg) infrared space telescope ever launched. It has also got the largest single mirror ever built for a space telescope (3.5 metres). Herschel is designed to operate at Far InfraRed (FIR) and Submillimeter (submm) wavelengths and to collect radiation from the coldest and most distant objects in the Universe. The HSO launched in May 2009 and is located at the second Lagrangian point (L2) of the Earth-Sun system, 1,500,000 km away from Earth. The mission recently ended (April 2013) when Herschel ran out of cryogens. My data comes from HIFI instrument (Heterodyne Instrument for Far Infra-red) abroad HSO which provides a high resolution spectral survey 400 - 1900 GHz. This instrument will be discussed in more detail in the next chapter.

1.4 Why do we need a space telescope?

A wide wavelength range of electro-magnetic radiation coming from space is blocked by our atmosphere. Although this phenomena is essential for the existence of life on our planet, if we want to better study our Universe we need to get above Earth's atmosphere. In order to study the process of star formation and the molecular clouds in which star formation occurs, the optimal wavelength range is the Far Infrared (50-1000μm) and sub-millimeter (0.1-1 mm). One may ask, though, why is FIR/sub-mm important?

The primary composition of the ISM is gas and dust. Although dust only makes up about one percent of the ISM mass, it plays an important role in the ISM (Kwok 2007). In the early stages of star formation the gas and dust temperatures are 10-30K (Romanini 2007). If dust emits as a black body, then *Wien's law* gives us the peak wavelength of the emission:

$$\lambda\,(cm) = \frac{0.2898}{T(K)} \tag{1.5}$$

However, due to the size of the dust grains and the wavelength of the radiation being emitted and absorbed, dust grains do not radiate as a true black body. As a result, we need to multiply the Plank function by an efficiency factor:

$$Q(\lambda) = Q_0(\frac{\lambda_0}{\lambda})^{\beta} \tag{1.6}$$

where Q_0 and β are constants and λ_0 is a reference wavelength.The key point is that this coefficient is proportional to $\lambda^{-\beta}$ and, therefore, we can calculate $\partial(\lambda^{-\beta}B_\nu)/\partial(\lambda) = 0$ to find the λ_{Max} for a modified black body; substituting $x = hc/\lambda kT$ in the Plank function:

$$B_\lambda = \frac{2hc^2}{\lambda^5}\frac{1}{e^{hc/\lambda kT} - 1} \tag{1.7}$$

and performing the differentiation to find λ_{Max} results in:

$$\frac{xe^x}{e^x - 1} = 5 + \beta \tag{1.8}$$

which leads us to Wiens law for a modified black-body:

$$\lambda_{Max}(cm) = \frac{0.2898}{T(K)} \frac{5}{5 + \beta} \tag{1.9}$$

Typically β is assumed to be between 1 and 2. For $\beta = 1$, $Q_0 = 1$ and $\lambda_0 = 2\pi a$, where a is the radius of dust, this equation is simplified. Also due to the Lorentz oscillator, it is physically reasonable to assume $\beta = 2$ for long wavelengths.(V. Ossenkopf and Th. Henning 1994) So if we assume $\beta \approx 1.5$, we can show that for a temperature range of 10-30K (typical of GMCs), the dust emits most of its radiation in the wavelengths range of $70 - 200\mu m$.

At these wavelengths, however, water vapor in the Earth's atmosphere is an excellent absorber. So a dry site at high elevation, such as Mauna Kea in Hawaii at an elevation of 4200 m, is a good location for a sub-mm telescope since it is above much of the water vapor in the atmosphere. As Figure 1.3 shows, even an excellent ground-based site like Mauna Kea is not sufficient to access the peak of the Spectral Energy Distribution (SED) from cold interstellar dust radiating as a modified black body.

In order to see how the atmosphere affects incoming radiation from space, we define a general concept in astrophysics; opacity (or optical depth), τ, as:

$$\tau = -\int_{0}^{L} \kappa \, \mathrm{d}s \tag{1.10}$$

where κ is the absorption coefficient, L is the total distance the wave travels through the cloud, in our case the atmosphere, and ds is the element of length.

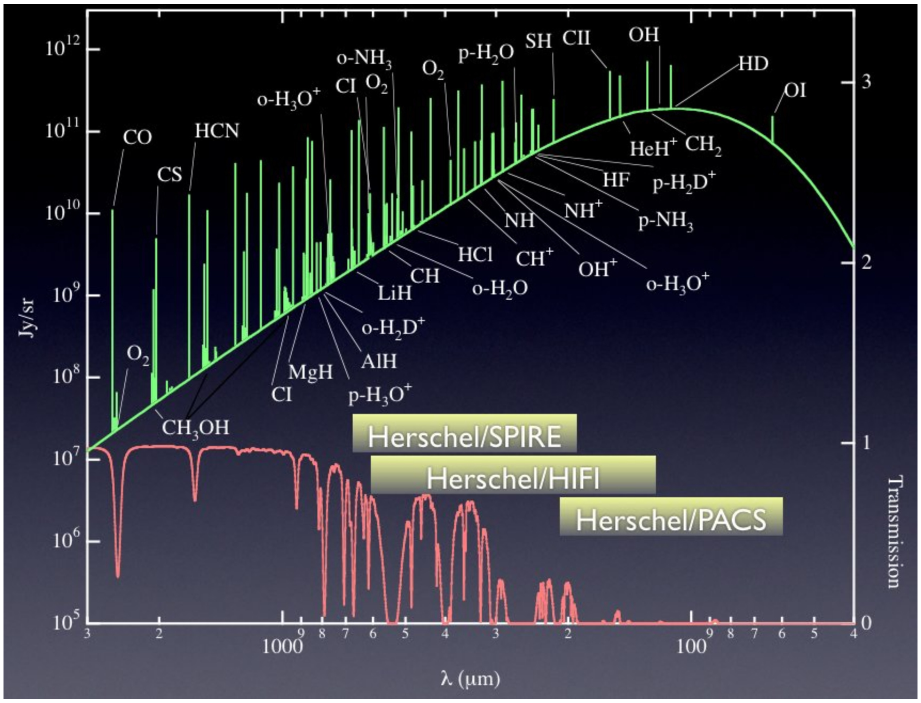

Figure 1.3: *The green graph is the Spectal Energy Distribution (SED) of cold interstellar dust, upon which is superimposed a model of emission frequencies for some important molecular and atomic species. The red graph is atmosphere transmission on Manua Kea, which shows the transparency of the atmosphere at a high dry location. This figure clearly shows that to observe many of the key species, and to access the peak of the SED for cold dust, an even better site than Mauna Kea is required. Fig from E. Bergin private communication.*

We define the emission coefficient, j_ν, as the amount of energy emitted per unit time per unit volume per solid angle per frequency, so the change in intensity due to the cloud's emission is:

$$\mathrm{d}I_\nu = j_\nu \mathrm{d}s \tag{1.11}$$

Similarly the change in the intensity due to the cloud's absorption is:

$$\mathrm{d}I_\nu = -\kappa_\nu I_\nu \mathrm{d}s \tag{1.12}$$

where the κ_ν term shows the dependence of κ on frequency. So the total change in intensity is:

$$\mathrm{d}I_\nu = j_\nu \mathrm{d}s - \kappa_\nu I_\nu \mathrm{d}s \tag{1.13}$$

$$\frac{\mathrm{d}I_\nu}{\kappa_\nu \mathrm{d}s} = -I_\nu + \frac{j_\nu}{\kappa_\nu} \tag{1.14}$$

The ratio of the emission and absorption coefficients is defined as the *source function*:

$$S_\nu \equiv \frac{j_\nu}{\kappa_\nu} \tag{1.15}$$

and substituting for opacity we obtain the well-known *equation of transfer*:

$$\frac{\mathrm{d}I_\nu}{\mathrm{d}\tau_\nu} = I_\nu - S_\nu \tag{1.16}$$

If we assume S is constant, the general solution is written as:

$$I = I_{bg}e^{-\tau} + S(1 - e^{-\tau}) \tag{1.17}$$

where I is what we receive and, I_{bg} is the background radiation passing through cloud. The first term on the right side of equation 1.17 shows the attenuation of the background radiation after passing through the cloud. The second terms provides the radiation produced by the cloud itself.

We can apply this result to study the observed intensity on Earth. By taking into account the angle of incident radiation and assuming $S = 0$,(i.e. that the atmosphere does not contribute any radiation), we can show:

$$I_{Obs} = I_* e^{\frac{-\tau}{Cos(\theta)}} \tag{1.18}$$

where I_{Obs} is the intensity we observe on the ground, I_* is source intensity above the atmosphere and θ is the angle to zenith.

To see how important the water vapor is in affecting the transparency of the atmosphere we define the Precipitable Water Vapor (PWV), which is the depth of water in a column of the atmosphere if all the water in that column were precipitated as rain. PWV is directly related to τ which, in turn, is directly related to the column density of water. There are a number of sophisticated models, however, which can translate PWV into a wavelength dependent τ which allows us to plot opacity and, thus, atmospheric transmission, $e^{-\tau}$, as a function of frequency.

Figure 1.4 shows the results of one of these models for, PWV=4 mm and PWV=1 mm, and shows water vapor in the atmosphere is as an absorber of radiation. Therefore in order to observe some frequencies, especially those that are critical to the study of cold interstellar dust, we have to get above the atmosphere.

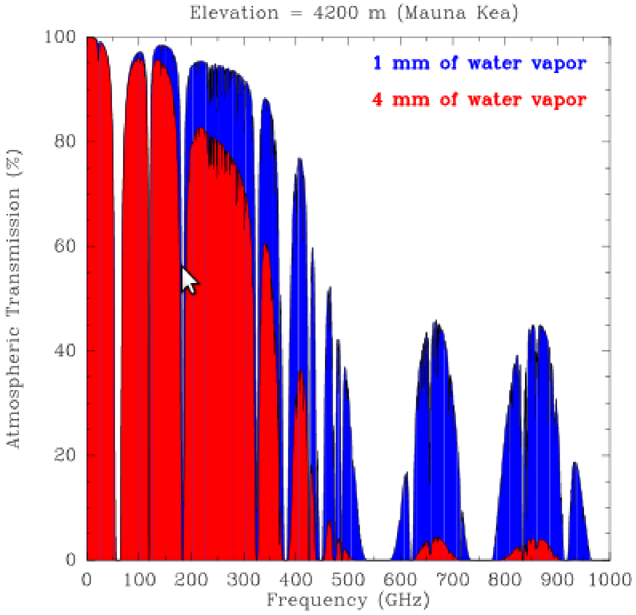

Figure 1.4: *Atmospheric transparency at Manua Kea, PWV=4 and PWV=1. Fig from Vastel: IRAP; Toulouse*

1.5 Interstellar Molecules

Dust is not the only component of the ISM, 99% of the mass resides in gas which, as Figure 1.3 shows, contains both atomic and molecular components. In the late 1930s the first interstellar molecules were discovered via absorption lines seen against the background starlight. The very first molecules were CN (λ =3876.84 $\mathring{A}$), CH (λ =4300.30 $\mathring{A}$) and CH^+ (λ =4232.54 $\mathring{A}$) (W.S. Adams 1943). In the 1950s because of the improvement of radio receivers, a new range of spectroscopy was available to astrophysicists. With the development of millimetre wave receivers, the rotational transitions of many molecules were detected, where the first detections were CO (λ =2.6 mm) and hydrogen cyanide(HCN λ =3.4 mm). As Figure 1.3 shows, the FIR/Submm wavelength regime is where a significant number of molecular and atomic species produce emission lines. At these wavelengths, these lines are usually rotational transitions for molecules and fine structure lines for atoms.

Studying the molecular and atomic emission lines in the FIR/submm, not only provides us with an inventory of the chemical complexity in the ISM, it also provides clues to the physical condition in the gas (such as abundance, density, temperature, etc.). This will be discussed thoroughly in the next chapters.

Summary

We wish to obtain the chemical inventory and to extract the physical conditions in Orion S, a relatively nearby, quiescent, and young massive star formation regions using data from Herschel/HEXOS. In chapter 2 we will describe the observations and how the Hetrodyne technique is used by the HIFI instrument aboard HSO to provide a high resolution spectra. We will also describe the basic data reduction procedure. In chapter 3 we will describe how we perform the line identification and will list all the identified species and transitions. In chapter 4 we will discuss different methods we used to extract the physical conditions, e.g. temperature, source size, density, etc., in Orion-S, compare the results of these methods and finally, provide calculations of the column density, temperature, and size of the emitting regions for each of the detected species.

Chapter 2

Observations

2.1 Heterodyne Spectroscopy

The problem with a regular, i.e a direct detection, spectrometer is that the spectral resolution (λ/L where L is the size of spectrometer) is limited by the size of the spectrometer and the wavelength of the radiation. At near IR and mid IR wavelengths (2 - 20 microns) the best modern direct-detection spectrometers provide spectral resolutions of 350 to 25000[1]. Even Herschel's spectrometer (PACS) only has a resolution of 940-5500[2] . Given that emission lines in the cold, dense ISM associated with star formation are often less than 1 km/s in width, clearly these direct detection techniques do not allow us to resolve the lines since the best velocity resolution for PACS is 55 $km\ s^{-1}$.

At FIR/submm wavelengths direct detection spectrometers become unfeasible, partly due to the required size of such a spectrometer and partly due to the difficulty of directly detecting and amplifying these low energy photons. At these frequencies (100's of GHz to THz), signals must often be amplified by 15-20 dB or more and it is technologically challenging to build low noise amplifiers that work well at such high frequencies. In addition, if there is any kind of internal reflection/impedance mismatch in the optical path, the internal reflection signal is also amplified and interferes with the incoming signal. One solution to these problems is to build a Heterodyne receiver.

The heterodyne technique is an application of the simple idea of "beat frequency". A Het-

---

[1] http://www.eso.org/public/teles-instr/vlt/vlt-instr.html

[2] http://herschel.esac.esa.int/Docs/PACS/html/ch04s07.html

rodyne receiver essentially combines the incoming Radio Frequency (RF) with a frequency close to the frequency to be detected called the Local Oscillator (LO) to produce a beat frequency (called the intermediate frequency or IF) which is lower in frequency and easier to amplify. In addition, since the IF is very different from the incoming RF, neither the RF nor any internal reflections in the RF get amplified. (Wilson T.L, Rohlf K,& Huttemeister S 2009, Chapter 5)

The actual mixing of these two signals is accomplished by using a device that operates as a "square-law detector" in which $I(V) = \alpha.V^2$, where I is the current and α is a constant and V is the voltage. As a simple example we can study the combination of two sinusoidal waves, where for simplicity we assume they have the same phase:

$$\begin{aligned} V_{RF} &= V_{RF} sin(2\pi\nu_{RF}t) \\ V_{LO} &= V_{LO} sin(2\pi\nu_{LO}t) \end{aligned} \tag{2.1}$$

Therefore, the current will be:

$$\begin{aligned} I = {} & \alpha[V_{RF} sin(2\pi\nu_{RF}t) + V_{LO} sin(2\pi\nu_{LO}t)]^2 \\ = {} & \alpha[\tfrac{V_{RF}^2}{2} + \tfrac{V_{LO}^2}{2}] && \text{(DC component)} \\ & -\alpha\tfrac{V_{RF}^2}{2} cos(4\pi\nu_{RF}t) && \text{(2nd harmonic of RF)} \\ & -\alpha\tfrac{V_{LO}^2}{2} cos(4\pi\nu_{LO}t) && \text{(2nd harmonic of LO)} \\ & +\alpha V_{RF}V_{LO}\{cos[(2\pi\nu_{RF} + 2\pi\nu_{LO})t]\} && \text{(sum frequency)} \\ & +\alpha V_{RF}V_{LO}\{cos[(2\pi\nu_{RF} - 2\pi\nu_{LO})t]\} && \text{(frequency difference)} \end{aligned} \tag{2.2}$$

If we send this signal through a low-pass filter centered on the beat frequency (hereafter called the intermediate frequency or IF):

$$\nu_{IF} = |\nu_{RF} - \nu_{LO}| \tag{2.3}$$

We can eliminate the high frequency terms and, therefore, amplify and sample a much lower frequency than the original, RF.

2.1.1 Upper Side Band (USB) and Lower Side Band (LSB)

By using eq. 2.2 and eq. 2.3, we can define the IF band, $\Delta\nu_{IF}$, as:

$$\nu_{IF0} + \Delta\nu_{IF} = \pm[\nu_{LO} - \Delta\nu_{RF}] \tag{2.4}$$

$\Delta\nu_{IF}$ defines the frequency width of the IF bandwidth which is a characteristic of the mixer detector, it covers the range of frequency from ν_{IF0} to $\nu_{IF0} + \Delta\nu_{IF}$, where ν_{IF0} is the beginning of IF band, and $\Delta\nu_{RF}$ is the range of RF frequency can be changed so that we are still in IF band.

As eq. 2.4 shows there are two different RF ranges that can fit into the same IF band, $\nu_{LO} - \Delta\nu_{RF}$ when $\nu_{LO} > \nu_{RF}$ this is called LSB and $\Delta\nu_{RF} - \nu_{LO}$ when $\nu_{RF} > \nu_{LO}$ which is called USB. Consequently we are actually simultaneously detecting RF frequencies from $\nu_{LO} - \nu_{IF0}\ to\ \nu_{LO} - \nu_{IF0} - \Delta\nu_{IF}$, LSB, and also from $\nu_{LO} + \nu_{IF0}\ to\ \nu_{LO} + \nu_{IF0} + \Delta\nu_{IF}$, USB, this is called a Dual Side Band(DSB) receiver. To see how the DSB detectors work, we suppose the characteristic of the mixer is: $\Delta\nu_{IF} = 4\ GHz$, $\nu_{IF0} = 3\ GHz$, and $\nu_{LO} = 1000\ GHz$. It means the USB RF range we can detect is 1003-1007 GHz and the LSB RF range is 993-997 GHZ, Fig. 2.1 shows this graphically.

The Hetrodyne technique down-converts the USB and LSB frequency range to the IF band, as shown in Fig. 2.1, to provide us a high resolution spectra at a lower IF frequency which is easier to amplify. However to analyze the content in the spectrum we need to know

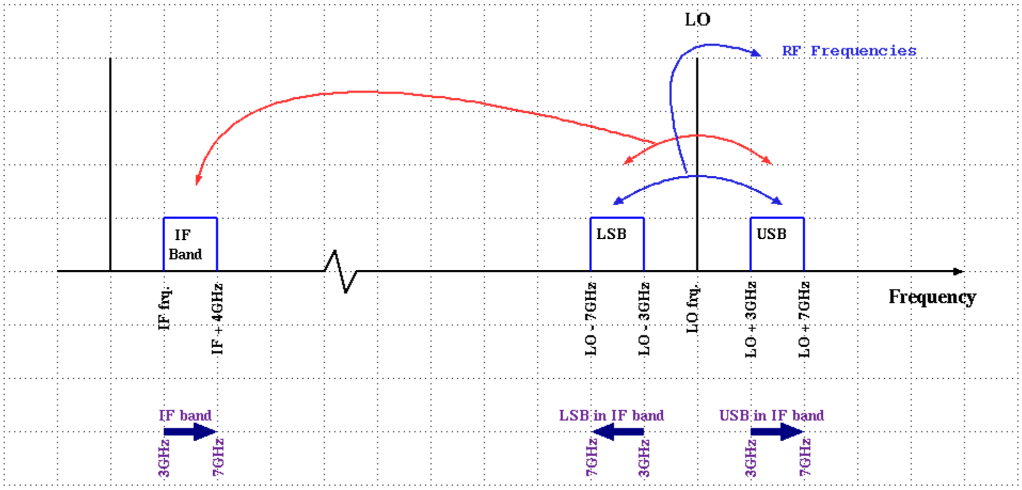

Figure 2.1: *Conversion from high frequency, RF, to low frequency, IF. The direction of the arrows shows how the LSB and USB appear in the IF band.*

which RF frequency an observed spectral line comes from. Figure 2.2 shows how RF frequencies from USB and LSB overlap into the IF band. In order to have the right frequency in our final spectra we need to be able to identify which observed line in the IF is coming from which RF frequencies, LSB or USB. As is shown in Fig. 2.1 the USB frequency range has a different direction (higher to lower frequencies) in the IF than the LSB does (lower to higher frequencies). This characteristic of DSB detectors provides the key to determine the exact incoming frequency of an observed line, in which by shifting the LO frequency causes line profiles from the USB to move in the opposite direction to the LSB lines. Arrows in Fig 2.3 shows how we can distinguish among USB and LSB lines, where by shifting LO frequency slightly higher one the LSB lines should move toward the end of IF band whereas USB lines should move toward the other end of the IF band. This is the key to mapping the right RF frequencies into the IF band.

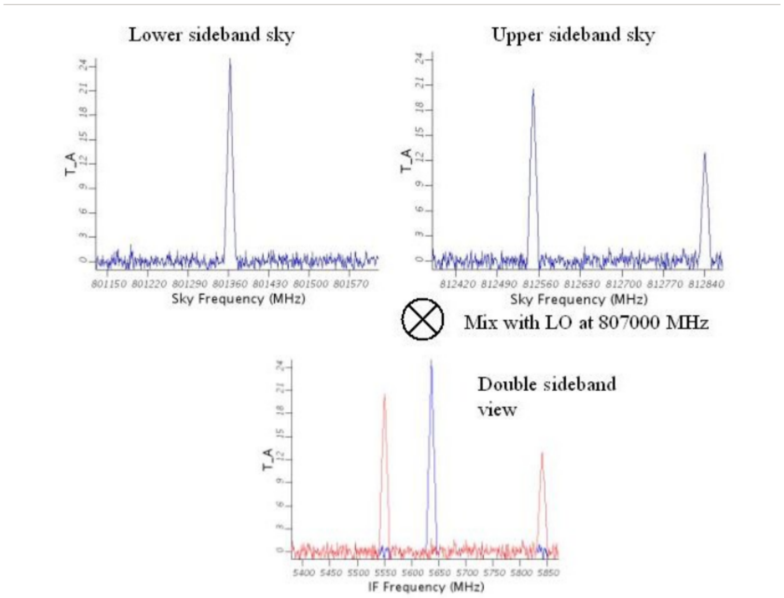

2.2: *Superposition of upper(red in double side band view) and lower (blue in double side band view). Sideband spectra in a portion of a single DSB spectrum crudely based on Orion cloud spectra taken at 807.0GHz. Figure from HIFI Observer's Manual, ver. 20.4*

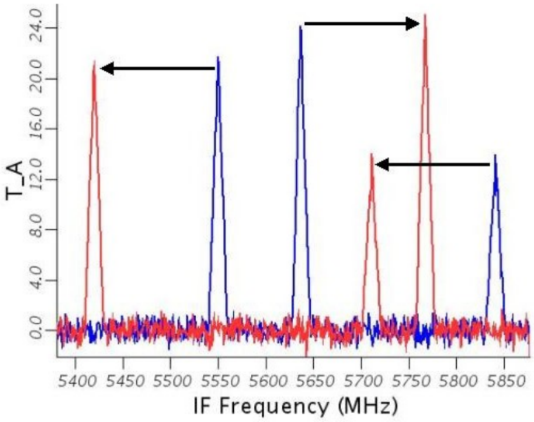

2.3: *Superposition of two separate DSB spectra in blue and red taken at 807.0GHz and 807.13GHz respectively. Note how the largest line from the lower sideband goes up in the IF band frequency when the LO frequency is increased (compare the previous figure), while the other two lines from the upper sideband go in the opposite direction. In all cases the frequency shift is 0.13GHz, the same as the LO frequency change between the two observation. Figure from HIFI Observer's Manual, ver. 20.4*

2.2 The Heterodyne Instrument for the Far Infrared (HIFI)

The data presented in this thesis were all taken by the Heterodyne Instrument for the Far-Infrared (HIFI), which is one of three instruments aboard the Herschel Space Observatory. HIFI operates over the frequency ranges 479-1901GHz with independent horizontal and vertical polarization and has a spectral resolution, $\lambda/\Delta\lambda$, 10^6 to 10^7. HIFI uses both SIS and HEB mixers to cover the desired frequency range as described below (Roelfsema et. al. 2010).

An SIS (Superconductor-Insulator-Superconductor junction) mixer is composed of superconductors sandwiching a thin layer of insulator, which uses the quantum tunneling effect to pass current through this thin region. The theoretical current-voltage diagram of SIS junction is shown in Fig. 2.4. As it is shown in this figure, if the bias voltage to be set at $2\Delta/e$, the knee of the graph, an incoming photon will create a large change in current, this is a non-linear I-V relation. In order to use this effect we need to bias the SIS junction at this critical voltage, this is shown on the voltage diagram in Fig. 2.5. Once one side of the SIS junction is set to the corresponding voltage to the energy gap, Δ, it fulfills our demand.

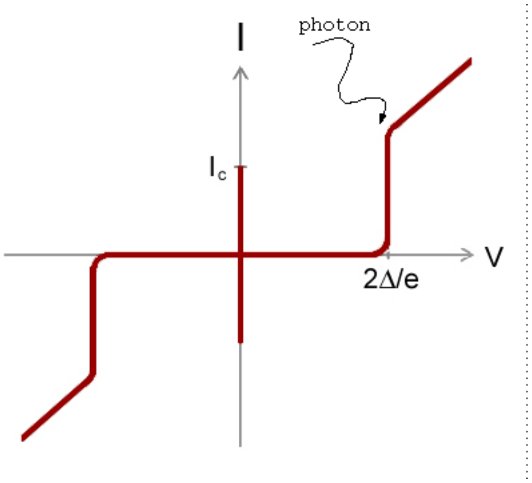

Figure 2.4: *I-V curve of the SIS non-linear junction.*

Superconducting hot electron bolometers are very promising mixer technology for THz

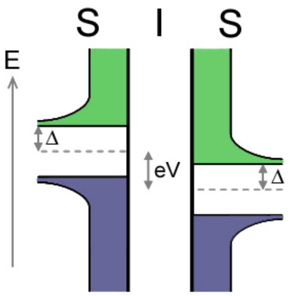

Figure 2.5: *SIS junction energy level. The gap energy level,* Δ*, shows why the bias voltage should be* $2\Delta/e$*.*

frequencies and operate as square law detectors for these high frequency photons. HIFI covers the full spectrum frequency range by the mean of seven mixers, where each mixer is referred to as a band. These bands and frequency range coverage will be explained thoroughly in next section. Table 2.1 shows the mixer each band is using and the LO frequency coverage of each mixer. The frequency resolution of HIFI is 1.1MHz, the corresponding velocity resolution is listed on the last two columns of table.1 for the high and low frequency ends of each band.

Band(s)	Mixer type	LO. Lower Freq. GHz	LO. Upper Freq. GHz	Beam-width FWHM	IF Band-width GHz	Velocity Resolution at lower freq. *km/s*	Velocity Resolution at higher freq. *km/s*
1	SIS	488.1	628.4	39”	4.0	0.7	0.5
2	SIS	642.1	793.9	30”	4.0	0.5	0.4
3	SIS	807.1	952.9	25”	4.0	0.4	0.3
4	SIS	957.2	1113.8	21”	4.0	0.3	0.3
5	SIS	1116.2	1271.8	19”	4.0	0.3	0.3
6 & 7	HEB	1430.2	1901.8	13”	2.4	0.2	0.2

Table 2.1: *HIFI frequency coverage, mixer types and band information. Table from HIFI Observer’s Manual, ver. 20.4*

2.3 Secondary data processing.

After the data were downloaded from Herschel and run through the HIPE 9[3] pipeline[4], further data analysis and processing was done using CASSIS[5]. Cassis is Java based program to analyze spectroscopic data, particularly for astrophysics. CASSIS is created by astrophysicists and developers at IRAP[6] in Toulouse, France. CASSIS comes with a lot of basic functionality such as, spectrum plotting, baseline subtraction, and Gaussian fitting. It also provides some more advanced functions like population diagram fitter and spectral line modeling, which will be described in later sections.

CASSIS also comes with pre-built in molecular and atomic line databases, such as CDMS [7], JPL[8], NIST[9] and VASTEL[10]. These are databases produced by different institutes either based on laboratory measurements, theoretical calculations, or from astronomical observations. These databases provide us with accurate frequencies, oscillator strengths, upper state energies, and quantum numbers for thousands of transitions in the GHz to THz frequency range.

The level 2 data product[11] provided by the HIPE 9 pipeline is a time integrated, calibrated spectrum for each of HIFI's two polarizations so the first step is to add up these two independent spectra and average them. In order to do this we use CLASS which is another

---

[3] The data processing application is Herschel Interactive Processing Environment (HIPE). After running through HIPE we can start interacting with data.

[4] The HIFI pipeline is used for processing data received HIFI spectrometers into a final product that is suitable for interactive analysis.

[5] http://cassis.cesr.fr

[6] L'Institut de Recherche en Astrophysique et Plantologie (The Research Institute in Astrophysics and Planetology)

[7] Cologne Database for Molecular Spectroscopy

[8] Jet Propulsion Laboratory

[9] National Institute of Standards and Technology

[10] Separation of the same species due to the forbidden transitions, ortho and para, or different spatial structure.

[11] Final level after running through the HIPE 9.

program widely used for the purpose of reducing spectroscopic data obtained on single-dish telescopes. CLASS is one of the programs under a collective set of software called GILDAS, developed by IRAM[12]-Grenoble based on Fortran 90 and C/C++. CLASS also allows us to identify lines, subtract base lines, and fit Gaussians (up to 5 components).

The data from HIPE do not account for the source velocity with respect to the telescope's frame of reference, therefore, the next step is take into account the Doppler shift, by including the known velocity of the Orion Nebula ($7km\ s^{-1}$; Joseph P. McMullin et. al. 1992). However, applying the Doppler velocity to the center of the band will not fully correct the data, especially at the band edges. Given the large bandwidth, and the fact that the spectrometer has a fixed frequency resolution of 1.1 MHz, this means the velocity width of each channel changes from one end of the band to the other. Thus, we have to correct for this variable width to ensure that the Doppler velocity of each frequency channel is calculated correctly. CLASS also provides some functionality not found in CASSIS, such as the co-averaging of spectra and spectral smoothing.

The continuum emission in HIFI may not always be correct since continuum calibration is not very accurate for a Heterodyne instrument. So in order to focus solely on the strength of the emission lines, the continuum should be removed by subtracting any residual baseline (or offset from the zero point on the intensity axis; see fig. 2.6). CLASS actually does this by fitting and subtracting the baseline in regions[13] free from emission. These regions must be selected and set manually by the user. In most cases a linear baseline fit is accurate enough but higher order polynomials can be fitted if needed.

---

[12] institute for millimetric radio astronomy

[13] These regions should be defined in CLASS by the users.

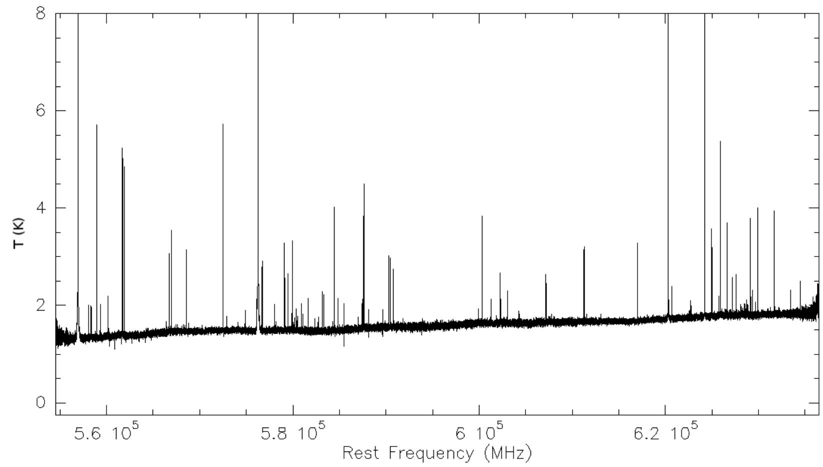

Figure 2.6: *This spectrum of band 1b ensures first order, linear, of baseline fit and subtraction is sufficient.*

Often the lines are weak and one way to suppress the noise is to spectrally smooth the data. Fig. 2.7 shows an example of a spectrum around 576-582GHz and provides an example of an unsmoothed spectrum. Fig. 2.8 shows the same spectrum smoothed by a factor of 6 in frequency and demonstrates how the S/N ratio improves in this scenario but at the cost of reduced resolution.

In order to see how smoothing works it is essential to understand noise uncertainty due to random processes. The standard radiometer equation for a radio telescope (Wilson T.L et al 2009, Chapter 4.2.1) is: Figure 2.7

$$T_{rms} \propto \frac{T_{sys}}{\sqrt{\Delta\nu \ \tau}} \tag{2.5}$$

where T_{sys} for each HIFI band is shown in Figure 2.9. $\Delta\nu$ is the frequency resolution of the receiver, which is $1.1 \times 10^6 Hz$ for HIFI. And τ is the observation time.

Smoothing simply averages the noise among several adjacent channels. The frequency

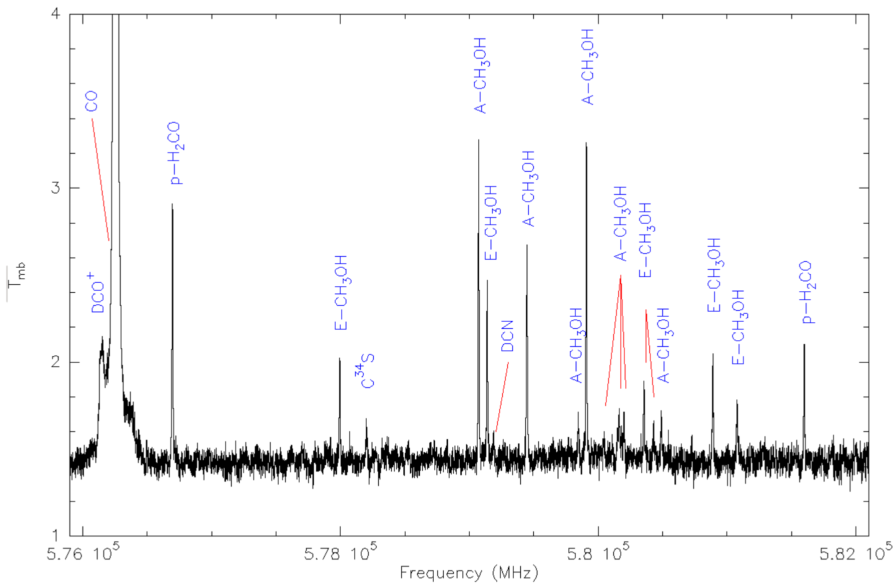

Figure 2.7: *The figure shows an unsmoothed Orion-S spectrum.*

resolution, therefore, changes depending on the number of adjacent channels over which we are taking the average the frequency resolution changes. The new frequency resolution (after smoothing), velocity resolution, and noise level in the data (1σ rms) value are listed in table 2.2. The number of channels over which to smooth was chosen in a way to ensure that the ratio of observed T_{rms} and $T_{sys}/\Delta\nu$ is almost constant from one band to another.

	Freq used (GHz)	Smoothing degree*	Freq. Res.* $\Delta\nu$ (MHz)	Vel. Res.* Δv $(km.s^{-1})$	T_{sys} (K) approximation	$T_{sys}/\sqrt{\Delta\nu}$	T_{rms} $^\diamond$
band 1	555	2	2.2	~ 1	~ 100	~ 0.1	~ 0.1
band 2	716	4	4.4	~ 2	~ 150	~ 0.1	~ 0.1
band 3	857	4	4.4	~ 2	~ 200	~ 0.1	~ 0.1
band 4	1044	8	8.8	~ 3	~ 400	~ 0.1	~ 0.2
band 5	1235	8	8.8	~ 2	~ 1000	~ 0.3	~ 0.4
band 6	1514	16	17.6	~ 3	~ 1300	~ 0.3	~ 0.7
band 7	1787	16	17.6	~ 3	~ 1300	~ 0.3	~ 0.7

$\ast$ Number of adjacent channels averaged together.
$\star$ Calculated for the frequencies listed, near the middle of each band.
$\diamond$ This is observed RMS noise from the spectra at the listed frequencies.

Table 2.2: *Noise level and resolution after smoothing.*

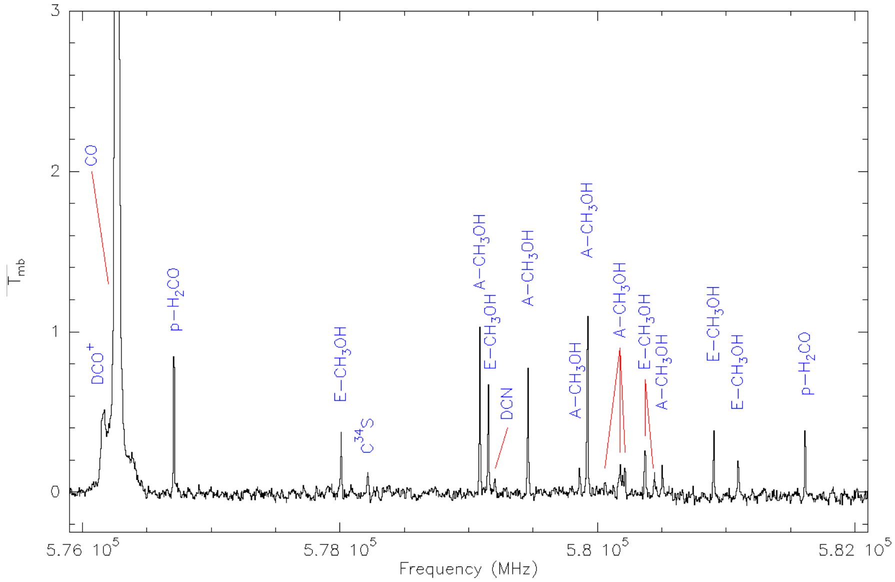

Figure 2.8: *The same frequency range as the previous figure after smoothing. By smoothing the data we can suppress the noise and begin to see the actual line profiles.*

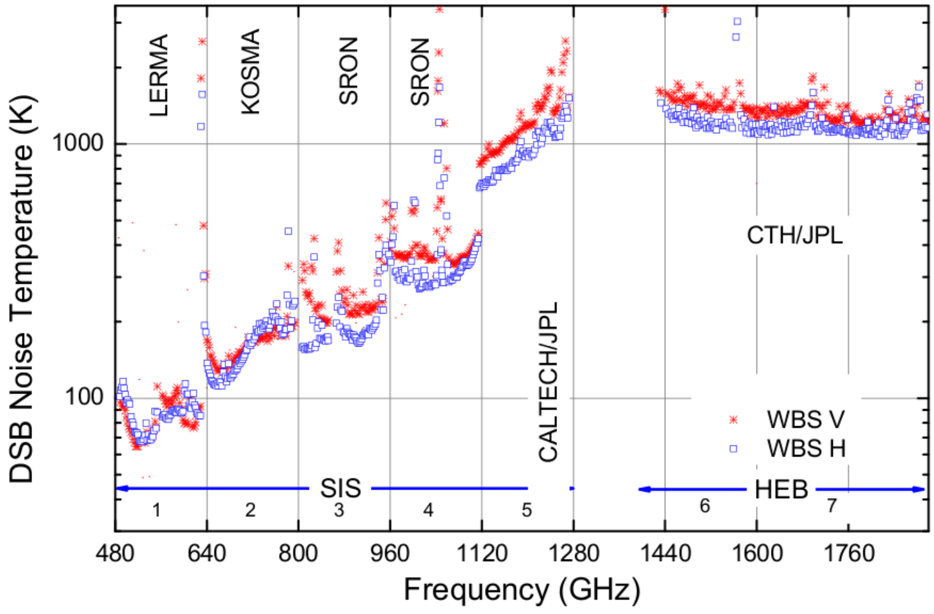

Figure 2.9: *This figure shows system temperature frequency dependence of HIFI for both H-polarization (blue squares) and V-polarization (red circles). Figure from P.R. Roelfsema et. al. 2011*

Chapter 3

Results

3.1 Line Identification

Once the HIFI data for each band have been co-added, Doppler corrected, and spectrally smoothed we can begin to identify the variety of species producing the emission lines. This was done via the CASSIS package.

The first step was to identify the strong emission lines from common species that are known to exist in the ISM in other star forming regions. These species have been compiled into a separate sub-database within CASSIS by other researchers. The graphical display tool within CASSIS makes it easy to identify species. The green lines in Fig 3.1 show all possible transitions with upper state energy levels of 150 K or less (the energy of the upper quantum state). This tool shows that even in a relatively small frequency range of 576-582GHz, there are a large number of possible transitions. To ensure that we do not miss any possible correct line identifications, we arbitrarily set the upper energy state to $1500K$. The species that we focused on in this step were CO, $C^{18}O$, ^{13}CO, SO_2, H_2CS, CH_3OH, CCH, CH, H_2O, N_2H^+, HCN, HNC, and HCO^+. The observed frequencies are listed in table. A.1

Once this first step was accomplished we began to examine the weaker and less well-known species/transitions. For this task we used the full molecular line database in CASSIS which includes the CDMS, and JPL databases, see section 2.4.

As can be seen in figure 3.1 and 3.2, many of these lines have multiple possible identifications (based solely on their tabulated frequencies). Thus, the next step is to determine

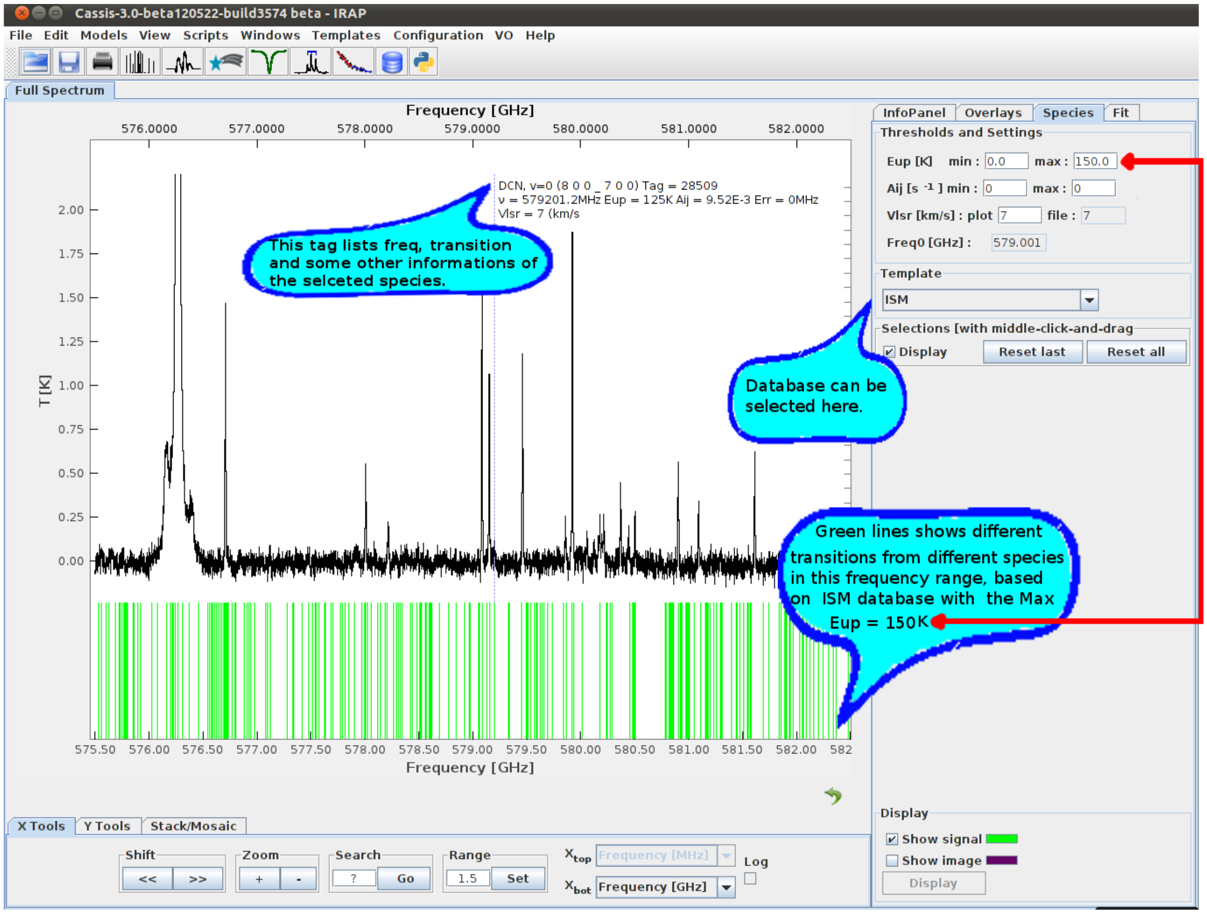

DCN, v=0 (8 0 0 _ 7 0 0) Tag = 28509
ν = 579201.2MHz Eup = 125K Aij = 9.52E-3 Err = 0MHz
Vlsr = 7 (km/s

This tag lists freq, transition and some other informations of the selceted species.

Thresholds and Settings
Eup [K] min : 0.0 max : 150.0
Aij [s -1] min : 0 max : 0
Vlsr [km/s] : plot 7 file : 7
Freq0 [GHz] : 579.001

Template
ISM

Database can be selected here.

Green lines shows different transitions from different species in this frequency range, based on ISM database with the Max Eup = 150K

Display
☑ Show signal
☐ Show image

Xtop Frequency [MHz]
Xbot Frequency [GHz]

Figure 3.1: *Figure shows how the basic CASSIS line identification works.*

which of the possible line IDs is the correct one. This step involves some simple LTE (Local Thermodynamic Equilibrium) modelling of the line profiles for each of the possible species in multiple bands which allows us to estimate the relative contributions of each species to the overlapping spectral feature. Details of the modelling procedure will be provided in the analysis chapter (chapter 4). Fig. 3.2 shows an example at 506.827GHz, where there are two possible IDs for this line. If the unknown line is selected to be DCN then if we fit the observed transition in this band, the model predicts that another transition of DCN should occur at frequency 579.199GHz. If we examine frequency 579.199GHz and see a transition of DCN where it is predicted to be, then the line at 506.827GHz likely does arise from species DCN. However, if we identify the original line at 506.827Ghz as $HOONO_2$ then the model predicts another $HOONO_2$ transition at 508.041GHz which we do not see. Thus, the line at 506.827GHz is probably not $HOONO_2$.

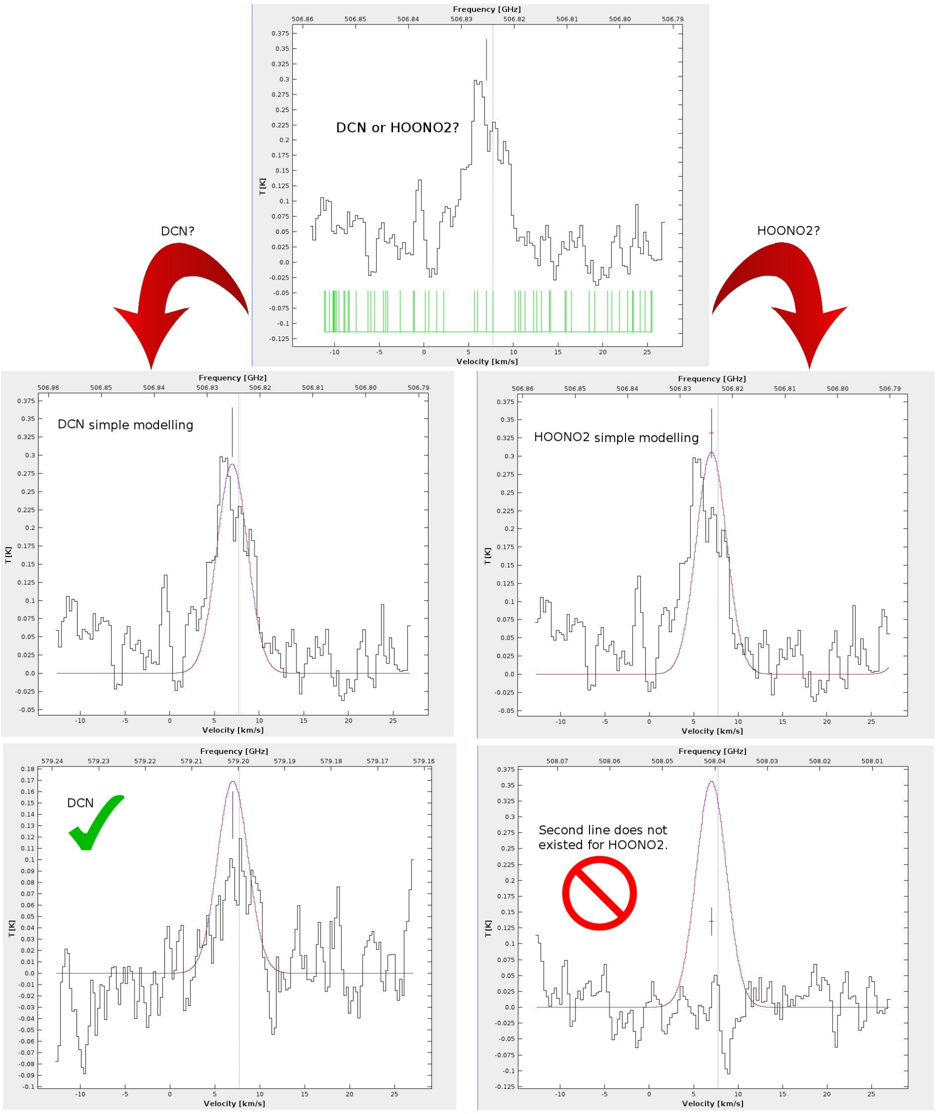

Figure 3.2: *The procedure to find the right species out of potential candidates.*

This is done for each of the potential candidate species until the models match the observations in all bands. We have listed all the observed lines with peak intensity 3σ above noise in each band in table A.1 including all the identified and unidentified lines. Unidentified lines are listed as U.

More than 800 different transitions, including their peak intensities, from 47 different species, listed in table 3.1 and some unidentified spectral lines are listed in table A.1. The

Table 3.1: *Identified species in Orion-S.*

atoms	di-atomic molecules	multi-atomic molecules	Ionized species
$C-atom$	CO	CCH	C^+
	$^{13}C^{18}O$	DCN	CH^+
	^{13}CO	HNC	CO^+
	$C^{17}O$	HCN	DCO^+
	$C^{18}O$	$H^{13}CN$	$H^{13}CO^+$
	CS	HDO *	$HC^{18}O^+$
	$C^{34}S$	$o-H_2O$ **	HCO^+
	^{13}CS	$p-H_2O$ **	N_2H^+
	CH	$H_2^{18}O$ *	
	HCl *	$o-H_2S$ **	
	$H^{37}Cl$ *	$p-H_2S$ **	
	SO	$H_2^{33}S$	
	NO *	$H_2^{34}S$	
	SH^+	SO_2	
	SiN	H_2CS	
	SiO	$o-H_2CO$ **	
	CN	$p-H_2CO$ **	
		$o-NH_3$ **	
		$p-NH_3$ **	
		$A-CH_3OH$ **	
		$E-CH_3OH$ **	

* JPL database used for these species.
** VASTEL database used for these species.
For all other species CDMS database is used.

intensity of each line is reported in Kelvin.

3.2 Gaussian fit methodology

To be able to extract physical conditions of the gas from these spectral line observations we need to obtain the intensity, frequency, velocity with respect to the local standard of rest (V_{lsr}), flux, Full Width Half Maximum (FWHM), and source size. We do this via Gaussian fitting. The Gaussian fit uses a Levenberg-Marquardt algorithm implemented in Cassis.

Since Orion-S is believed to be a very young star formation region, the effect of the hot core or an outflow may not be obvious for most species, and it can be assumed that the observed lines are coming from a single extended component, where extended means it uniformly fills the beam at all frequencies (bigger than $39''$, see table 2.1). It turns out that, in most cases, a single component Gaussian fit to a specific species can reasonably reproduce the observed lines. Fig. 3.3 shows one of CH lines as an example. However, for some other lines a two component Gaussian fit is needed to fit the data. An example of a two component fit is HCN, shown in Fig. 3.4, which shows the effect of an outflow on the observed lines. HCN is known to be a tracer of outflow in many star formation regions (Bachiller & Rez Gutierrez 1997).

Table B.1 shows the results of Gaussian fitting of all the identified transitions. Note that in case of two component fits the narrower component is referred as "main" and the broad component is referred to as "wing". Fits were only performed on identified lines with $S/N > 5\sigma$. The first column in table. B.1 are the transition quantum numbers (an explanation of the quantum numbers are provided at either the CDMS[1] or the JPL websites[2]). Table 3.1 indicates which database we used in the line identification (The VASTEL database uses the CDMS and JPL quantum number coding). The frequency of the fitted Gaussian profile is listed in the second column. T_{mb} and V_{lsr} are respectively the intensity and centroid velocity of the corresponding Gaussian fit. ΔV_{FWHM} is the "Full Width Half Maximum", and $\int T_{mb} dV$ is the flux.

Some observed lines are the superposition of more than one species so they were excluded from table B.1 since the Gaussian fit does not reliably separate emission from different overlapping transitions.

---

[1] http://www.astro.uni-koeln.de/cdms/catalog

[2] http://spec.jpl.nasa.gov/ftp/pub/catalog/doc/catintro.pdf

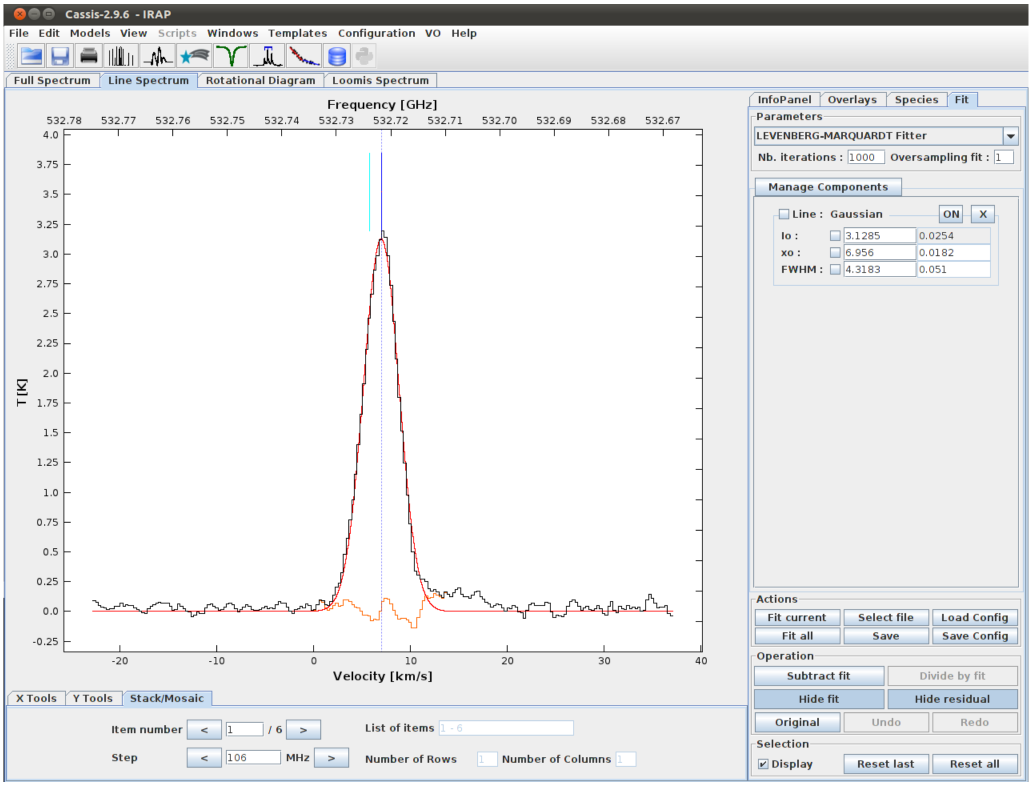

LEVENBERG-MARQUARDT Fitter

Nb. iterations : 1000 Oversampling fit : 1

☐ Line : Gaussian

Io :	☐	3.1285	0.0254
xo :	☐	6.956	0.0182
FWHM :	☐	4.3183	0.051

☑ Display

Item number 1 / 6

Step 106 MHz

List of items 1 - 6

Number of Rows 1 Number of Columns 1

Figure 3.3: *Singl100e Gaussian fit (red) to an observed CH line (black), where the orange line is the residual.*

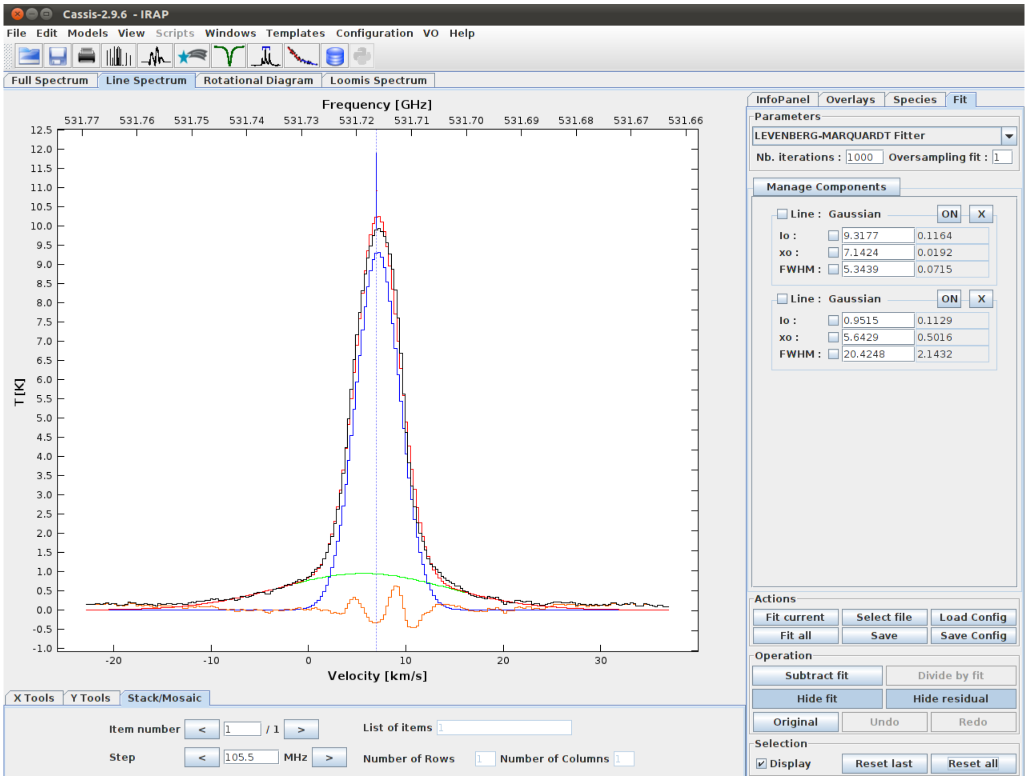

LEVENBERG-MARQUARDT Fitter

Nb. iterations : 1000 Oversampling fit : 1

☐ Line : Gaussian

Io : ☐ 9.3177 0.1164

xo : ☐ 7.1424 0.0192

FWHM : ☐ 5.3439 0.0715

☐ Line : Gaussian

Io : ☐ 0.9515 0.1129

xo : ☐ 5.6429 0.5016

FWHM : ☐ 20.4248 2.1432

☑ Display

Item number 1 / 1

List of items 1

Step 105.5 MHz

Number of Rows 1 Number of Columns 1

Figure 3.4: *Multiple Gaussian fit to a HCN line. Here the green line is the broad component (wing), the blue one the narrow component fit (main) and the red line is sum of these two fits. The observed HIFI line is shown in black, whereas the residual with respect to the 2 component fit (red) is shown in Orange.*

Table 3.2: *Percentage of received flux per species*

Species	Total Flux of species	Flux percentage %
CO	5470.34	59.21 %
$^{13}C^{18}O$	1.82	0.02 %
^{13}CO	828.39	8.97 %
$C^{17}O$	37.82	0.41 %
$C^{18}O$	154.84	1.68 %
$CS, v = 0$	123.11	1.33 %
^{13}CS	1.20	0.01 %
$C^{34}S$	6.38	0.07 %
C^+	309.43	3.35 %
$C{-}atom$	46.80	0.51 %
CCH	48.64	0.53 %
CH	39.57	0.43 %
CH^+	19.27	0.21 %
$CN, v = 0$	6.41	0.07 %
$DCN, v = 0$	1.99	0.02 %
DCO^+	1.24	0.01 %
HCl	39.90	0.43 %
$H^{37}Cl$	20.02	0.22 %
$H_2^{18}O$	1.88	0.02 %
H_2CS	8.51	0.09 %
$o{-}NH_3$	30.63	0.33 %
HCO^+	447.28	4.84 %
$H^{13}CO^+$	12.81	0.14 %
$HC^{18}O^+$	0.58	0.01 %
HDO	3.13	0.03 %
HCN	236.73	2.56 %
$H^{13}CN$	7.24	0.08 %
HNC	11.52	0.13 %
N_2H^+	29.95	0.32 %
NO	7.62	0.08 %
CO^+	0.43	0.01 %
SiN	2.07	0.02 %
$o{-}H_2CO$	152.22	1.65 %
$p{-}H_2CO$	55.44	0.60 %
$o{-}H_2S$	60.00	0.65 %
$p{-}H_2S$	23.05	0.25 %
$H_2^{33}S$	0.77	0.01 %
$H_2^{34}S$	3.07	0.03 %
SH^+	0.42	0.01 %
SiO	4.59	0.05 %
SO	93.52	1.01 %
SO_2	17.41	0.19 %
$A{-}CH_3OH$	483.19	5.23 %
$E{-}CH_3OH$	387.08	4.19 %
Total Recieved Flux	9238.31	100.00 %

3.3 Individual Species

A detailed analysis of every individual species is beyond the scope of this thesis, so in the following sections we will provide a brief description of the observed characteristics of a few of the most important ones, which contributes to the bulk of the emission intensity.

3.3.1 CO and isotopologues

CO and its isotopologues are linear molecules which comprise more than 70% of the total integrated line flux from Orion S. CO is important as a tracer of molecular gas. It is used as a proxy for H_2 which is unobservable due to not having a dipole moment and hence no allowed rotational transitions exist. Vibrational quadrupole transitions occur in H_2 but are not excited under the conditions that prevail in GMCs. Carbon monoxide is believed to be the most abundant interstellar molecule after H_2 with an $H_2 : CO$ abundance ratio of 10,000:1 (van Dishoeck & Black 1987). Therefore, CO observations are used to determine the masses and distributions of molecular hydrogen clouds(Young & Scoville 1991).

There exists a critical density at which collisions and radiation are equally important; above this threshold, Local Thermodynamic Equilibrium(LTE) will hold. (for details see Chapter 4). As listed in table B.1, we detect CO emission from J=5 (which has $E_{up} = 83\ K$, & $n_{crit} \sim 1.7 \times 10^5\ cm^{-3}$) to J=16 (which has $E_{up} = 752\ K$, & $n_{crit} \sim 3.4 \times 10^6\ cm^{-3}$) in the temperature range of $30\ K < T < 100\ K$. Thus, by observing such a large range of high and low J transitions with the HIFI instrument we are probing a wide range of physical conditions.

Figure. 3.5 shows the first 9 observed transitions of CO (see table B.1). A first glance at this figure shows definite non-Gaussian line shapes at some frequencies, e.g. 806.65, 921.89, and 1159.99 GHz. An investigation revealed that these negative spurs occur due to emission in the off position. HIFI takes data by continuously chopping between the source position (on position) and a nearby off position, used for subtracting out background emission. However, if the line emission is extended one can have emission in the off position which, when subtracted, shows up as a pseudo absorption feature. A procedure is being implemented to correct for this contamination but it is beyond the scope of this thesis. In next chapter, where we analyse our data, we tried to reduce the emission in off position effects by reverting to the raw data.

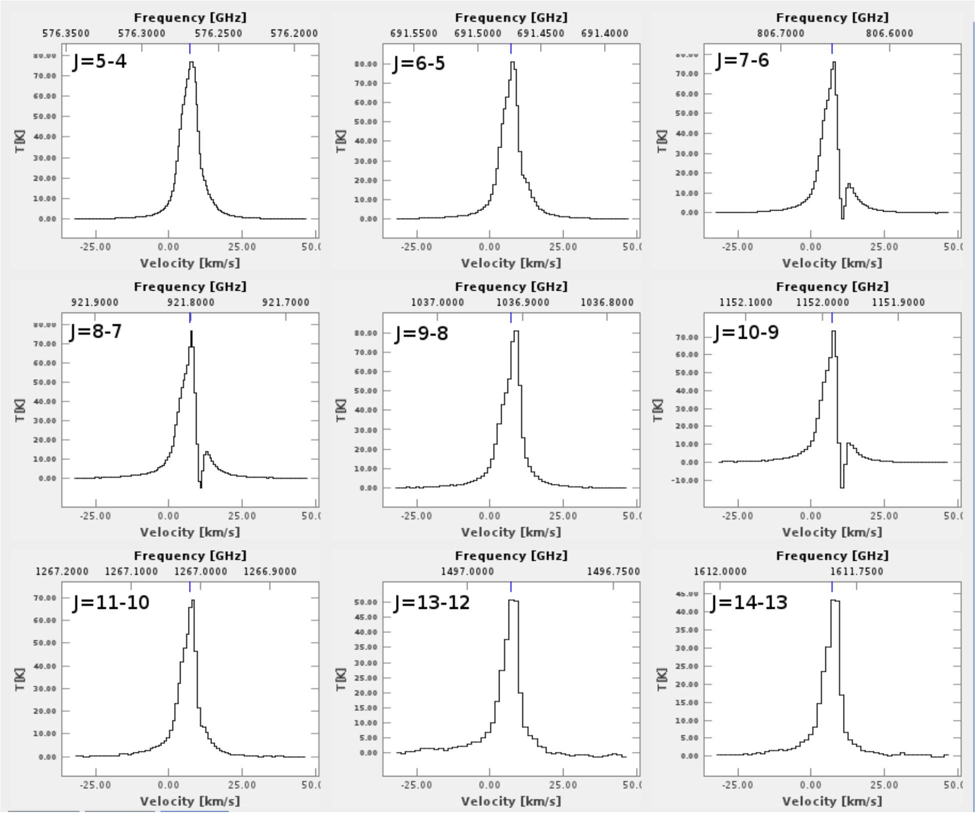

Figure 3.5: *Observed CO lines*

Figure 3.6 shows an Owens Valley Radio Observatory (OVRO) Map of CO 2-1 emission from Orion-South by Zapata et al. (2005). The most prominent feature is a highly collimated, high velocity outflow with a length of 0.07 *pc* and velocities of $-140\ km\ s^{-1}$ (blue shifted) to the NW and $88\ km\ s^{-1}$ (red shifted) toward the SE (Rodrigues-Franco et al. 1999). As the ΔV_{FWHM} of the wing in table. B.1 shows an outflow is observed spanning

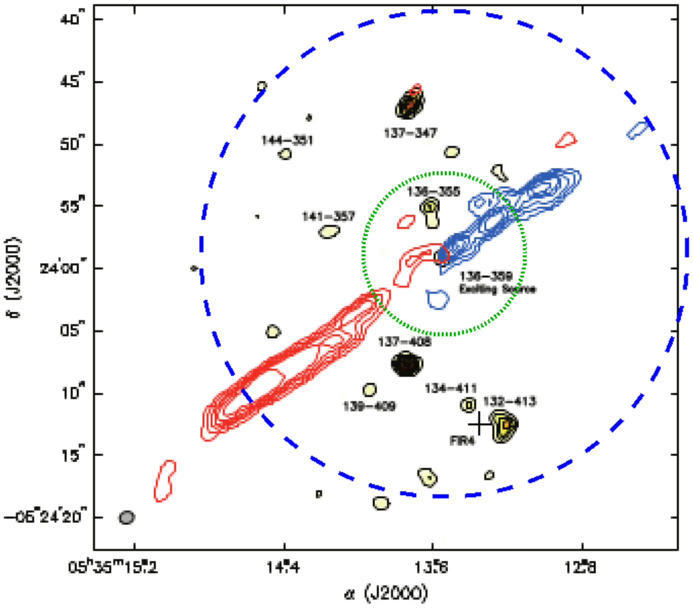

Figure 3.6: *The blue and red contours show the velocity ranges of* -80 *to* -26 $km\,s^{-1}$ *(blue shifted) and* 22 *to* 82 $km\ s^{-1}$ *(red shifted) respectively (Zapata et al. 2005). The green and blue circles show the minimum (*$13''$*) and maximum (*$39''$*) beam width on the outflow map made by Zapata et al. 2005.*

$\sim 20\ km\ s^{-1}$, this is also seen in fig. 3.7. Another extended bipolar CO outflow has been reported at a low velocity ($5km\ s^{-1}$), in the orientation of NE (blue shifted) to SW (red shifted) (Schimd-Burgh et al. 1990). The much smaller measured outflow velocity in our data is likely due to beam filling factor effects. As figure 3.6 shows, the Band 1 Herschel beam encompasses the whole region (blue circle), or partially covers the outflow in higher HIFI bands, bands 6 & 7 (green circle). Thus, the emission from the outflow will be reduced in intensity by the ratio of the area of the outflow emission region to the area of the beam. The observed intensity from the highest velocity gas may be reduced below the noise level of our observations and, therefore may be undetectable.

Also, more importantly, our lowest detected J transition for $CO\ J = 5 \rightarrow 4$ has a critical density (n_{crit}) $\sim 1.7 \times 10^5\ cm^{-3}$ which is much higher than that of $CO\ J = 2 \rightarrow 1$ $n_{crit} \sim 8 \times 10^3\ cm^{-3}$. Since gas in outflows is generally of lower density (e.g., Tafalla

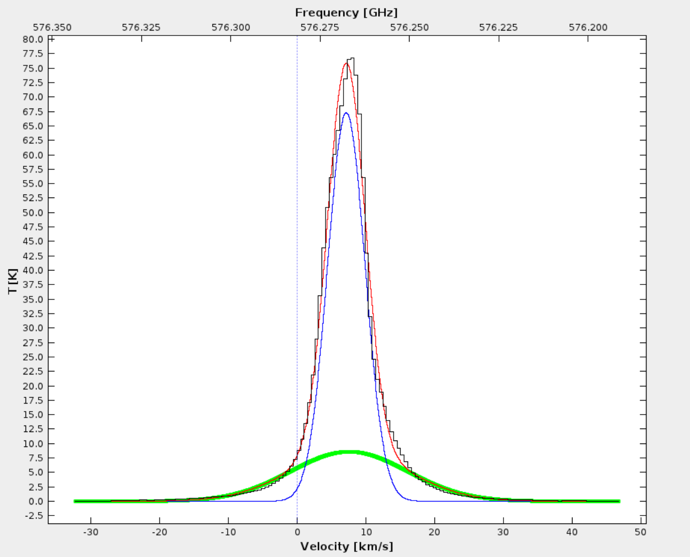

Figure 3.7: *The green line shows the Gaussian fit to the outflow (wing) and the blue line is the fit to the main component. The red line is sum of main and wing components of the Gaussian fit to this transition of CO* $J = 5 \rightarrow 4$.

and Myers, 1997; Dobashi andUehara, 2001; Takakuwa et al., 2003; Beltrn et al., 2004a) it makes sense that the outflow should be less prominent in the high J lines than the low J lines.

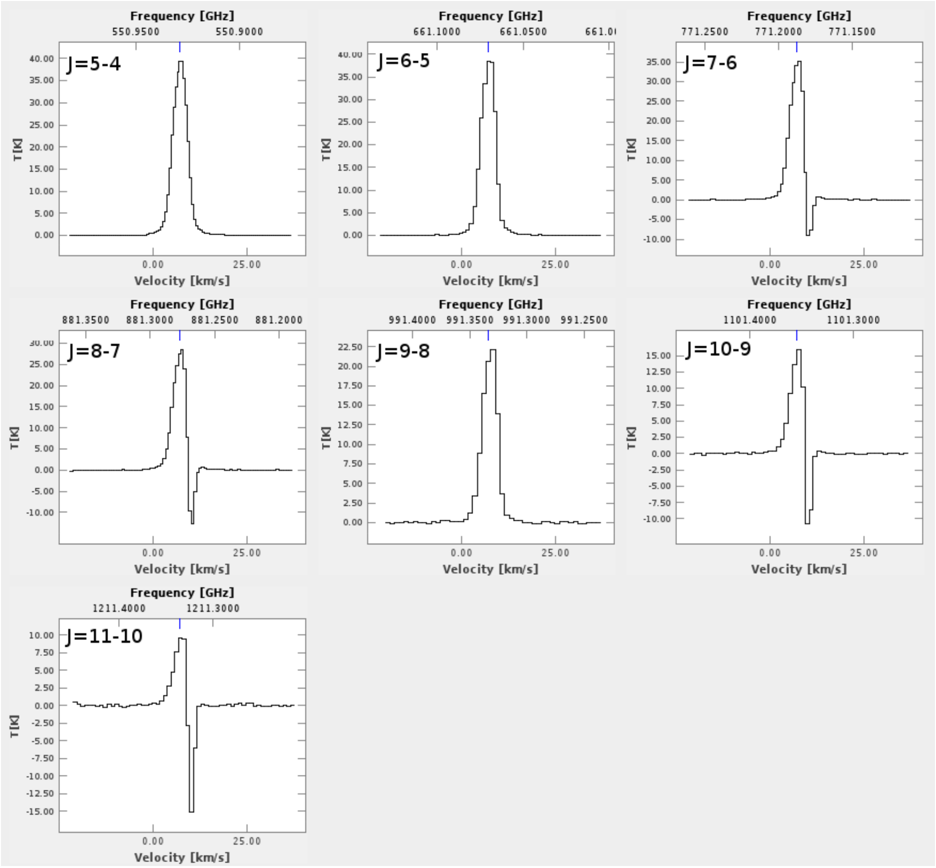

Figure 3.8: *Observed* ^{13}CO *lines.*

Figure 3.8 shows the observed line profiles of ^{13}CO. As with CO, emission in the off position is effecting our spectra. Nevertheless, it is clear that outflows are not as evident in the ^{13}CO spectra as in those of CO. This is mainly due to the lower isotopic abundances of ^{13}CO ($^{12}C/^{13}C \sim 55$; Wilson & Matteucci 1992) and the fact that the lower column density gas in the outflow becomes more difficult to trace.

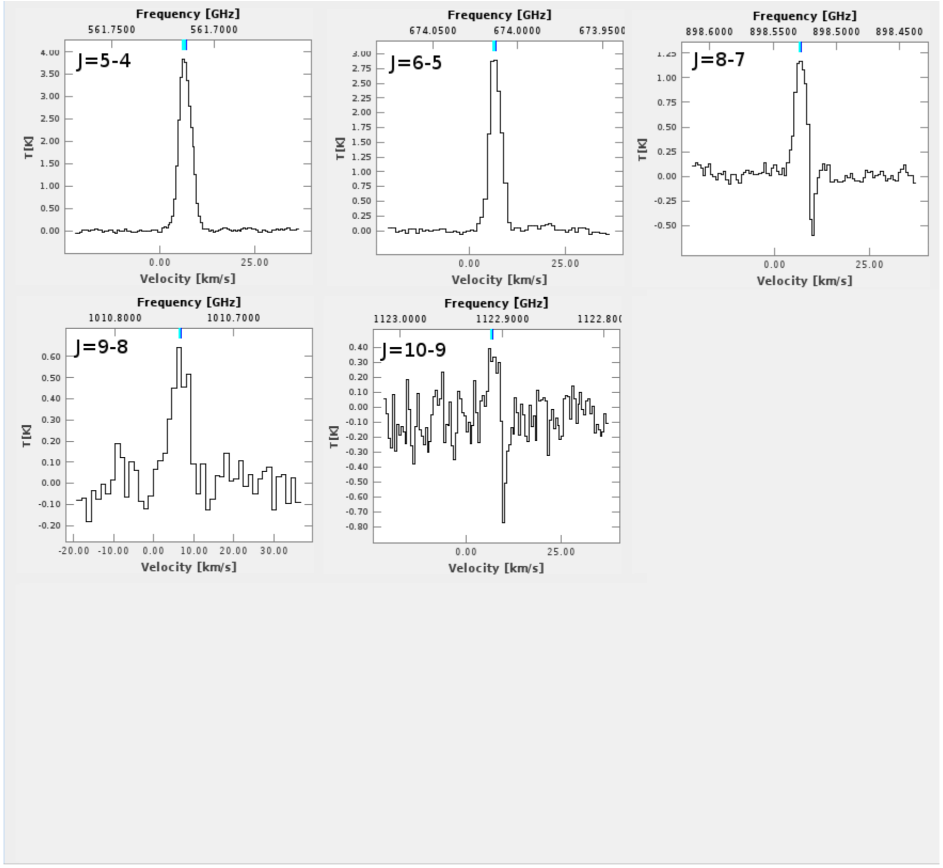

Figure 3.9: *Observed $C^{17}O$ lines.*

As shown in figure 3.9 for $C^{17}O$, at the frequency of 898.525 GHz we again encounter emission in the off position. $C^{17}O$ has hyper fine structure due to the interaction between the electronic angular momentum and the nuclear spin of $I = 5/2$ in the ^{17}O nucleus. While the hyper fine splitting is unresolved it does make more complex analysis or modelling of the lines more complicated. Also, one of the transitions at frequency of 786.282 GHz is not shown here due to line blending.

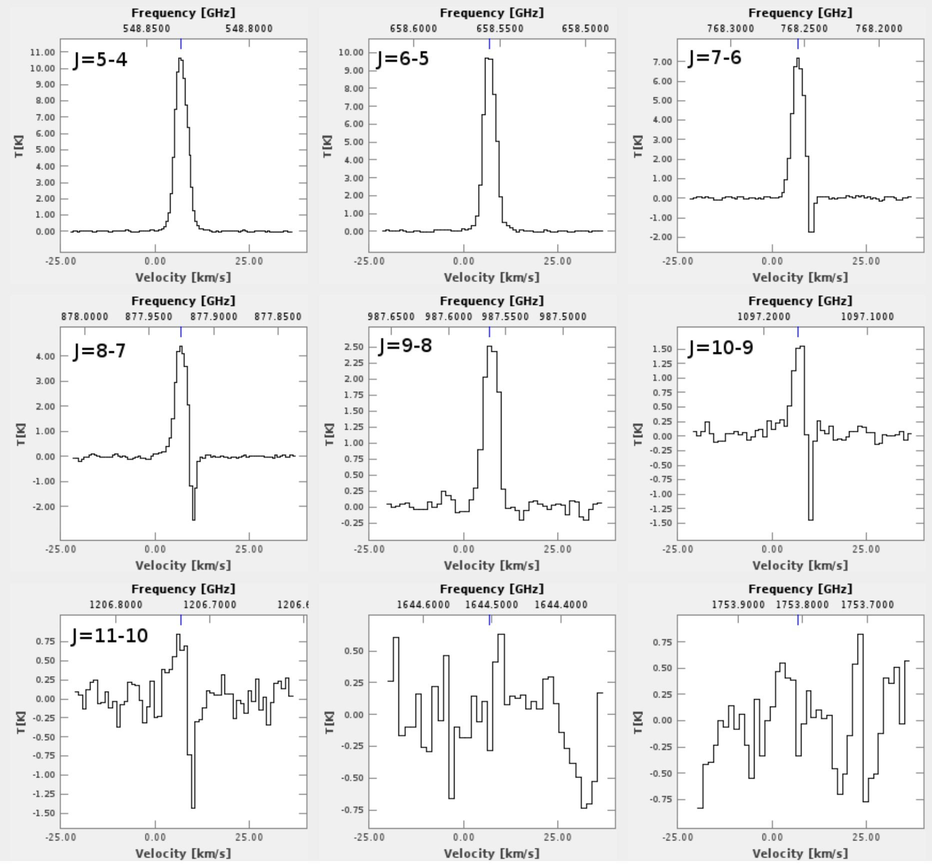

Figure 3.10: *Observed $C^{18}O$ lines.*

$C^{18}O$ is an important species for subsequent modelling since it is usually optically thin ($CO/C^{18}O \sim 500$; Dishoeck & Black 1998) and so is often a direct tracer of column density. In our data it suffers from contamination in the off position which will make modelling difficult, (see chapter 4). As with ^{13}CO we do not see evidence for outflows in $C^{18}O$.

In $C^{18}O$ the higher J transitions are somewhat wider than the lower ones (i.e. uncontaminated J=9-8 is wider than uncontaminated J=5-4, see table B.1) indicating a contribution to the emission from a smaller, warmer region. This will be investigated further in chapter 4.

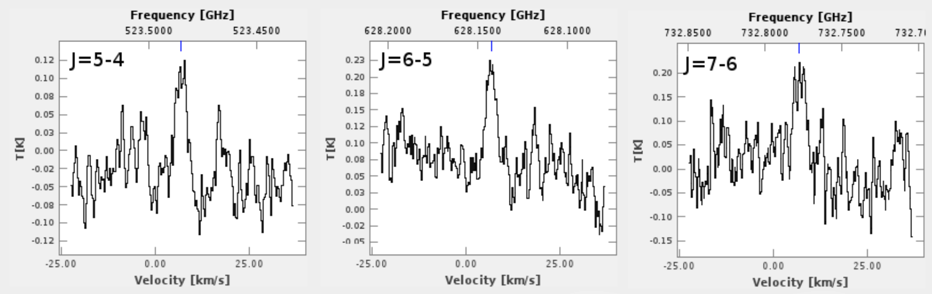

Figure 3.11: *Observed* $^{13}C^{18}O$ *lines.*

Figure 3.11 shows the last observed carbon monoxide isotopologues, $^{13}C^{18}O$, toward Orion-S. We searched for other isotopologues, i.e. $^{13}C^{17}O$, and we could not detect them. $^{13}C^{18}O$ has hyperfine structure such as $C^{17}O$.

3.3.2 CS, ^{13}CS, and $C^{34}S$

CS is a diatomic linear molecule with a pure rotational spectrum. It is a well know tracer of dense gas due to its high critical density (Plume et al 1992) and has been seen in many other massive star forming regions (e.g, Plume et al 1992, 1997, Shirley et al. 2003, Wu et al. 2010). Like CO we observe many J transitions, from J= 10-9 up to J=19-18, which correspond to $E_{up} = 155\ K$ & $n_{crit} = 9 \times 10^7\ cm^{-3}$ and $E_{up} = 446\ K$ & $n_{crit} = 4 \times 10^8\ cm^{-3}$ respectively for $30\ K < T < 100\ K$. In contrast with CO, CS and its isotopologues comprise only 1.5% of the total flux, (see table 3.2). Figure 3.12 shows first nine observed transitions of CS. At frequencies 880.903 GHz and 929.733 GHz only one component was needed to fit the observed line profile, see table B.1. However, at higher J, we required two components to fit the observed line profiles: one narrow component ($\Delta_{FWHM} \sim 5\ km\,s^{-1}$) and a broader component ($\Delta_{FWHM} \sim 14\ km\ s^{-1}$). This is not too surprising when one takes into consideration the critical densities of these states ($> 9.6 \times 10^7\ cm^{-3}$) and their excitation energy ($> 20\ K$). Thus, similar to what we see to a lesser extent in $C^{18}O$, it is likely that the higher J transitions are beginning to probe the smaller, denser, hot core in Orion south as well as the cooler, less dense extended envelope. In chapter 4 we will show how the high J CS

transitions may be associated with a small, warm core, by two components LTE modelling.

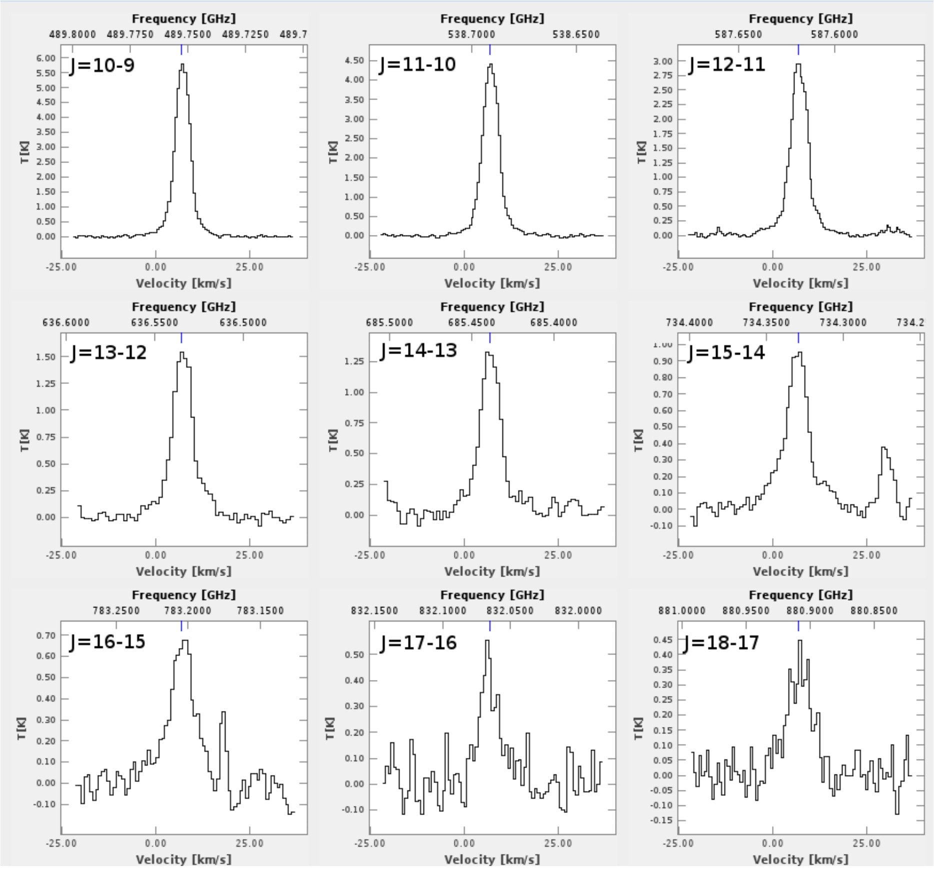

Figure 3.12: *Observed CS lines.*

The hot core broader component seen in CS is not observed in $C^{34}S$, figure 3.13, and ^{13}CS, figure 3.14 again mainly due to lower abundances of isotopes, $[^{32}S]/[^{34}S] \sim 22$ (Wannier & Linke 1978) and $[^{12}C]/[^{13}C] \sim 55$ (Dishoeck & Black 1998).

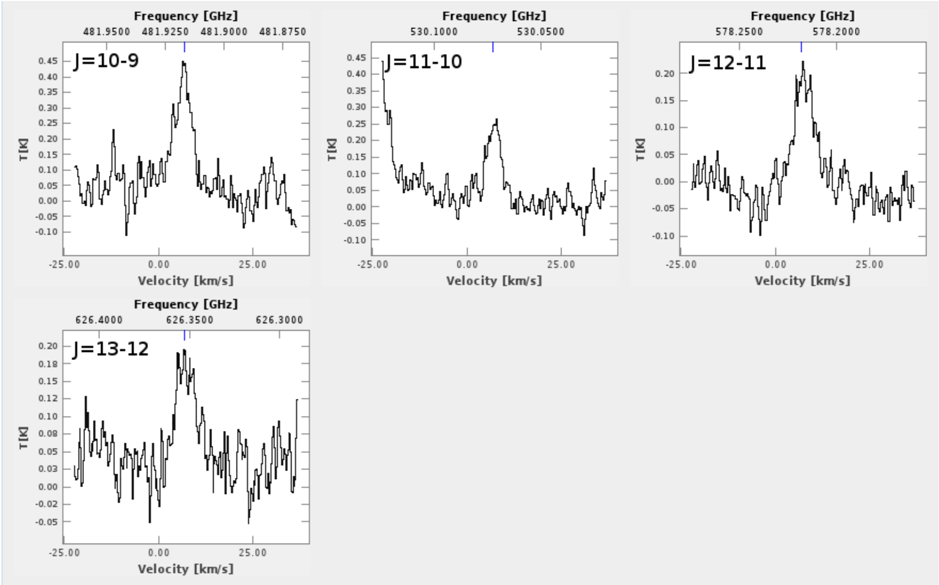

Figure 3.13: *Observed* $C^{34}S$ *lines.*

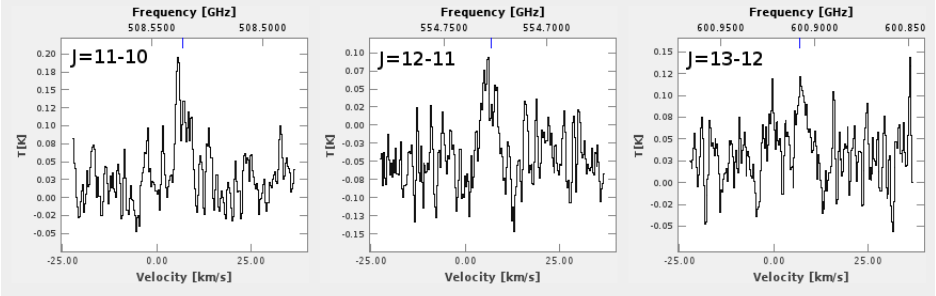

Figure 3.14: *Observed* ^{13}CS *lines.*

3.3.3 C & C^+

Transitions of neutral carbon (C), $[CI]$, and singly ionized carbon (C^+), $[CII]$, are atomic fine structure lines. Table B.1 lists transitions of $[CI]$ & $[CII]$ as $^{2S+1}L_{|L+S|}$, where S, L, J are spin, orbital, and total angular momentum quantum numbers, respectively. The term $2S+1$ is referred to as multiplicity (degeneracy). Both have been seen over large regions of the ISM. $[CI]$ is known to trace the UV illuminated surfaces of GMCs (Papadopoulos et al. 2004; Tielens & Hollenbach, 1985a,b) and $[CII]$ is a tracer of the WIM (Velusamy et al. 2012). Both $[CI]$ & $[CII]$ are thought to be good tracers of "dark gas" which are the regions of the ISM where the gas is mainly molecular (i.e. H_2 instead of HI) but CO has not yet formed (Wolre et al. 2010; Papadopoulos et al. 2004; Bennett et al. 1994; Langer et al. 2010)

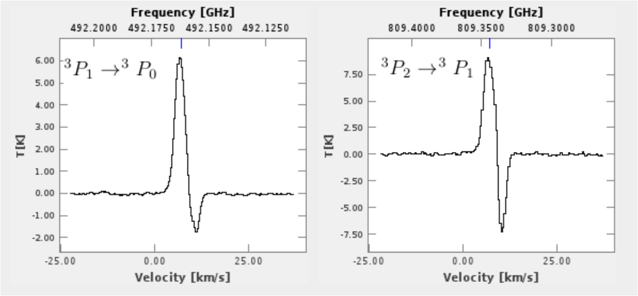

Figure 3.15: *Observed CI lines.*

In HIFI's range of frequency coverage there are two possible transitions of $[CI]$, $^3P_1 \rightarrow ^3 P_0$ and $^3P_2 \rightarrow ^3 P_1$, table B.1 and fig 3.15, and one possible transition (for $T_{ex} < 1500K$) of $[CII]$, table B.1 and fig 3.16. Figure 3.15 shows that $[CI]$ is contaminated with emission in the off position and so its centroid velocity as determined by a Gaussian fit may be slightly erroneous. Since $[CII]$ transition is not contaminated with emission in the off position it can provide a more confident result of an observed velocity, $\sim 8.5km\ s^{-1}$. $[CII]$ and other UV illuminated gas tracer, i.e CH, SH^+, CO^+, have velocities higher than most other species detected $\sim 7.5kms^{-1}$. This may suggest that the WIM surrounding Orion region is kinematically distinct from the molecular gas directly associated with the Orion S star forming region.

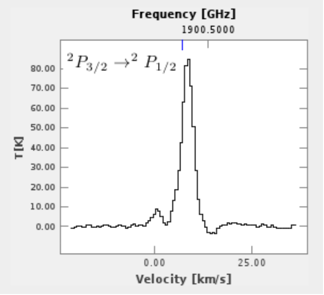

Figure 3.16: *Observed CII $^2P_{3/2} \rightarrow ^2 P_{1/2}$ line.*

3.3.4 $\boldsymbol{CH}$, $\boldsymbol{CH^+}$

CH is a linear radical molecule in which the spin-orbit interaction of the unpaired electron splits the rotational levels. Each of the rotation levels is split into + and − parity which are further split by the hyperfine structure.

The methylidyne radical was detected in the interstellar medium as early as 1937 (Swings & Rosenfeld 1937). CH is a well-known tracer of dark gas (Levrier et al. 2012) in which the abundance $[CH]/[H_2]$ can be as high as 3.5×10^{-2} (Sheffer et al. 2008). As figure 3.17 shows we observe six different transitions of CH.

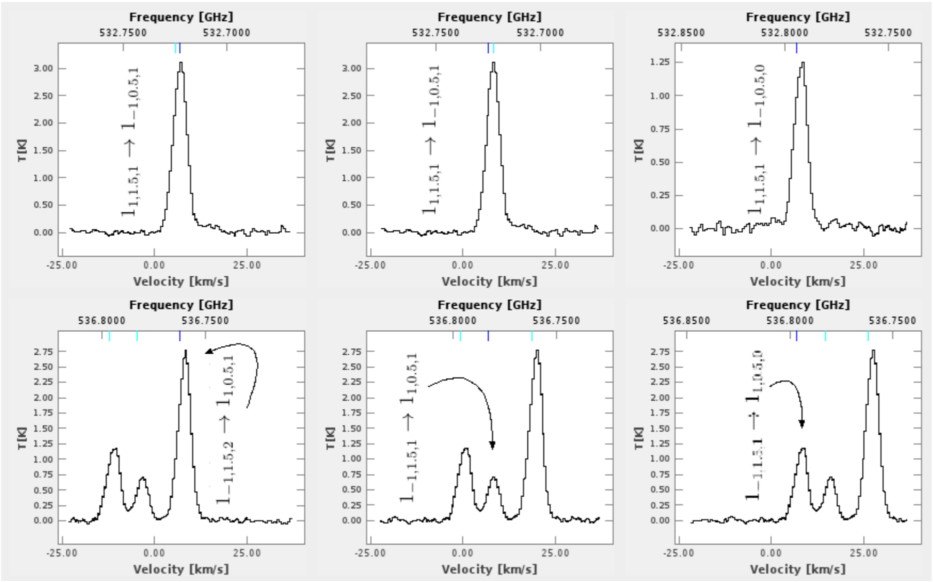

Figure 3.17: *Observed CH lines.*

The only observed CH^+ transition, $J = 1 \rightarrow 0$, is a pure rotational transition, which is shown in fig 3.18. This transition is also contaminated with emission in the off position. This means that the fitted V_{lsr} may be lower than the true V_{lsr}. Thus, CH^+ which is also a PDR tracer might have a true velocity more similar to that of CO^+, CII, CH, etc, see table B.1.

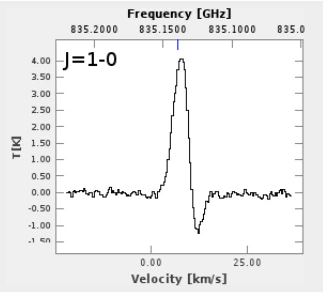

Figure 3.18: *Observed* CH^+ *lines.*

3.3.5 $\boldsymbol{CCH}$

CCH is another linear radical molecule in which the spin-orbit interaction and hyperfine structure splits each level into ladders. CCH is known as a tracer of Photo-Dissociation Region (PDR) (Mul & McGrown 1980). These transitions are also detectable from the ground and complements CH (Gerin et al. 2010), where $[CCH]/[H_2] = (3.2 \pm 1.1) \times 10^{-8}$. Figure 3.18 shows all identified CCH transitions via HIFI spectrum.

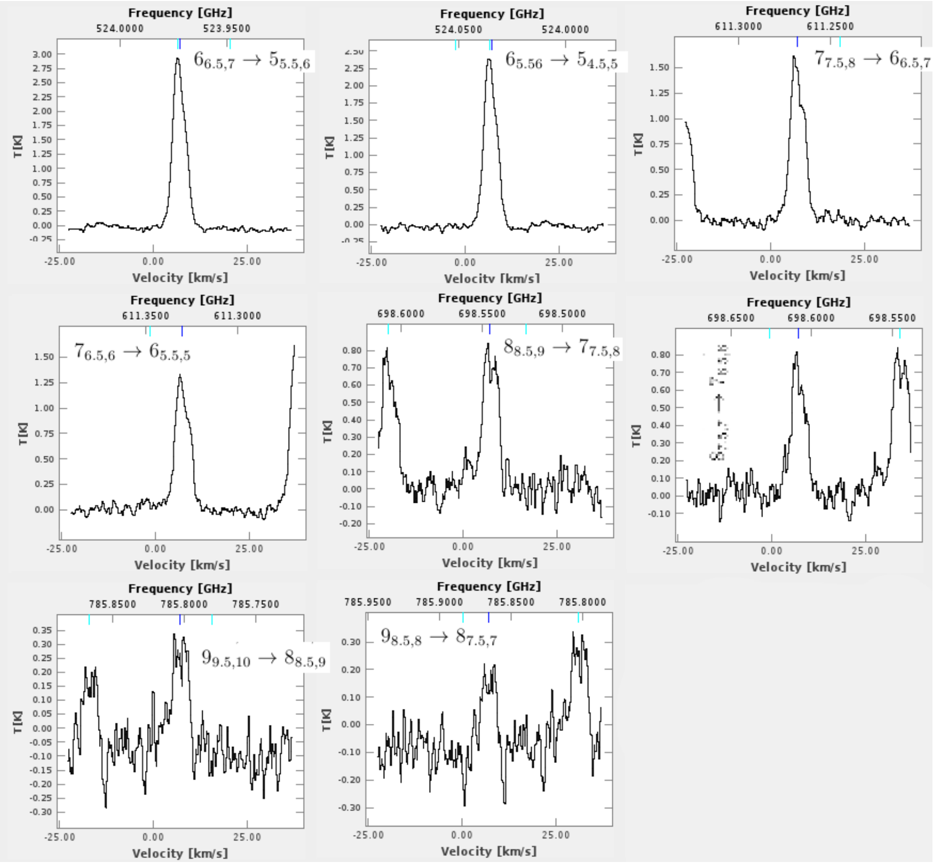

Figure 3.19: *Observed CCH lines.*

3.3.6 HCl & $H^{37}Cl$

The large rotational constant of HCl places its ground state rotational transition in FIR/sub-mm wavelength (Blake & Phillips 1985). This ground state transition lies at $\sim 526GHz$ which splits into three hyperfine components due to the quadrupole moment of ^{35}Cl. This splitting, see fig.3.20, not only allows us unambiguous identification but also can provides us with a determination of optical depth ground level (Schilke et al. 1995).

HCl has been previously observed by ground based telescopes (De Lucia et al. 1971). Hydrides like HCl are thought to be good coolants of the gas due to their large rotational constant and large separation of their energy levels.

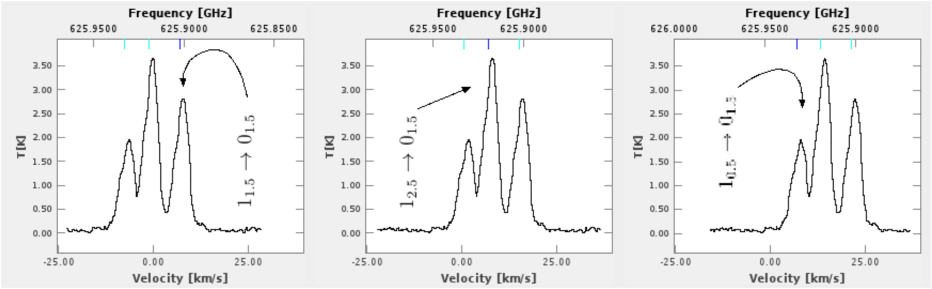

Figure 3.20: *Observed HCl lines.*

In $H^{37}Cl$ we also observe the ground state transition split into a triplet at the frequency of $\sim 624GHz$, see figure 3.21.

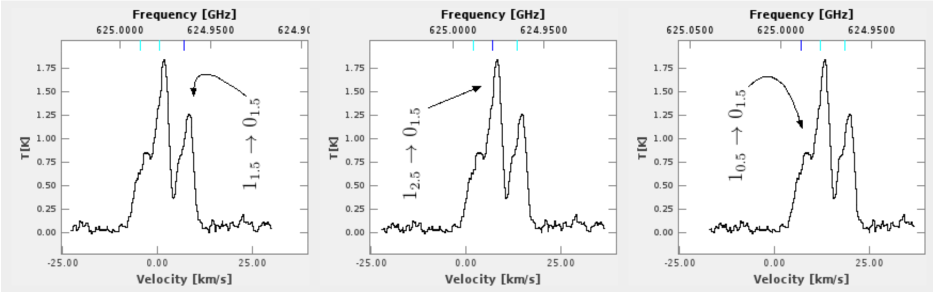

Figure 3.21: *Observed $H^{37}Cl$ lines.*

3.3.7 HCO^+ and isotopologues

HCO^+ is a linear molecule with a pure rotation spectrum. HCO^+ is a well known tracer of both dense molecular gas as well as outflows (Girart et al. 1999). HCO^+ has some of the strongest lines seen in our survey of Orion-S and comprise $\sim 5\%$ of the total flux, see table 3.2. Different transitions of HCO^+, see fig. 3.22, detected in the HIFI spectral survey, from $J = 6 - 5,\ E_{up} = 90K$ to $J = 13 - 12,\ E_{up} = 389K$ which respectively correspond to $n_{crit} \sim 3.2 \times 10^7$ to $n_{crit} \sim 6.0 \times 10^8$, can be used to probe a wide range of physical conditions in Orion-S.

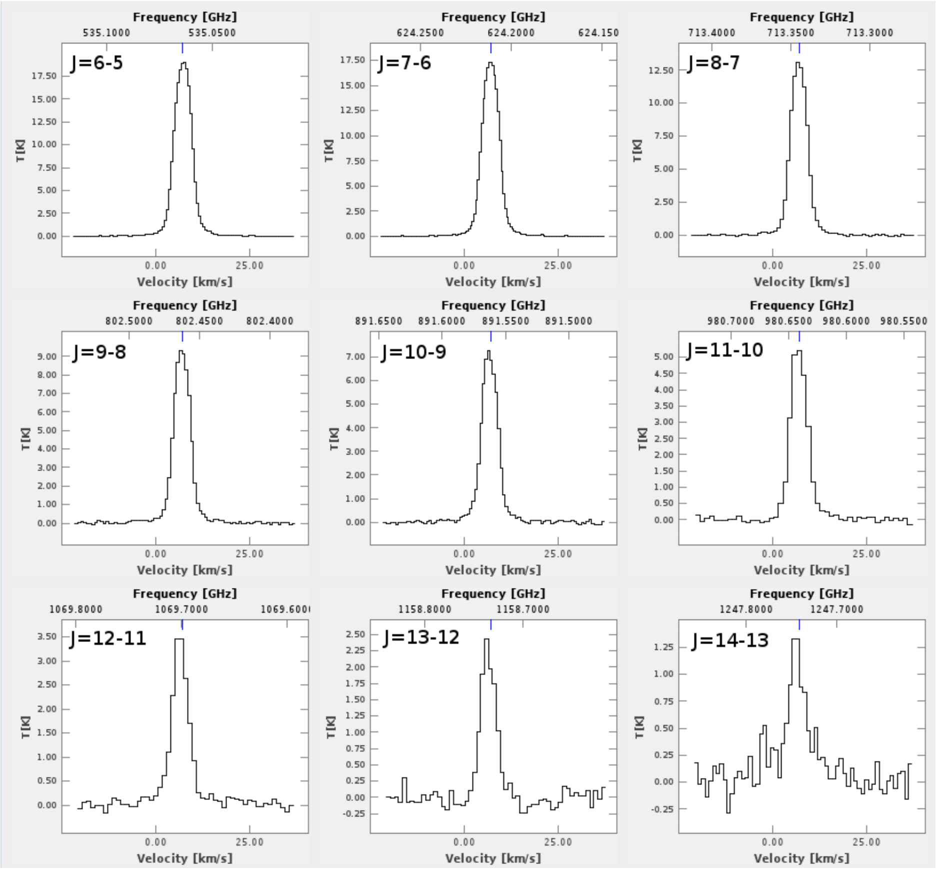

Figure 3.22: *Observed* HCO^+ *lines.*

The other identified isotopologues of this species are $H^{13}CO^+$ and $HC^{18}O^+$ shown respectively in figures 3.23 & 3.24. The total flux of these two radicals together are less than 0.15%, see table 3.2, which is lower than HCO^+ due to the abundances ratios, $[^{12}C/^{13}C] \sim 55$ & $[^{16}O/^{18}O \sim 500]$.

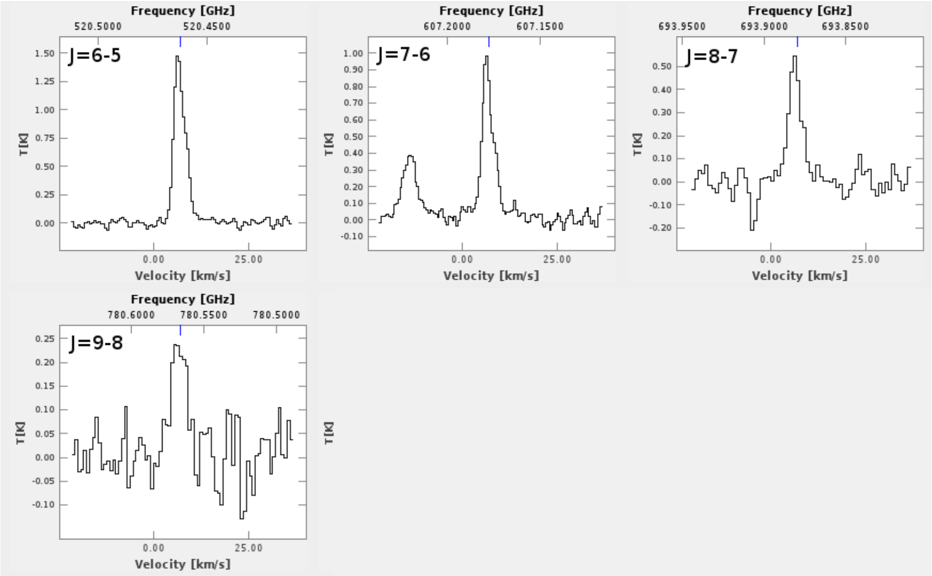

Figure 3.23: *Observed* $H^{13}CO^{+}$ *lines.*

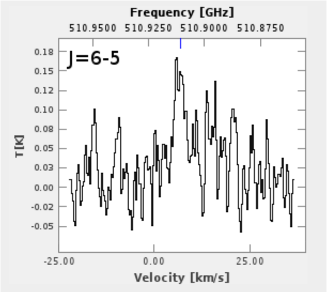

Figure 3.24: *Observed* $HC^{18}O^{+}$ *lines.*

3.3.8 $\boldsymbol{HCN}$, $\boldsymbol{HNC}$, and isotopologues

HCN is a particularly important linear molecule since it has pure rotational transitions at sub-mm wavelengths and ro-vibrational lines in the infra-red, both observable from the ground (Carr et al. 1995; van der Tak et al. 1999). HCN is one of the most abundant nitrogen bearing species in hot cores (Rodgers & Charnley 2001). HCN is thought to be a good tracer of hot cores in star formation regions since it is has been detected toward many massive star formation regions (Boonman et al. 2001). The different transitions of HCN, $J = 6 - 5$, $E_{up} = 89K$ to $J = 13 - 12$, $E_{up} = 387K$ which correspond to

$1.0 \times 10^9 < n_{crit} < 7.6 \times 10^9 cm^{-3}$ allow us to probe high density gas over a large temperature range.

For $J = 11 \rightarrow 10$ transition of HCN we did not fit two components due to its shape. Whereas to all other identified transitions of HCN, see fig 3.25, we fitted two Gaussian components (outflow and main), see table B.1.

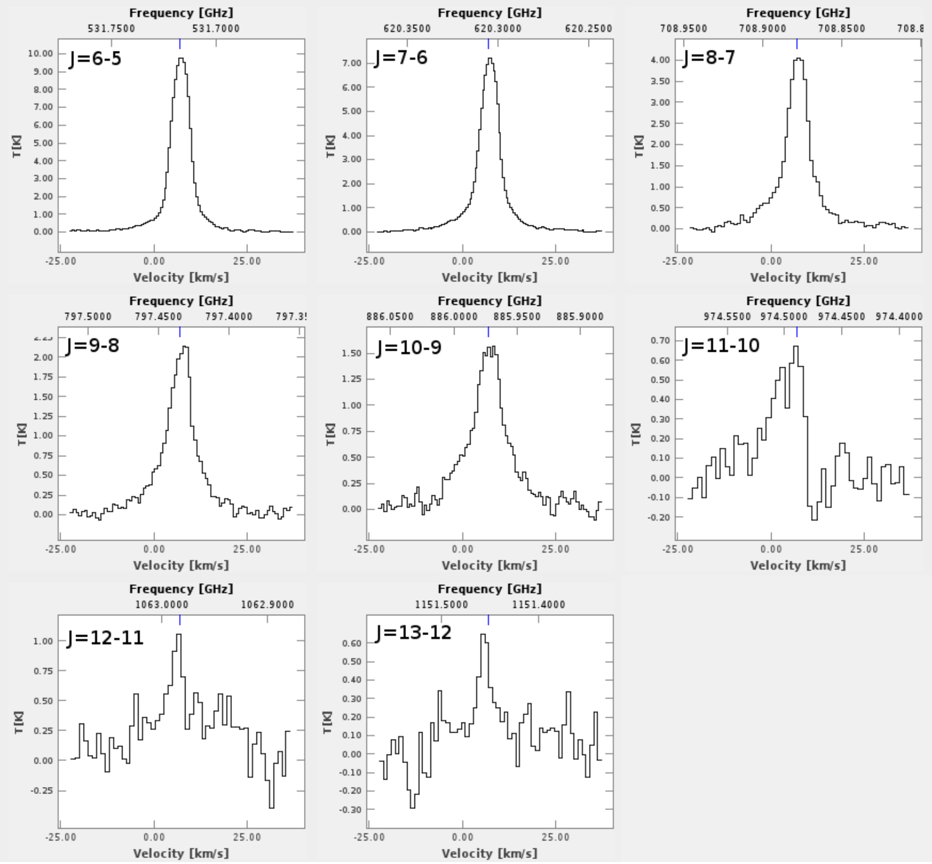

Figure 3.25: *Observed HCN lines.*

The only observed isotopologue is $H^{13}CN$, fig 3.26, which we see in the main (narrow) component but not in the outflow probably due to the lower ^{13}C abundances, $[^{12}C/^{13}C \sim 55]$.

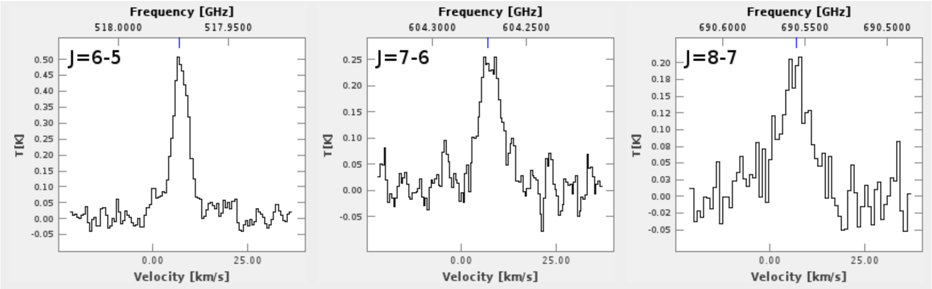

Figure 3.26: *Observed $H^{13}CN$ lines.*

HNC is the other linear species composed of atoms of hydrogen, nitrogen, and carbon. HNC, however, shows different physical and chemical properties than HCN. In the assumed temperature range of the cloud, HNC transitions, $J = 6-5,\ E_{up} = 91K$ to $J = 8-7,\ E_{up} = 156K$, the corresponding critical density lies in the range of $7.3 \times 10^7 < n_{crit} < 1.7 \times 10^8 cm^{-3}$. HNC can be a complement of HCN to trace dense cores. Values for the HNC/HCN abundance ratio can provide us an understanding of the physical condition of the cloud. Chemical modelling of Baan et al. (2008) shows that an abundance ratio greater than unity suggests a quiescent, low temperature gas, whereas the ratio below unity is consistent with the models of higher density, and higher temperature gas. This occurs because higher temperatures cause HNC to convert more effectively to HCN via the reaction of $HNC + H \rightarrow HCN + H$. This reshuffling reaction with the activation barrier of 200(K) is responsible for the change in the abundance ratio of HNC/HCN in higher temperature regions. Identified transitions of HNC are shown in figure 3.27.

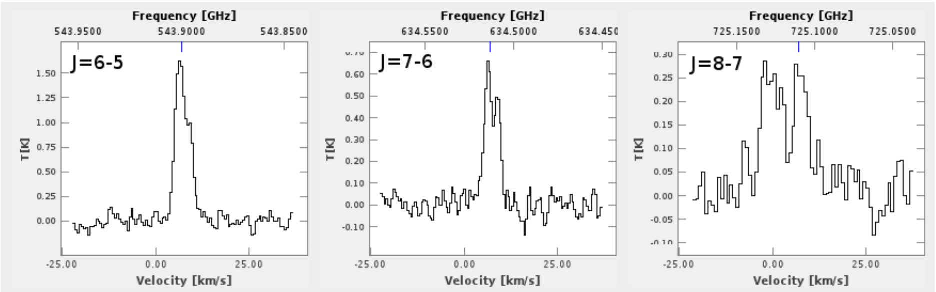

Figure 3.27: *Observed HNC lines.*

3.3.9 DCO^+ & DCN

DCO^+ & DCN are both linear molecules which can be considered as tracers of the chemical history of the deuteration processes in the interstellar medium. D/H ratios can change significantly with the temperature of the medium. This ratio tends to be higher for cold gas since low temperature fractionation reactions preferentially drive the chemistry towards deuterated species rather than their non-deuterated counterparts (Roberts et al. 2003). Studying DCO^+ can also provide us with the information to estimate the electron fraction in the dense gas and prestellar cores (Bergin, Plume, Williams and Myers 1999). Deuterated species toward Orion-S will be the focus of a future paper by Vastel et al. (2013). Identified transitions of DCO^+ & DCN are shown respectively in fig. 3.28 & 3.29.

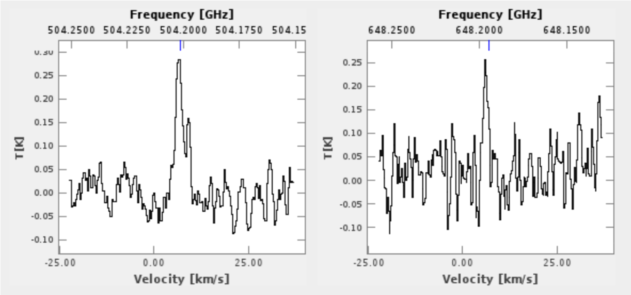

Figure 3.28: *Observed* DCO^+ *lines.*

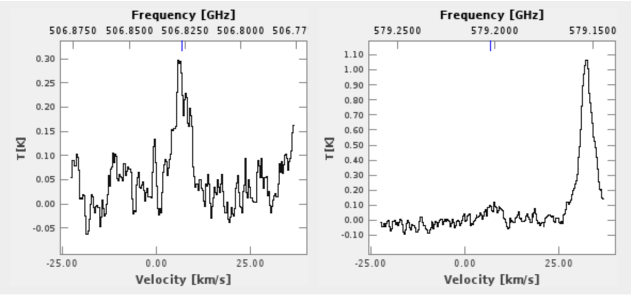

Figure 3.29: *Observed* DCN *lines.*

3.3.10 H_2O, $H_2^{18}O$, HDO

Although the water molecule has an axis of symmetry, its moment of inertia around the three rotational axes are different. Therefore water is an asymmetric rotor which makes its modelling complicated due to the sheer number of its quantum transitions (Melnick et al. 2000). Projection of total angular momentum, J, onto A and C inertial axis of the water molecule defines two other quanta, K_a & K_c, for water and its isotopologues, see tables B.1 & B.2. Also since the two H atoms can have *parallel* or *antiparallel* nuclear spins, the water molecule can be in *ortho* or *para* states that can be treated as two distinct molecules, see table B.3 and fig 3.30. Given the large number of transitions spanning a wide range of physical conditions, water is considered to be an excellent coolant of the gas in star forming regions (Ceccarelli et al. 1996). The abundance of water varies significantly in cold and warm regions since it can freeze onto the dust grains in cold regions and have enhanced production in warm regions (Boonman et al. 2003). Water can also be used as a tracer of shock heated gas (Neufeld & Melnick 1987). Figures 3.30,3.31, and 3.30 shows respectively all identified transitions of H_2O, $H_2^{18}O$, and HDO toward Orion-S, which are the focus of a future paper by Nagy et al. 2013.

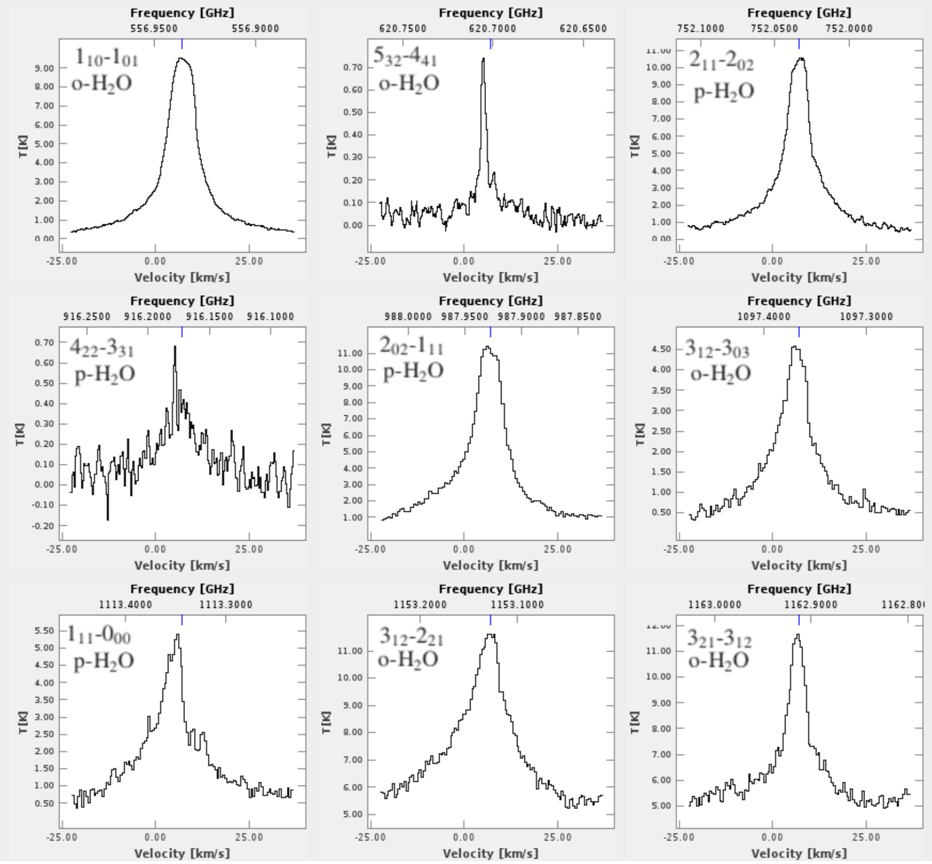

Figure 3.30: *Observed H_2O lines.*

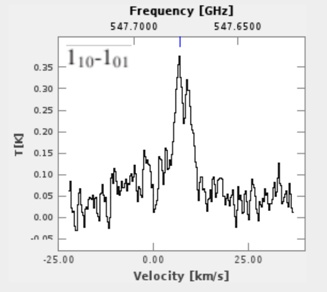

Figure 3.31: *Observed $H_2^{18}O$ line.*

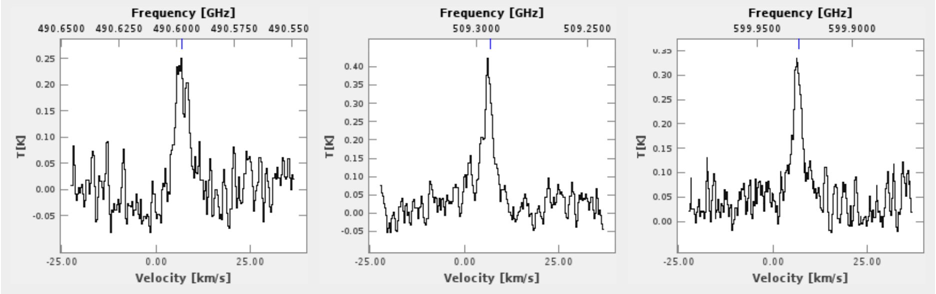

Figure 3.32: *Observed HDO lines.*

3.3.11 $\boldsymbol{o - NH_3}$

NH_3 is a symmetric top molecule meaning that the rotational inertia of the A & B axes are equal. NH_3 is observationally used to trace dense ($10^4\,cm^{-3}$) molecular clouds cores (Myers & Benson 1983), it is also a good temperature probe (Juvela et al. 2012). Due to the possible orientation of hydrogen spins, two distinct species of NH_3 exist, $o - NH_3$ & $p - NH_3$. Since there are three hydrogen atoms (rotation of 120° around the symmetry axis) it turns out that the molecule is *ortho* if K is a multiple of 3. As figure 3.33 shows we observe one ammonia line toward Orion-S. As table B.1 shows this line also exhibits an outflow component with a velocity of $\sim 9\,kms^{-1}$.

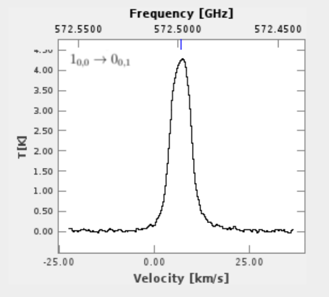

Figure 3.33: *Observed $o - NH_3$ line.*

3.3.12 $\boldsymbol{N_2H^+}$

N_2H^+ is a well known tracer of cold, dense gas in the interstellar medium, since it does not freeze onto dust grains as readily as many other molecules (Womack et al. 1992). It has been detected in a variety of different regions as well such as protostellar cores (Caselli et al. 2002) and PDRs (Fuente et al. 2005). We see a number of high J transitions of N_2H^+, see figure 3.34, which shows transitions from $J = 6-5,\ E_{up} = 94K$ to $J = 10-9,\ E_{up} = 246K$ and critical densities of $2.9 \times 10^7 < n_{crit} < 1.5 \times 10^8$.

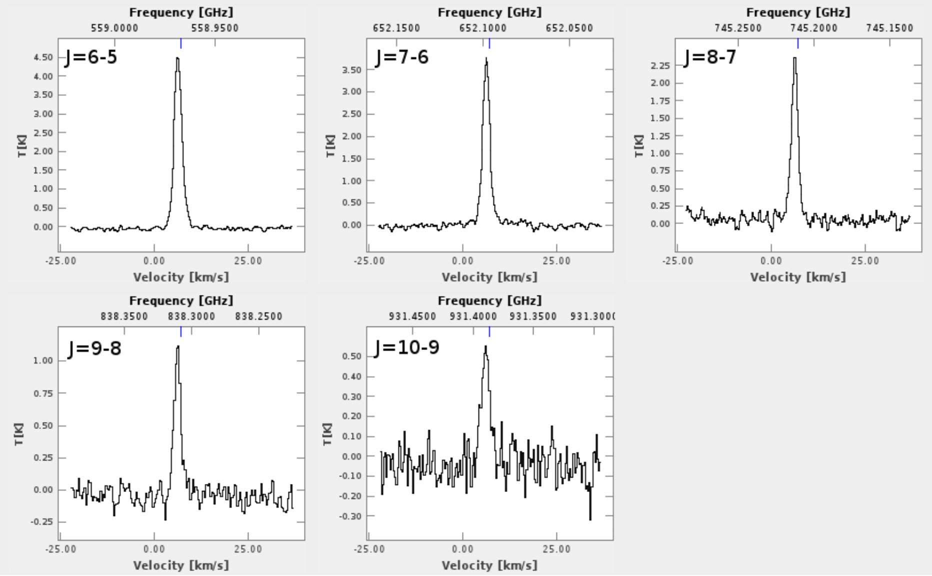

Figure 3.34: *Observed N_2H^+ lines.*

3.3.13 $\boldsymbol{o - H_2CO}$ & $\boldsymbol{p - H_2CO}$

Formaldehyde, H_2CO is a near symmetric rotor where the small asymmetry around the $C-O$ axis causes splitting of the energy levels into two K doublets, K_a & K_c, see table B.1. In addition hydrogen atom spins causes the molecule to be divided into two distinct *ortho* and *para* molecules. H_2CO is also well known for its rotational transition below the cosmic radiation temperature, 2.7 K (Palmer et al. 1969).

The first nine identified transitions of ortho and para formaldehyde are shown respectively in figures 3.35 and 3.36. At the frequency of 509.565GHz, the $o - H_2CO$ transition is blended of methanol lines so we excluded it from the analysis and this figure. Ortho and para formaldehyde transitions together comprise less than 3 % of total received flux.

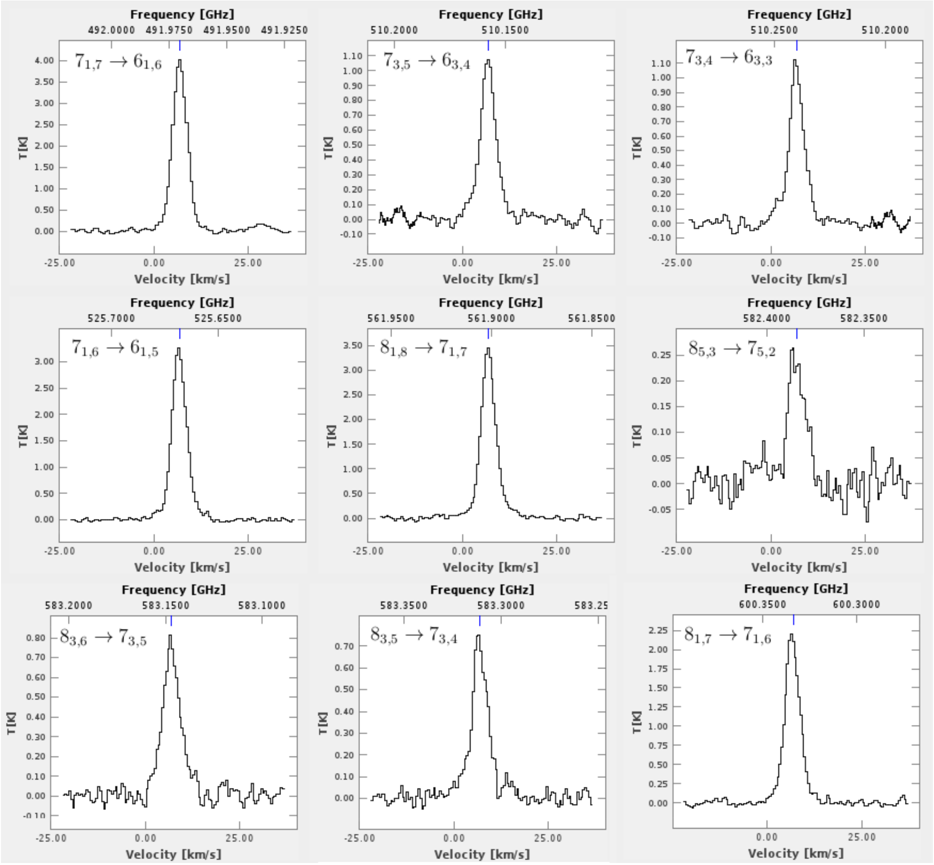

Figure 3.35: *Observed* $o-H_2CO$ *lines.*

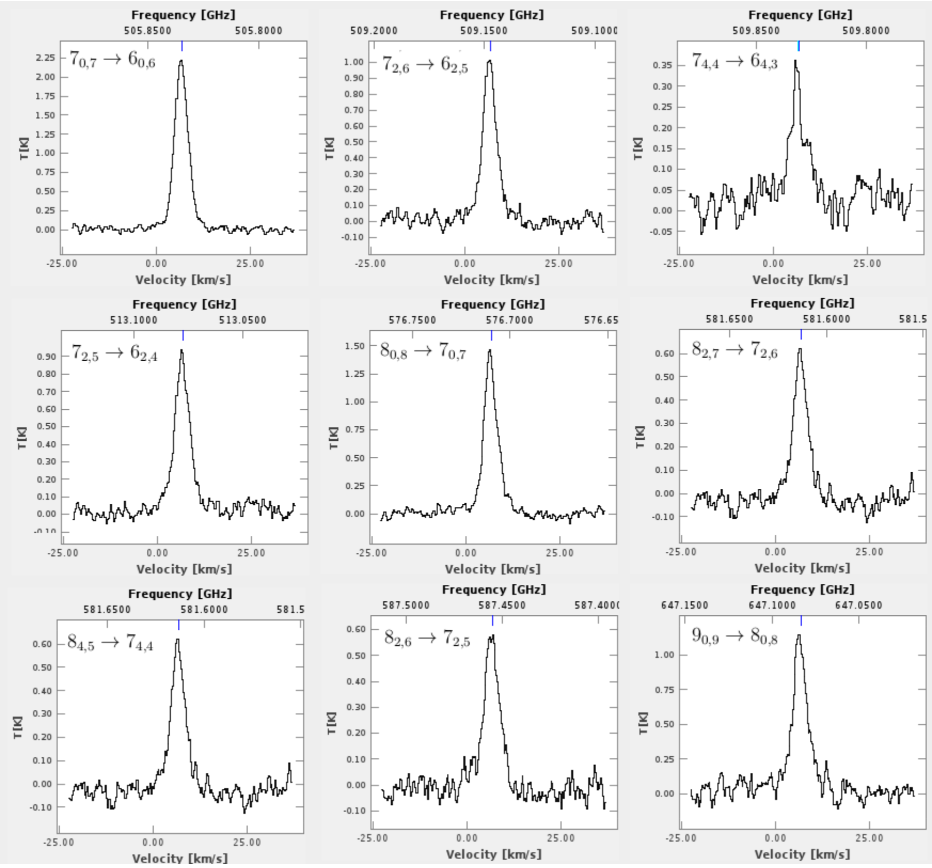

Figure 3.36: *Observed $p-H_2CO$ lines.*

3.3.14 H_2S

H_2S is an asymmetric rotor which like H_2O shows ortho and para separation. Hydrogen sulfide is considered to be a tracer of high temperature chemistry and grain surface temperature chemistry (Watson & Walmsley 1982). H_2S comprises less than 1% of the total received integrated line toward Orion-S. Figure 3.37 shows all identified transitions of H_2S which are again contaminated with emission in the off position.

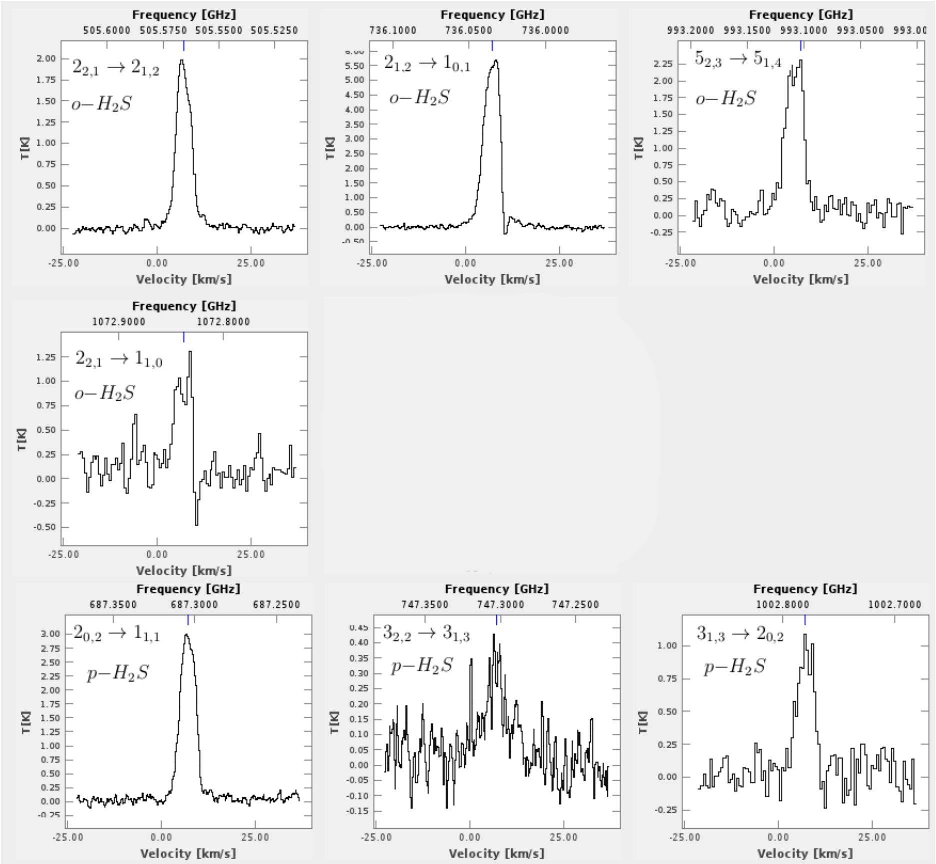

Figure 3.37: *Observed H_2S lines.*

3.3.15 ***SiO***

SiO is a linear molecule which comprises less than 0.05% of the total received flux. *SiO* abundances are enhanced in hot and shocked regions (Iglesias & Silk 1978) and so *SiO* emission is often used as a tracer of molecular outflows since the *SiO* emission will preferentially trace the outflow material itself, rather than the dense protostellar core (Martin-Pintado et al. 1992). This is mainly due to *Si* bearing dust grains being shattered by the outflow, followed by a rapid gas phase reaction with free oxygen to produce *SiO*. We could observe only one identified transition of *SiO* toward Orion-S which is above 5σ, see figure 3.38.

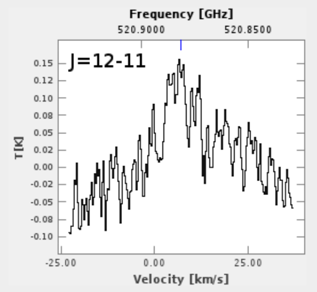

Figure 3.38: *Observed SiO lines.*

3.3.16 ***SO***

SO is a linear radical in which all rotational transitions split into three states since the total spin quantum number is $S = 1$, see table B.1. Figure 3.39 shows first nine identified transitions of *SO* with HIFI, which comprise $\sim 1\%$ of the total flux. *SO* is found in molecular clouds associated with *HII* regions (Gottlieb et al. 1978), and dense cores of dark clouds(Swade 1989).

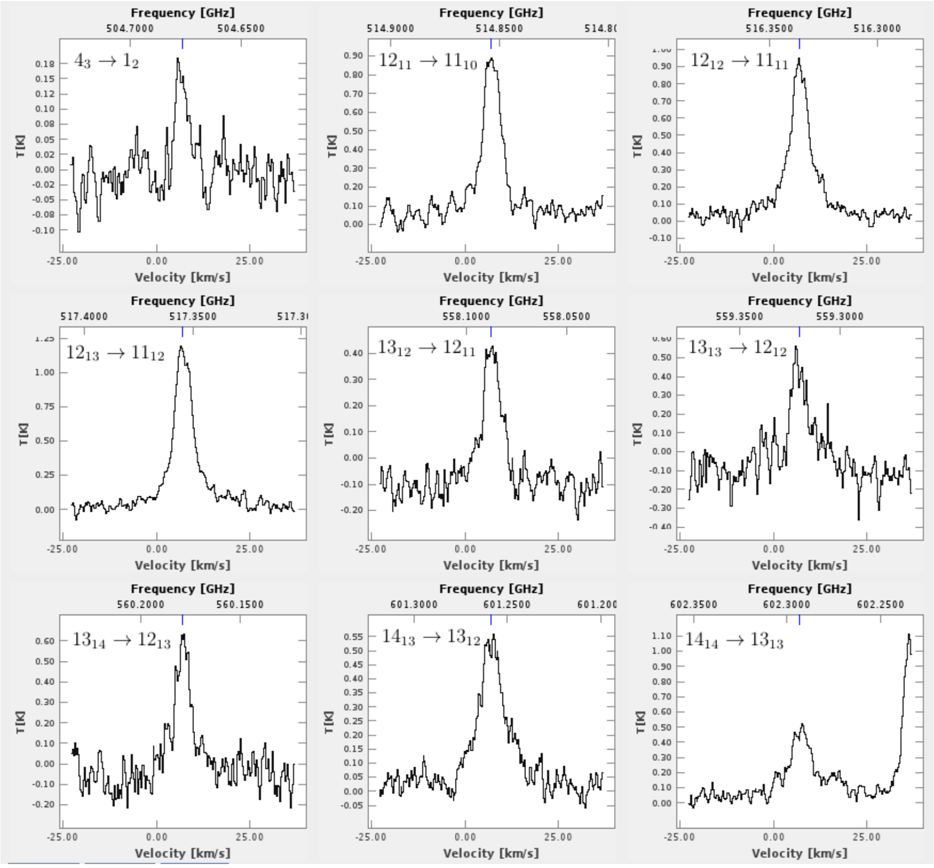

Figure 3.39: *Observed SO lines.*

3.3.17 SO_2

SO_2 is an asymmetric molecule that forms through the conversion of SO by OH. SO2 emission comprises ~ 0.2% of the total received flux. This molecule has been found to be abundant in warm molecular clouds (Schilke et al. 2001). Figure 3.40 shows the first nine observed transitions of SO_2.

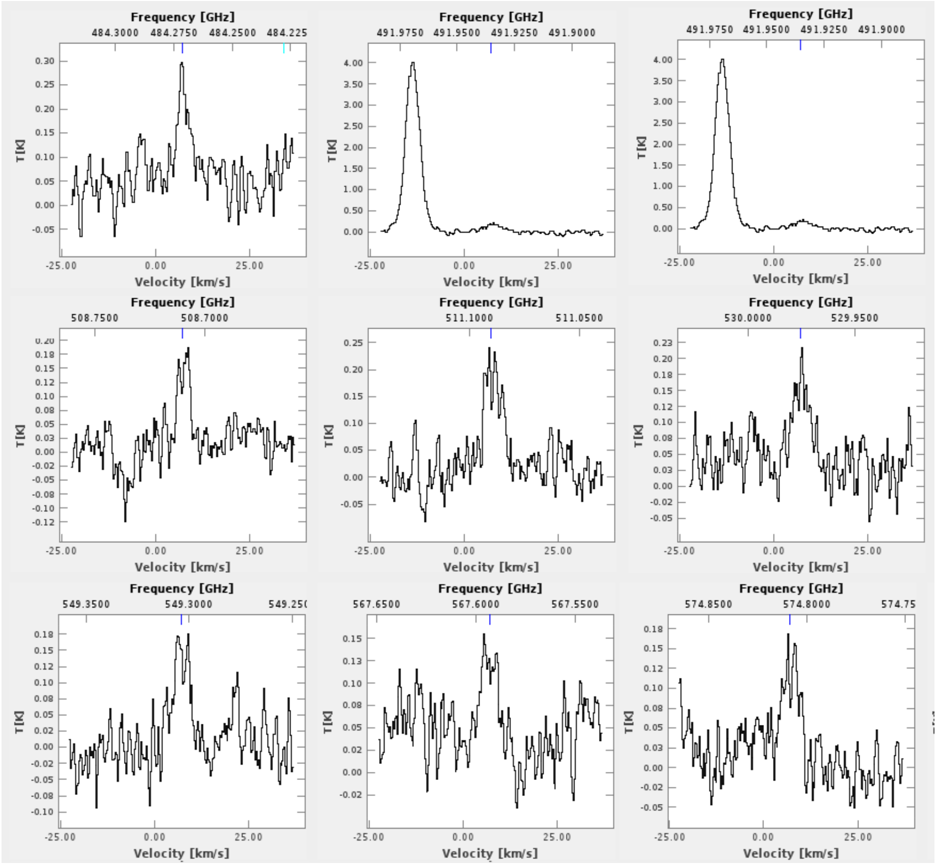

Figure 3.40: *Observed SO_2 lines.*

3.3.18 $E - CH_3OH$ & $A - CH_3OH$

Methanol is an asymmetric top molecule. The methyl group ($-CH_3$) has three equivalent H atoms where the combination of the spin of these three hydrogen atoms can create two distinct molecules $E - CH_3OH$ & $A - CH_3OH$. The A state corresponds to all spins being parallel while E state means one is in the opposite direction than the other two spins. Although methanol is a asymmetric top, it is nearly a prolate top and its rotational energy can be labelled by K ladders, instead of K_a & K_c. Table B.1 shows all quantum numbers of methanol transitions including vibrational state and parity. We observe more than 400 transitions of methanol toward Orion-S listed in table B.1. Methanol is a good temperature probe (Beuther et al. 2005) since its large number of observable transitions lend itself nicely to a rotation diagram analysis (see Chapter 4 and also Wang et. al. 2011). Methanol in Orion-S will be the subject of a future paper (Tahani et al. 2013)

Chapter 4

Analysis

Using the HIFI spectral scan data from the HEXOS Guaranteed Time Key Project, we identified 47 different species producing more than 800 different transitions in the frequency range of 479-1906GHz. After detecting and identifying each transition and fitting Gaussian line profiles to each individual transition, we may now utilize these results to begin to examine the physical conditions of the gas in Orion-S, e.g column density, gas temperature, source size, etc. Different methods, which are explained in this chapter, will be employed. We will first introduce the *rotation diagram* and *population diagram* methods and then we will compare these results with a more time consuming and more sophisticating modelling method, known as *LTE* modelling.

4.1 Rotation Diagram versus Population Diagram

Theoretically, the abundance of a molecular species can be determined from observations of a single transition. In LTE, the distance over which temperature changes occur is large compared to the distances travelled by particles and photons between collisions (i.e. their mean free path). Thus, the particles and photons cannot escape the local environment and are confined to a "box" of constant temperature. In that confined "box" the particles and black-body radiation come into equilibrium with each other and so can be described by a single temperature. Therefore, in LTE the population of any molecular energy level is given by the Boltzmann equation:

$$\frac{n_u}{n_0} = \frac{g_u}{g_0} e^{-E_u/kT_{ex}} \tag{4.1}$$

where E_u is the sum of the electronic, vibrational, and rotational energies of that state, n_0 is the population density of the ground state, g_u is the degeneracy of state u, k is the Boltzmann constant and T_{ex} is the excitation temperature. If the gas is truly in LTE then T_{ex} is the kinetic temperature of the gas. If the gas is not in LTE then the excitation temperature used to satisfy the Boltzmann population distribution will not necessarily reflect the actual kinetic temperature of the gas. Summing over all states gives the total molecular density (n_t):

$$n_t = \frac{n_0}{g_0} \sum_{i=0}^{\infty} g_i e^{-E_i/kT_{ex}} \tag{4.2}$$

And the partition function is defined as:

$$Z(T) = \sum_{i=0}^{\infty} g_i e^{-E_i/kT_{ex}} \tag{4.3}$$

Using the equations 4.1, 4.2, and 4.3 we can show that:

$$n_u = \frac{n_t}{Z(T)} g_u e^{-E_u/kT_{ex}} \tag{4.4}$$

Equation 4.4 is an expression of the density in one state in terms of total density.

Knowing these basics can provide us with a better understanding of the concept of critical density, introduced in chapter 3. As shown in a simplified two level system in fig 4.1, there are three radiative processes that can populate and depopulate an energy level. First, there is spontaneous decay from the upper state u to the lower state l. The transition probability is given by the Einstein spontaneous emission coefficient, A_{ul}. A transition from a higher state to a lower state is accompanied by the emission of a photon whose energy corresponds to the energy difference between the two states ($E = h\nu$).

A second mechanism for inducing a level chance occurs through the absorption of a photon. This transition depends on the local radiation rate, U, and the Einstein induced

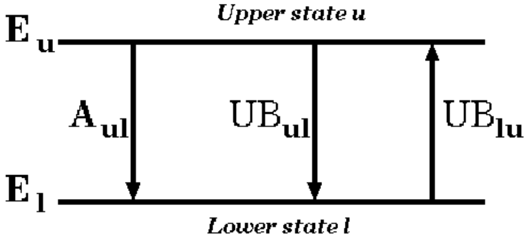

Figure 4.1: *Two level state.*

absorption coefficient, B_{lu}.

A second downward process is stimulated emission defined by the B_{ul} coefficient. In a steady state the number of emissions and absorptions must be equal. Therefore:

$$n_u A_{ul} + n_u B_{ul} U = n_l B_{lu} U \tag{4.5}$$

By mean of equation 4.5, and 4.1 and the comparison to the Planck function we can find the relation between the Einstein's coefficients:

$$g_u B_{ul} = g_l B_{lu} \tag{4.6}$$

and;

$$A_{ul} = \frac{2h\nu^3}{c^2} B_{ul} \tag{4.7}$$

Recalling the equation of transfer from chapter 1, eq.1.17, can be rewritten in terms of the Planck function as:

$$B(T_B) = B(T_{bg})e^{-\tau} + B_\nu(T_K)(1 - e^{-\tau}) \tag{4.8}$$

where $B(T_B)$ is the observe intensity, $B(T_{bg})$ is the intensity of the background radiation, and $B_(T_K)$ is the source function (intensity) of the gas cloud.In the optical thin limit with no background radiation, this can be rewritten as

$$B(T_B) = \tau B(T_K) \tag{4.9}$$

However, from equation 1.10 in chapter 1 τ is given by;

$$\tau = \int \kappa \mathrm{d}s \tag{4.10}$$

Also by the definition of the absorption coefficient κ we can simply say it is the probability of the absorption of an incident photon by the medium in a solid angle (4π) per unit volume per unit time:

$$\kappa_\nu = \frac{h\nu}{4\pi}[n_l B_{lu} - n_u B_{ul}]\phi_\nu \tag{4.11}$$

Using the relation between Einstein values, equations 4.6 & 4.7, and equations 4.1, and 4.11 we can show that:

$$B(T_B) = \tau B(T_K) = \int \kappa_\nu \mathrm{d}s B(T_K) = \int \frac{h\nu}{4\pi}[n_l B_{lu} - n_u B_{ul}]\phi \mathrm{d}s \left(\frac{2h\nu^3}{c^2}\frac{1}{e^{h\nu/kT}-1}\right) \tag{4.12}$$

By equations 4.1 & 4.6:

$$B(T_B) = \int \frac{h\nu}{4\pi}[e^{h\nu/kT}-1] n_u B_{ul}\phi \mathrm{d}s \left(\frac{2h\nu^3}{c^2}\frac{1}{e^{h\nu/kT}-1}\right)$$

also using equation 4.7 and a little algebra we can show that:

$$\begin{aligned} B(T_B) &= \int \frac{h\nu}{4\pi}[e^{h\nu/kT}-1] n_u \frac{c^2}{2h\nu^3} A_{ul}\phi \mathrm{d}s \left(\frac{2h\nu^3}{c^2}\frac{1}{e^{h\nu/kT}-1}\right) \\ &= \frac{h\nu}{4\pi} N_u \frac{c^2}{2h\nu^3} A_{ul}\phi \left(\frac{2h\nu^3}{c^2}\frac{e^{h\nu/kT}-1}{e^{h\nu/kT}-1}\right) \end{aligned}$$

Therefore;

$$B(T_B) = \frac{h\nu}{4\pi} N_u A_{ul}\phi_\nu \tag{4.13}$$

where N_u is the column density (cm^{-2}) of particles in the upper state given by $N_u = \int n_u \mathrm{d}s$. In the radio regime where $h\nu << kT$ the Planck's function can be rewritten as:

$$B(T_B) = \frac{2k\nu^2}{c^2} T_B = \frac{h\nu}{4\pi} N_u A_{ul}\phi_\nu \tag{4.14}$$

Rearranging equation 4.14 in terms T_B and integrating both sides of equation with respect to the frequency we can show that;

$$\int T_B \mathrm{d}\nu = \frac{hc^2}{8k\pi\nu} N_u A_{ul} \int \phi(\nu)\mathrm{d}\nu = \frac{hc^2}{8k\pi\nu} N_u A_{ul} \tag{4.15}$$

where ϕ is a Gaussian line profile which is normalized to one over integration with respect to ν, $\int \phi \mathrm{d}\nu = 1$. Also, by changing frequency ν to velocity (V) using the Doppler shift equation we can modify the left hand side of this equation to;

$$\int T_B \mathrm{d}\nu = \frac{\nu}{c} \int T_B \mathrm{d}V \tag{4.16}$$

Therefore, from equations 4.15 & 4.16;

$$N_u = \frac{8k\pi\nu^2}{hc^3} \frac{1}{A_{ul}} \int T_B \mathrm{d}V = \zeta_u \mathbb{W} \tag{4.17}$$

where for simplicity we define;

$$\begin{aligned} \zeta_u &= \frac{8k\pi\nu^2}{hc^3} \frac{1}{A_{ul}} \\ \mathbb{W} &= \int T_B \mathrm{d}V \end{aligned} \tag{4.18}$$

Therefore, the column density in the upper state is purely dependent on the integrated intensity (as given in table B.1 in the results chapter), and some fundamental constants. Also, if we assume the system is in LTE, we can use the partition function to obtain the total column density by using equation 4.2;

$$N_t = \frac{N_u}{g_u} \frac{\sum\limits_{i=0}^{\infty} g_i e^{-E_i/kT}}{e^{-E_u/kT}} = \frac{N_u}{g_u} \frac{\mathcal{Z}}{e^{-E_u/kT}} \tag{4.19}$$

where N_t is the total column density reported in terms of column density of the upper energy state N_u, and $\mathcal{Z}$ is the partition function.

The *rotation diagram* method is a derivative of the above method that employs multiple observed transitions as opposed to simply using a single transition of a molecular species.

Substituting equation 4.17 into equation 4.19 after some algebra it can be shown that;

$$N_t \frac{g_u}{\mathcal{Z}} \frac{hc^2}{8k\pi\nu} A_{ul} e^{-E_i/kT} = N_t C e^{-E_i/kT} = \int T_B \mathrm{d}v \tag{4.20}$$

Or in a logarithmic scale:

$$-\frac{1}{T}\frac{E_u}{k} + b = ln(\int T_B \mathrm{d}v) \tag{4.21}$$

where b & C are constants given by $C = \frac{g_u}{\mathcal{Z}} \frac{hc^2}{8k\pi\nu} A_{ul}$ & $b = ln(CN_t)$. This equation is essentially a linear equation of the form $mx + b = y$, where here $-\frac{1}{T} \equiv m$, $\frac{E_u}{k} \equiv x$, and $ln(\int T_B \mathrm{d}v) \equiv y$. So the slope of a plot of $ln \int T_B \mathrm{d}V$ versus E_l/k yields a measure of the excitation temperature of the molecular cloud and the "y" intercept measures the total column density. This technique is called a *rotation* diagram and the excitation temperature is often referred to as a rotation temperature, mainly because this technique is often applied to the rotational transitions of molecules. If the molecule is in LTE then the excitation/rotation temperature is equivalent to the kinetic temperature. Using equations 4.2 & 4.17 we can rewrite equation 4.21 as:

$$-\frac{1}{T}\frac{E_u}{k} + ln(N_t) - ln(\mathcal{Z}) = ln(\frac{N_u}{g_u}) = ln(\frac{\zeta_u \mathbb{W}}{g_u}) \tag{4.22}$$

Figure 4.2 shows the rotation diagram plotted for ^{13}CO, which is a plot of equation 4.22, $ln(\frac{N_u}{g_u})$ versus E_u. Therefore, the slope of this graph is inversely proportional to the temperature, and therefore we can find column density, N_t.

A rotation diagram is a useful tool to extract physical conditions of the gas if it is optically thin, which may not always be the case. In an optically thick case we use the original form of equation 4.8 for the cloud and add an extra term to account for coupling between the beam size and the source size:

$$B(T_B) = B(T_K)(\frac{\Delta\Omega_a}{\Delta\Omega_s})(1 - e^{-\tau}) = B(T_K)\tau(\frac{\Delta\Omega_a}{\Delta\Omega_s})(\frac{1 - e^{-\tau}}{\tau}) \tag{4.23}$$

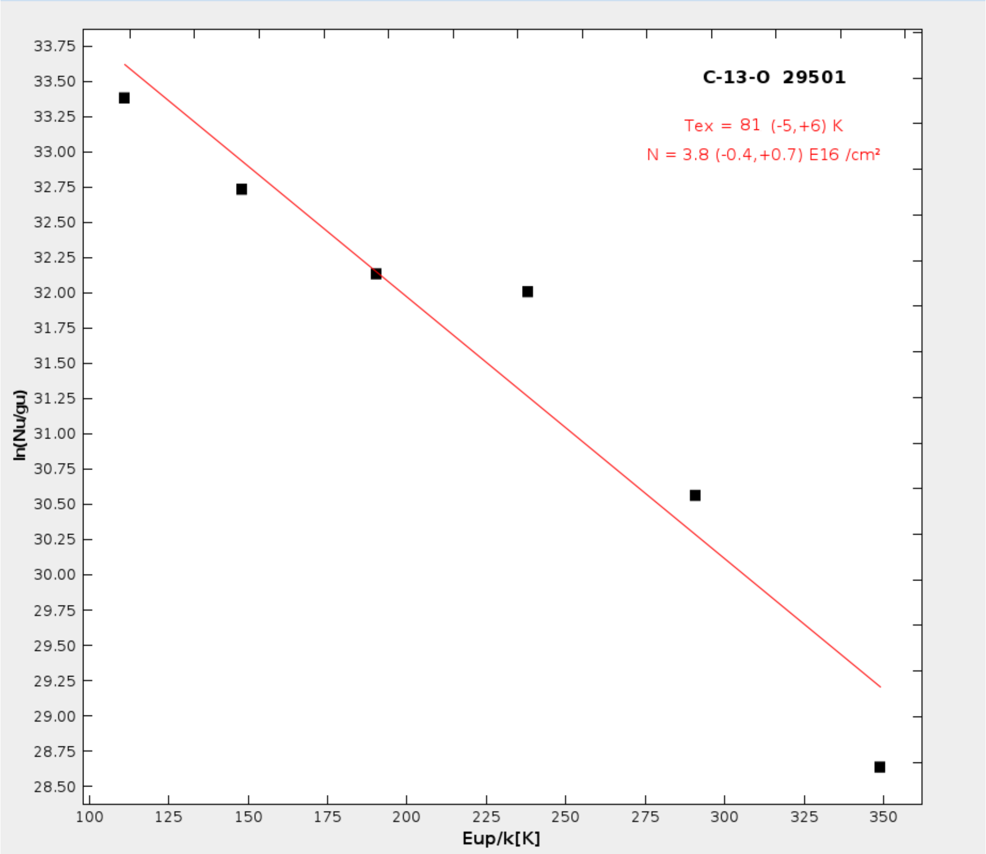

Figure 4.2: *Figure shows rotation diagram for* ^{13}CO*. The points represent the observed integrated intensities converted to* N_u/g_u *assuming optically thin LTE conditions, and the red line is the best fit straight line to the data. The invests slope provides the excitation temperature and the y intercept provides the total column density.*

where the factor $(\frac{\Delta\Omega_a}{\Delta\Omega_s})$ is known as the beam dilution factor and accounts for emission regions that may be smaller than the resolution of the telescope (i.e. the telescope beam size). The brightness temperature of the black body is equal to its thermodynamic temperature if it fills the telescope beam (and it is optically thick), otherwise this temperature is lowered by the solid angle of the source divided by the solid angle of the telescope beam (and further modified by the opacity). Comparison with equations 4.12 & 4.14 suggest that we can derive:

$$B(T_B) = \frac{2k\nu^2}{c^2}T_B = \frac{h\nu}{4\pi}N_u A_{ul}\phi_\nu \frac{1-e^{-\tau}}{\tau}(\frac{\Delta\Omega_a}{\Delta\Omega_s}) \qquad (4.24)$$

After some algebra it can be shown that:

$$N_u = \frac{8k\pi\nu^2}{hc^3}\frac{1}{A_{ul}}\int T_B \mathrm{d}v \frac{\tau}{1-e^{-\tau}}(\frac{\Delta\Omega_s}{\Delta\Omega_a}) \tag{4.25}$$

Thus;

$$-\frac{1}{T}\frac{E_u}{k} + ln(N_t) - ln(\frac{\tau}{1-e^{-\tau}}) - ln(\frac{\Delta\Omega_s}{\Delta\Omega_a}) + b' = ln(\int T_B \mathrm{d}v) \tag{4.26}$$

where b' is a constant:

$$b' = ln\left(\frac{A_{ul}hc^3}{8k\pi\nu^2}\frac{g_u}{\mathcal{Z}}\right) \tag{4.27}$$

Additional terms in equation 4.26 would correct equation 4.21 for optical depth effects and beam dilution factors. The corresponding graph is known as *the population diagram.* In comparison with equation 4.22 this can also be written as:

$$ln(\frac{N_u^{model}}{g_u}) = -\frac{1}{T}\frac{E_u}{k} + ln(N_t) - ln(\mathcal{Z}) - ln(\frac{\tau}{1-e^{-\tau}}) - ln(\frac{\Delta\Omega_s}{\Delta\Omega_a}) = ln(\frac{\zeta_u \mathbb{W}}{g_u}) \tag{4.28}$$

where N_u^{model} is N_u/g_u corrected for opacity and beam filling factor effects.

4.2 Population Diagram Results

In this section we explain how we can use the population diagram method to extract the temperature, column density, opacity, and source size of the molecular emission regions using our observed integrated intensities. Then in next section we compare these results with a much more sophisticated but time-consuming modelling technique to test the robustness of the population diagram method.

Equation 4.28 makes a link between our model and observations, and can be rewritten as:

$$ln(\frac{N_u^{model}}{g_u}) = ln(\frac{\eta_u \mathbb{W}}{g_u}) = ln(\frac{N_u^{observation}}{g_u}) \tag{4.29}$$

While the rotation diagram method requires a simple linear fit to the observations, solving the population diagram is a slightly more complicated problem and requires a computational approach. Since in equation 4.28 the free parameters are N_t, T, and source size (τ is determined once we select N_t and T) we can create a 3 dimensional grid in which, for each combination of these three parameters we predict an observed integrated intensity (and therefore N_u^{model}/g_u) for each observed transition. Then we use a χ^2 minimization technique to determine the combination of parameters that provides the best match between the model and the observations (i.e. $N_u/g_u = \eta\mathbb{W}$ as given in eq 4.22). Since the number of degrees of freedom, ρ, for each species is known we can define χ^2 as:

$$\chi^2 = \frac{1}{\rho}\left(\frac{N_u^{model} - N_u}{dN_u}\right)^2 \tag{4.30}$$

Therefore, by using a computer code we can calculate τ and therefore find N_u^{model}/g_u for each point at the defined three dimensional grid $N_t \times T \times \Delta\Omega_s$. Based on observation N_u/g_u is known, (see also equation 4.29), and we can find the best result by finding the model that produces the minimum χ^2 from equation 4.30. To show the method explicitly, we will work through the problem for the easiest case, *linear molecules*. Knowing that the spontaneous emission coefficient, A_{ul}, from rotational state J+1 to J is given by:

$$A_{ul} = \frac{64\pi^4\nu^3}{3hc^3}\mu^2\frac{J_u}{2J_u+1} \tag{4.31}$$

where μ is the permanent dipole moment of the molecule. We can find τ;

$$\begin{aligned}\tau &= \int \kappa \mathrm{d}s = \int \frac{h\nu}{4\pi}\left(n_u\frac{g_l}{g_u}\frac{g_u}{g_l}B_{ul}e^{E_u/kT} - n_u B_{ul}\right)\phi_\nu \mathrm{d}s \\ &= \frac{h\nu}{4\pi}(e^{E_u/kT}-1)N_u(\frac{c^2}{2h\nu^3})A_{ul}\phi_\nu = \frac{c^2}{8\pi\nu^2}A_{ul}(e^{E_u/kT}-1)\frac{N_t}{\mathcal{Z}}g_u e^{-E_u/kT}\phi_\nu \\ &= (1-e^{-E_u/kT})\frac{8\pi^3\nu}{3hc}\mu^2\frac{N_t g_u}{\mathcal{Z}}\phi_\nu\end{aligned} \tag{4.32}$$

So, in our 3D cube, we pick a range of N_t, from some minimum value to some maximum value and provide a step size. We do the same for T and for source size. Then, we use a computer code which loops through all possible combinations of N_t, T, and source size. The code then begins by calculating N_u/g_u for each transition via the rotation diagram method (equation 4.29). At each cube point, the code calculates τ for each observed transition (via equation 4.32) and then calculates N_u^{model}/g_u (via equation 4.25). The code then calculates the χ^2 value of that cube point via equation 4.30. Finally, we select the cube point (i.e the combination of parameters) with the lowest value of χ^2 as the model which best fits the observations. Often, in procedure, we begin with a very large cube that is coarsely sampled to find a rough region of parameter space that contains the solution. We then zoom in on the solution space and run the code a second time with a much smaller range of parameters with a much finer grid.

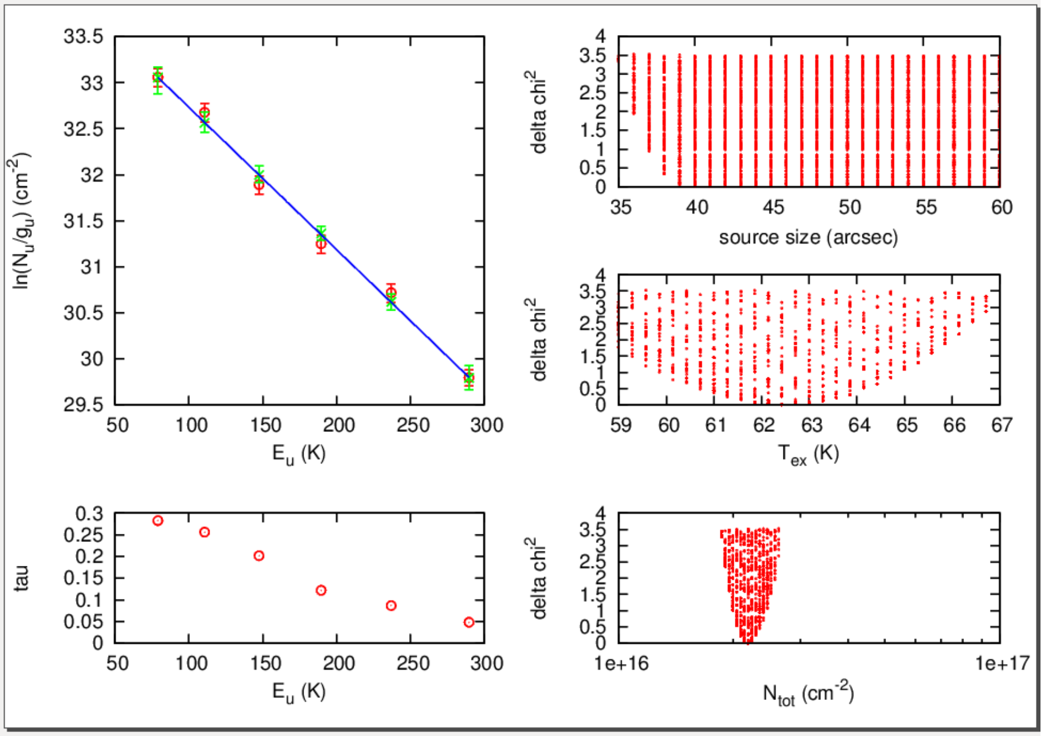

Figure 4.3: *Figure shows the population diagram of* $C^{18}O$. *The green stars show the* N_u^{model}/g_u *values from the best fit population diagram model. The red circles show the rotation diagram* N_u/g_u *data points and the blue line shows the rotation diagram linear fit. The figure on the bottom left shows the value of the opacity in each transition as calculated from the best fit model. On the right we show* χ^2 *"surface plots" which show the value of* χ^2 *(or rather* $\delta\chi^2$ *which is given by* $\delta\chi^2 = \chi^2_{step} - \chi^2_{best}$*) vs the three parameters for each point in our cube: source size (top right), T (middle right), and N (bottom right)*

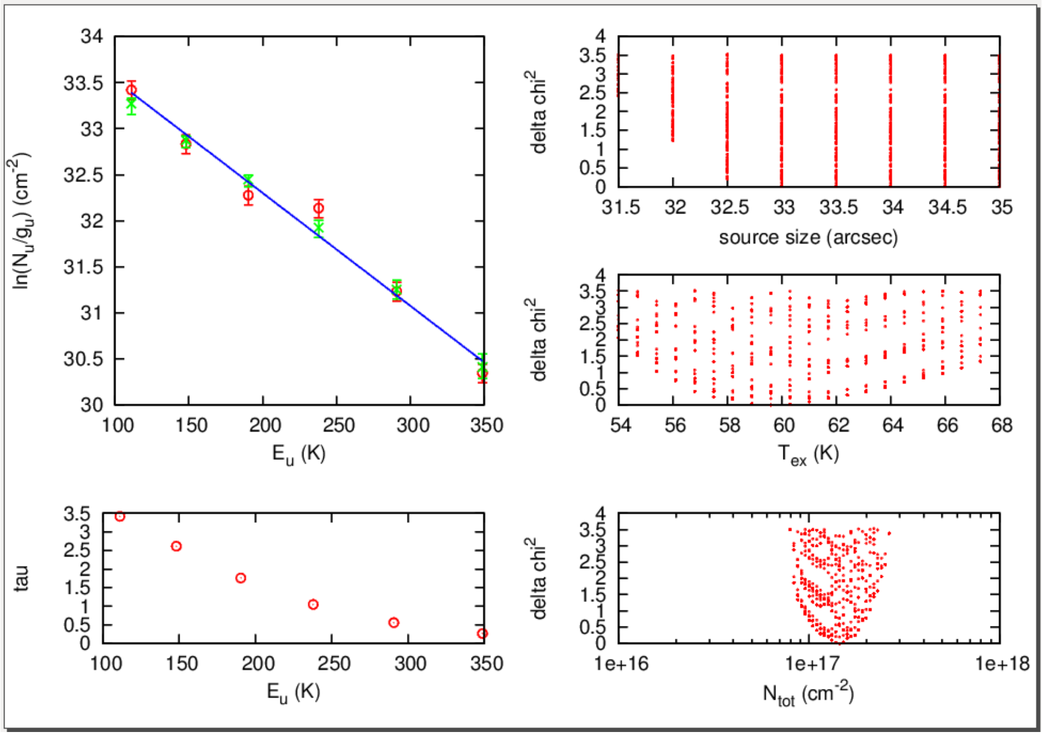

Figure 4.4: *Figure shows the population diagram of* ^{13}CO. *Plots are the same as described in Figure 4.3*

In the following we provide examples from three different species, from optically thin $C^{18}O$ to the optically thicker ^{13}CO, and also CS which is complicated by the fact that it requires two physical components to reproduce the observed emission. Figure 4.3 shows the results of the population diagram method for the (generally) optically thin $C^{18}O$ molecule. The figure on the top left shows N_u/g_u vs T (the rotation diagram). The red circles show the rotation diagram N_u/g_u data points (i.e. the values calculated via equation 4.17) and the blue line shows the rotation diagram linear fit. The green stars show the N_u^{model}/g_u values from the best fit population diagram model (i.e. from the best combination of N_t, T, and source size). The figure on the bottom left shows the value of the opacity in each transition as calculated from the best fit model. On the right we show χ^2 "surface plots" which show the value of χ^2 (or rather $\delta\chi^2$ which is given by $\delta\chi^2 = \chi^2_{step} - \chi^2_{best}$) vs the three parameters for each point in our cube: source size (top right), T (middle right), and N (bottom right).

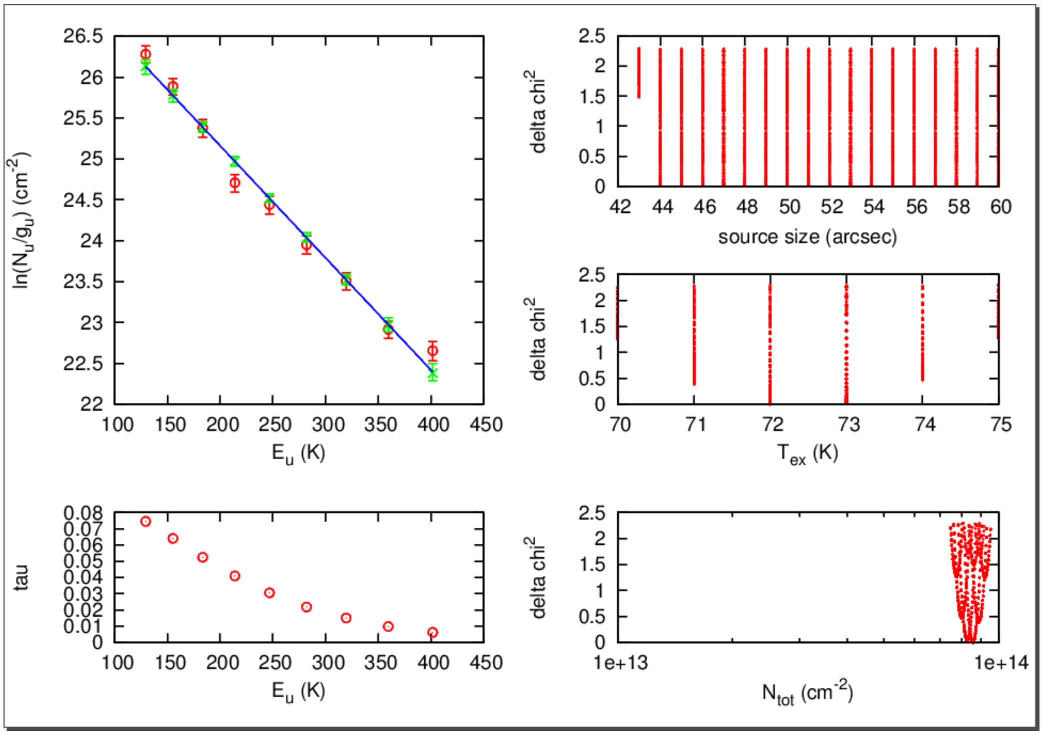

Figure 4.5: *Figure shows the population diagram of CS. Plots are the same as described in Figure 4.3.*

Figure 4.3 shows a clear convergence in N_t space at $N_t \sim 2 \times 10^{16}$, and in T space at $T \sim 62 - 63K$. There is no convergence in source size space but this figure does show that the minimum χ^2 occurs for size $> 44''$ which means that the $C^{18}O$ emission occurs from scales larger than the beam at all frequencies. The actual best fit parameters are given in Table 4.1. Given the modest opacity and large source size, it is no surprise that the population diagram results are very similar to those determined from the rotation diagram method (listed in table 4.1) since the latter technique assumes optically thin emission that fills the beam at all frequencies.

Figure 4.4 shows the results of the population diagram analysis for the more abundant isotopologue; ^{13}CO. Again there is good convergence in N_t and T space but no solution for source size. However, the minimum χ^2 values occurs for a source size > 33” indicating that the ^{13}CO emission may or may not fill the beam at all frequencies. However, with a maxi-

Table 4.1: *Population diagram results.*

Species	Pop / Rot	Source size (")	χ^2	Best value of $T(K)$	Best value of $N_t(cm^{-2})$
$C^{18}O$	Pop	40 >	1.61	62.4	2.19×10^{16}
	Rot	N/A	N/A	64	1.89×10^{16}
^{13}CO	Pop	33 >	3.42	59.6	1.45×10^{17}
	Rot	N/A	N/A	81	3.8×10^{16}
CS	Pop	45 >	6.59	73	8.12×10^{13}
	Rot	N/A	N/A	73	8.1×10^{13}

mum HIFI beam size of 39", it is likely the source can be considered extended even at the lowest frequencies. Table 4.1 also shows the best fit results for ^{13}CO. Given the large(ish) opacities and the uncertain beam size, it is no surprise that the population diagram results deviate from the rotation diagram results ($N_t = 3.8 \times 10^{16}$ and $T = 81K$; Figure 4.2).

As a final example, figure 4.5 shows the results of the population diagram analysis for CS. As we will discuss in LTE modelling section, CS line profiles are believed to be a superposition of two components, a warm compact region and a more extended region. Again the convergences of N_t and T are good but the solution for the source size is $> 45''$ which is indicating that the CS emission fills the beam at all frequencies. As figure 4.5 shows CS is optically thin, therefore it is not surprising that the population diagram and rotation diagram results matches well, see also table 4.1.

4.3 **LTE modelling**

While the population diagram method is fast and relatively straightforward, we want to test the accuracy and robustness of its results by performing a more sophisticated analysis of a few test cases and comparing the results. This method is a full LTE modelling of the actual line profiles as opposed to just the integrated intensities. To do this we use the LTE modelling capability as implemented in CASSIS.

Theoretically, in a thin case, what we receive is given by equation 4.13, where the line profile, ϕ_ν, is Gaussian and given by:

$$\phi(\nu) = \frac{1}{\sigma\sqrt{2\pi}} e^{\frac{1}{2}\left(\frac{\nu-\nu_0}{\sigma}\right)^2} \tag{4.33}$$

where σ is natural linewidth of the Gaussian line profile which can be related to the Full Width Half Maximum (FWHM) by $FWHM = 2\sqrt{2ln2}\sigma$. Therefore, in general, we know that:

$$B(T_B) = (1 - e^{-\tau})B(T_K) = \left(1 - exp\left(-\frac{c^2}{8\pi\nu^2}(e^{h\nu/kT} - 1)N_u A_{ul}\phi\right)\right)\left(\frac{2h\nu^3}{c^2}\frac{1}{e^{h\nu/kT} - 1}\right) \tag{4.34}$$

and τ, see also equation 4.32, can be modified to:

$$\tau = \frac{c^2}{8\pi\nu^2} A_{ul}(e^{E_u/kT} - 1)\frac{N_t}{\mathcal{Z}} g_u e^{-E_u/kT} \frac{1}{\sigma\sqrt{2\pi}} e^{\frac{1}{2}\left(\frac{\nu-\nu_0}{\sigma}\right)^2} \tag{4.35}$$

Equation 4.35 shows that the opacity not only changes from transition to transition but, for each transition, the opacity decreases as one steps away from the line centre (ν_0). Since the magnitude of the opacity affects the observed line brightness (equation 4.34), we can model the actual line profile by providing an N_t, T, line centre frequency (ν_0), and line width (σ), and then stepping through frequency (ν) space. At each frequency, we recalculate τ and therefore the brightness.

Since astrophysicists usually refer to Doppler velocity instead of Doppler frequency we can the change frequency dependence of equation 4.35 to V_{lsr}. Therefore, τ would have a dependence on velocity (V_{lsr}), temperature (T), total column density (N_t), & linewidth (σ). If we also take into account the beam dilution efficiency factor equation 4.34 we have five parameters dependency, N_t, T, V_{lsr}, σ, & source size $\Delta\Omega_s$.

Therefore, we have a model, $B(T_B) \equiv B^{model}_{(T_B)}(N_t, T, V_{lsr}, \sigma, \Delta\Omega_s)$, with 5 independent variables. The basic idea is similar to that employed by the population diagram method. For each of the parameters we provide a minimum and maximum value as well as a step size. We then create synthetic spectral lines at each point in a $\boldsymbol{N_t} \times \boldsymbol{T} \times \boldsymbol{V_{lsr}} \times \boldsymbol{\sigma} \times \boldsymbol{\Delta\Omega}$ grid and, using a χ^2 minimization technique, we select the combination of parameters that provides synthetic spectral lines that best match the observed spectral lines. Figure 4.6 shows an example of the spectral line fitting to the $C^{18}O$ lines. Table 4.2

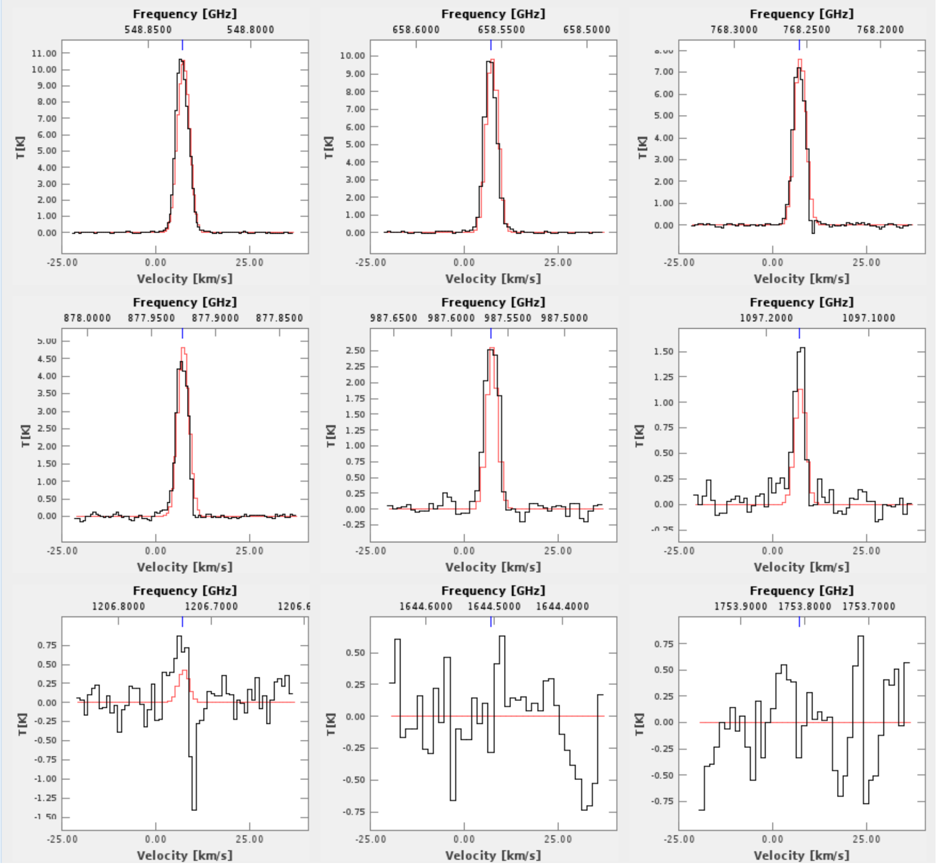

Figure 4.6: *LTE spectral line fitting of the $C^{18}O$ spectral. The black histogram shows the HIFI data and the red line shows the best model spectra.*

Although there are even more parameters to fit than in the population diagram method, and the corresponding computation time goes up dramatically, the advantage of this technique is that we are fitting the line profiles and not just the integrated intensities. Therefore, rather than having just one data point for each transition, we have as many data points per transition as we have have spectral resolution elements across the line. Thus the total number of data points for which we can compute the χ^2 is the number of transitions times the number of spectral resolution elements across each transition.

As can be seen in table 4.2, the LTE column densities for $C^{18}O$ are a factor of ~ 2 higher than those determined from the pop diagram method and, correspondingly, the temperature is about 25% lower. This discrepancy is probably due to the emission in the off position which has been discussed in chapter 3, figure 3.10. In the pop diagram analysis, we used the integrated intensities directly from the original data which, in some cases was badly contaminated by emission in the off position. However, in an attempt to improve our LTE line profile fitting, we made an attempt to crudely remove the off position emission from the raw data, which is what is presented in figure 4.6. This was accomplished by finding and co-adding the raw off position spectra, fitting out the emission feature and then using this "corrected" off position spectrum in the pipeline to produce the on-off spectra. While crude, since it uses spectral averages rather than the true time sequence on-off, it does do a decent job of removing most of the artifacts. A much more sophisticated method to correct for the off position emission is still being sorted out and, unfortunately, is beyond the scope of this thesis.

While pure χ^2 values can provide the "best fit" to the data, they cannot by themselves provide a measure of the "goodness of fit". For example, if every point in the grid has a poor χ^2 and they are all equally bad, then while the code will return the "best" fit, it is not necessarily a "good" fit nor is it particularly unique. To measure the "goodness of fit" we can also generate χ^2 surface plots. Figure 4.7 shows the surface plot for $C^{18}O$ in N_t versus T space. The x shows the best fit to the data and the contours show $\delta\chi^2 = 1, 2, 3$ (e.g. 1, 2, and 3 σ contours) going from the inner to the outer contour, where $\delta\chi^2 = \chi^2 - \chi^2_{Best}$. This plot shows that our solution is fairly well constrained in this parameter space and similar plots can be generated in the other N dimensions.

Table 4.2: *$C^{18}O$ LTE modelling best results in comparison to population diagram results.*

	N_t cm^{-1}	T_{ex} (K)	FWHM kms^{-1}	Source Size ($''$)	V_{lsr} kms^{-1}
LTE	5.17×10^{16}	48	3.5	45	7.4
Pop. diag.	2.19×10^{16}	62	N/A	40	N/A

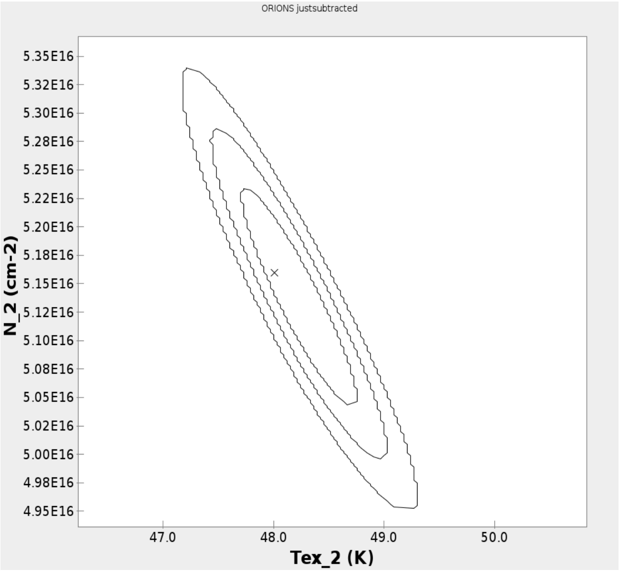

Figure 4.7: *The surface plot for $C^{18}O$ in N_t versus T space. The x shows the best fit to the data and the contours show $\delta\chi^2 = 1, 2, 3$ going from the inner to the outer contour, where $\delta\chi^2 = \chi^2 - \chi^2_{Best}$.*

LTE modelling of ^{13}CO provides us a more confident comparison with the pop diagram method since the ^{13}CO spectra did not suffer as much contamination with the off position emission. Therefore our result does not rely on our crude attempt to correct for the contamination. A comparison of these two results is listed in table 4.3. Also figure 4.8 shows the LTE model spectra superimposed upon the HIFI ^{13}CO spectra. The χ^2 contour diagram for N_t versus T is shown in figure 4.9 to provide a level of confidence in the results. Table 4.3 shows that there is a fairly good match between the results of N_t and T from population diagram and LTE modelling.

Table 4.3: ^{13}*CO LTE modelling best results in comparison to population diagram results.*

	$N_t\ cm^{-1}$	$T_{ex}\ (K)$	FWHM kms^{-1}	Source Size ($''$)	$V_{lsr}\ kms^{-1}$
LTE	1.66×10^{17}	66	3.5	96	7.5
Pop. diag.	1.45×10^{17}	60	N/A	$33 >$	N/A

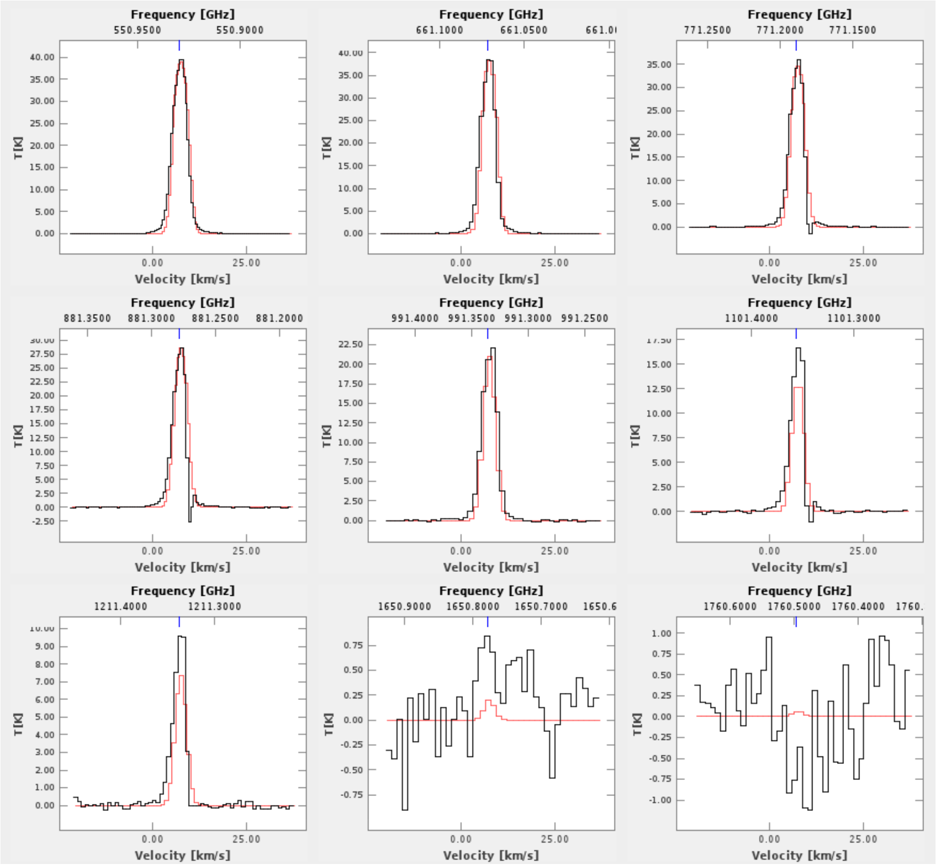

Figure 4.8: *HIFI* ^{13}*CO spectra. The black histogram shows the data and the red lines show the best fit LTE model.*

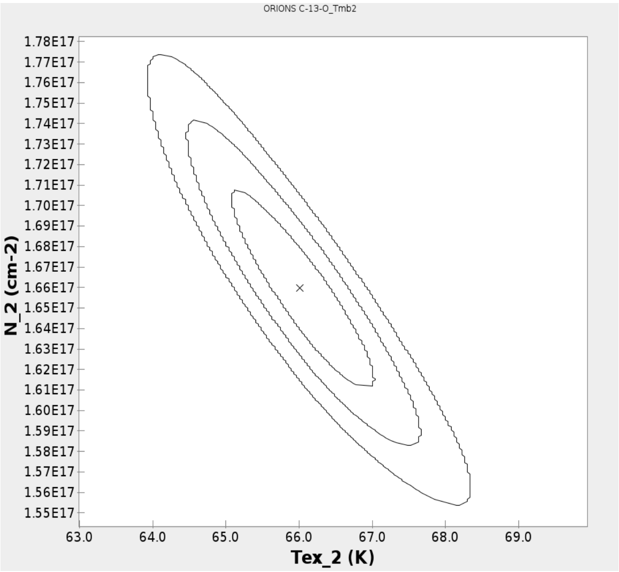

Figure 4.9: *The surface plot for* ^{13}CO *in* N_t *versus* T *space. The x shows the best fit to the data and the contours show* $\delta\chi^2 = 1,\ 2,\ 3$ *going from the inner to the outer contour, where* $\delta\chi^2 = \chi^2 - \chi^2_{Best}$.

We now turn our attention to CS and attempt the same modelling procedure. The results of which are shown in figure 4.10. It can immediately be seen from this figure that our "best fit" is not actually a good fit to the data and that the discrepancy between data and model worsens at higher J. This likely indicates that a one component model is insufficient to the task and that we need to invoke a two component model to fit the data: one which is warm (to account for the high J emission) and one which is cool (to account for the low J emission).

In a two component case, such as CS, we are dealing with a 10 dimensional parameter space. This makes the situation more complicated and time consuming. However, given the fact that we have 9 transitions of CS and good spectral resolution across them, the problem is still tractable. In fact, we can decrease the number of free parameters by first estimating a source size for each component and allowing the other 4 parameters to float. From this first pass we can obtain fairly accurate values for the best fit V_{lsr} and FWHM of both components.

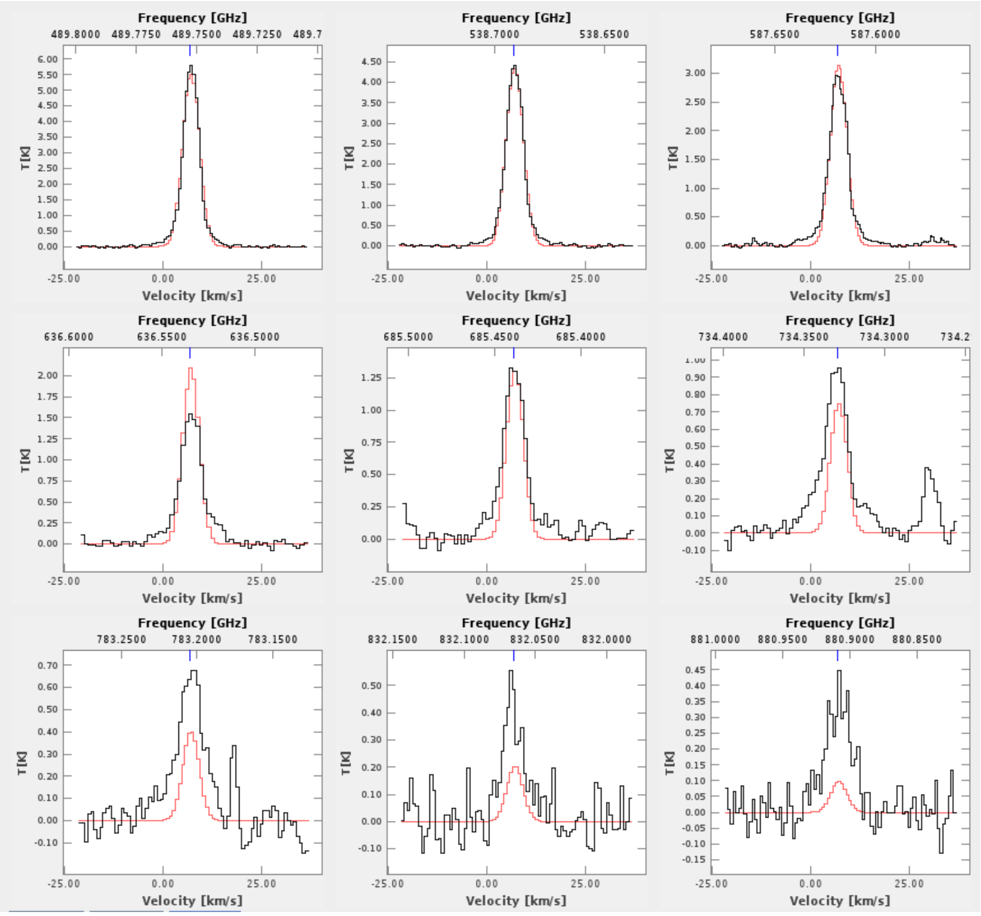

Figure 4.10: *1 component LTE spectral line fitting to the CS spectral. The black histogram shows the HIFI data and the red line shows the best model spectra.*

Then, in a second iteration, we fix the width and velocity of each component and allow the column density, temperature, and size of each component to vary. This iterative technique cuts the number of free parameters from 10 to 6 which greatly speeds up the computation time and makes the problem tractable. In figure 4.11 we show our best two components fit to the CS spectra. In figure 4.12 we show the χ^2 contour diagrams to show the “goodness of fit”. The “best fit” model is provided in table 4.4

As table 4.4 shows, the two component fitting of CS results in a small (19”), warm (84 K) core surrounded by a more extended (39”), cooler (31 K) envelope. This is not surprising since the warm core-cool envelope model is expected in a core with embedded star forma-

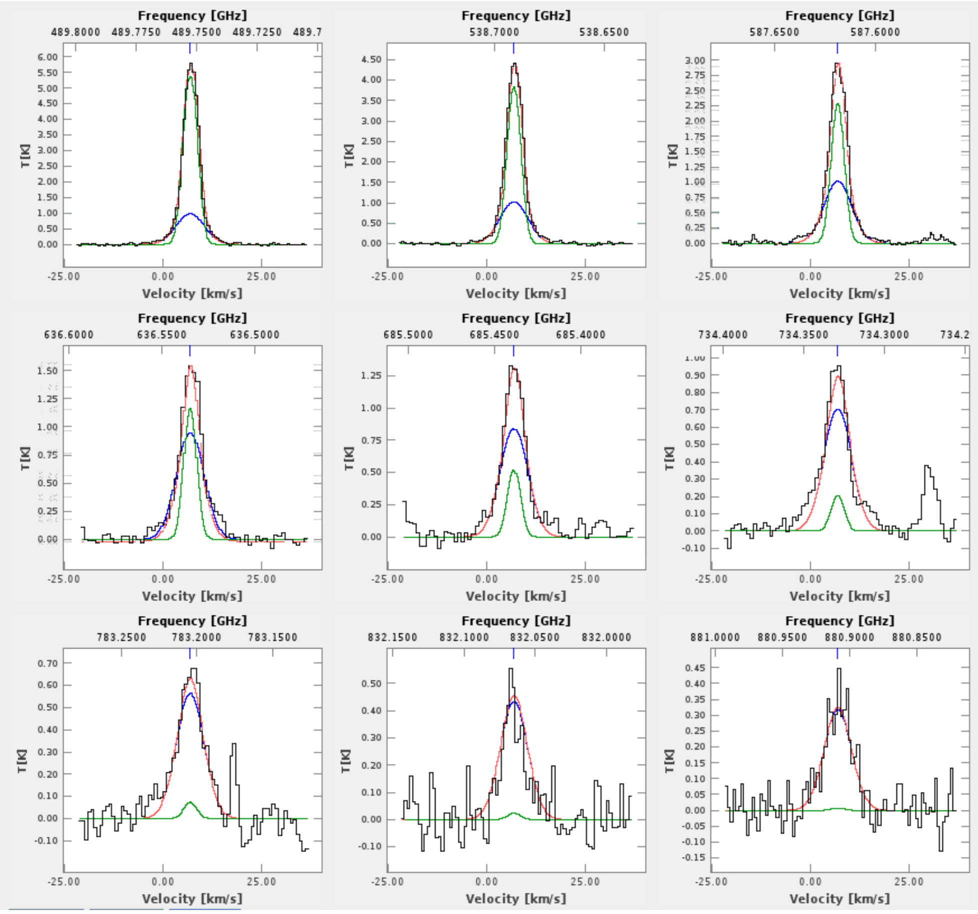

Figure 4.11: *2 components LTE spectral line fitting to the CS spectra. The black histogram shows the data and the red lines show the best fit LTE model which incorporates emission form both a warm, shown in blue lines, and a cooler extended component, shown in green.*

tion and has been seen on numerous occasions (i.e. Andre et al. 2010, Gutermuth et al. 2009, Linz et al. 2010). However, it is satisfying that our modelling technique provided this solution without any a priori assumptions about the core structure. Comparing the results with the population diagram method it seems that population diagram method for CS preferentially traces the warm compact component although it underestimates both the column density and the temperature of this component.

Our two component CS results does not only provide a better understanding of the source structure but also it can improve our modelling for ^{13}CO. Careful examination of figure 4.8 shows that, while the one component model matches the data extremely well at

Table 4.4: *CS LTE modelling best results of two components modelling.*

	N_t cm^{-1}	T_{ex} (K)	FWHM kms^{-1}	Source Size ($''$)	V_{lsr} kms^{-1}
LTE Compact	1.9×10^{14}	84	8.2	19	7.0
LTE Extended	1.3×10^{15}	31	3.8	39	7.2
Pop 1 component	8.12×10^{13}	73		45	

low J, at higher J there is a definite deviation between the models and the data. However, if we add a 20", 85K warm component (as derived from the CS results) to the original one component fit for ^{13}CO, we improve the fit for the high J transitions without degrading the fit to the low J transitions (see Figure 4.13). The parameters for the two component ^{13}CO fit are given in Table 4.5.

Table 4.5: *Two components result for* ^{13}CO.

	N_t cm^{-1}	T_{ex} (K)	FWHM kms^{-1}	Source Size ($''$)	V_{lsr} kms^{-1}
First extended component	1.66×10^{17}	66	3.5	96	7.5
Second hot component	5×10^{16}	85	6.5	20	7.4

As an additional tests of the robustness of the population diagram method we did LTE modelling for some other species. These results are listed in table 4.6.

What we can see from Table 1.6 is that for ^{13}CO, $H^{13}CO^{+}$, and $H^{13}CN$ there is very good agreement between the column densities and excitation temperatures derived from the population diagram method versus the full LTE spectral line profile modelling method. The source size agreement is less certain, but the sources sizes are not well constrained since, in most cases, they are larger than the beam at all frequencies.

For $C^{18}O$, CS, HCO^{+}, and HNC the agreement is less good. For $C^{18}O$ the column density and excitation temperature are off by a factor of 2 and 25% respectively. However,

Table 4.6: *Comparing LTE results with the population diagram results.*

Species	LTE / Pop	components	N_t cm^{-1}	T_{ex} (K)	FWHM kms^{-1}	Source Size $('')$	V_{lsr} kms^{-1}	comments
^{13}CO	LTE		1.66×10^{17}	66	3.5	96	7.5	
	Pop		1.45×10^{17}	60		33 >		
$C^{18}O$	LTE		5.17×10^{16}	48	3.5	45	7.4	
	Pop		2.19×10^{16}	62		40 >		E.O.P contamination
CS	LTE	warm	1.9×10^{14}	84	8.2	19	7.0	
	LTE	cold	1.3×10^{15}	31	3.8	39	7.2	
	Pop		8.12×10^{13}	73		45 >		
$H^{13}CO^+$	LTE		3.74×10^{12}	40	3.7	109	7.1	
	Pop		2.95×10^{12}	44		42 >		
HCO^+	LTE	warm	2.87×10^{13}	98	5.4	20	7.0	
	LTE	cold	6.70×10^{13}	54	4.7	119	7.2	
	Pop		4.68×10^{13}	77		41 >		1 component
HNC	LTE		1.87×10^{13}	25	4.5	120 >	7.5	
	Pop		8.32×10^{12}	33		40 >		Only 3 transitions
$H^{13}CN$	LTE		2.70×10^{12}	42	5.5	120 >	7.5	
	Pop		1.69×10^{12}	44		42 >		Only 3 transitions

* E.O.P: Emission in the Off Position.

as we have already mentioned, this is likely due to the contamination from the off-position emission. Given this, the agreement is remarkably good. For CS there is a clear need to model this species using two physical components. The population diagram method in this case seems to preferentially trace the warm component and does so to within a factor of two in column and 20% in temperature. For HCO^+, although the LTE modelling again requires two physical components to model the line profiles, the single component population diagram method finds a solution between the warm and cold components, again within a factor of two column density and 30% for temperature. Finally, for HNC, the column density is again off by a factor of ~ 2 and the temperature by $\sim 30\%$. However, the HNC population diagram was constructed from only 3 transitions and so its results could not be considered terribly robust. Nevertheless, the agreement in spite of this is remarkable.

Thus, it seems that the population diagram method is a useful tool to quickly obtain the physical conditions to within a factor of two in column density and $\sim 30\%$ in excitation temperature. This is true even in some of the most extreme cases, such as when the data are contaminated by emission in the off position, or when the line profiles clearly need to be modelled by two components, or when there are only 3 transitions. In less extreme cases, the agreement is better than 10%. Thus, we feel that we can use the population diagram method to extract this physical information from the remainder of the species detected in Orion-S to reasonable confidence. Since the population diagram routine runs in minutes versus hours or tens of hours (for the two component models), this represents a considerable savings in computational time.

4.4 Population Diagram Results for Other Species

Given the good match between the pop diagram and LTE modelling results shown in the previous chapter, we can can now confidently provide the column densities, excitation temperatures, and source sizes for the remaining species detected in Orion S using the pop diagram method. Results are shown in tables 4.7 and figures 4.14 to 4.37. Since the population diagram result is providing us with a range of solution for the source size we listed this solution range with the best χ^2 listed in between, (i.e $22 < 41 < 61$ means 41" is the minimum of the χ^2.

In order to be able to sensibly utilize a population diagram we should observe at least four transitions since there are four variables in eq.4.26, τ, N_t, T, & $\Delta\Omega_s$. In order to get results for three transitions we need to fix at least one of the free parameters. In most cases, we assume the source size, Ω_s, to be known mostly based on Zapata et al. work (2004). So in table 4.7 the results are reported by assuming source size varies between $10'' - 60''$ also to get a better solution convergence we fixed the source size to some values, $10''$, $30''$, $40''$.

Although it was only necessary for those species that we observe three transitions, we did it for all species to have a better understanding of the results and minimize χ^2.

These results will be used in a future study (summer 2013) to provide the first ever, comprehensive comparison of the chemical abundances in both Orion-KL and Orion South. This comparison will provide insight into the physical and chemical differences between two regions of massive star formation that are at different stages in their evolution.

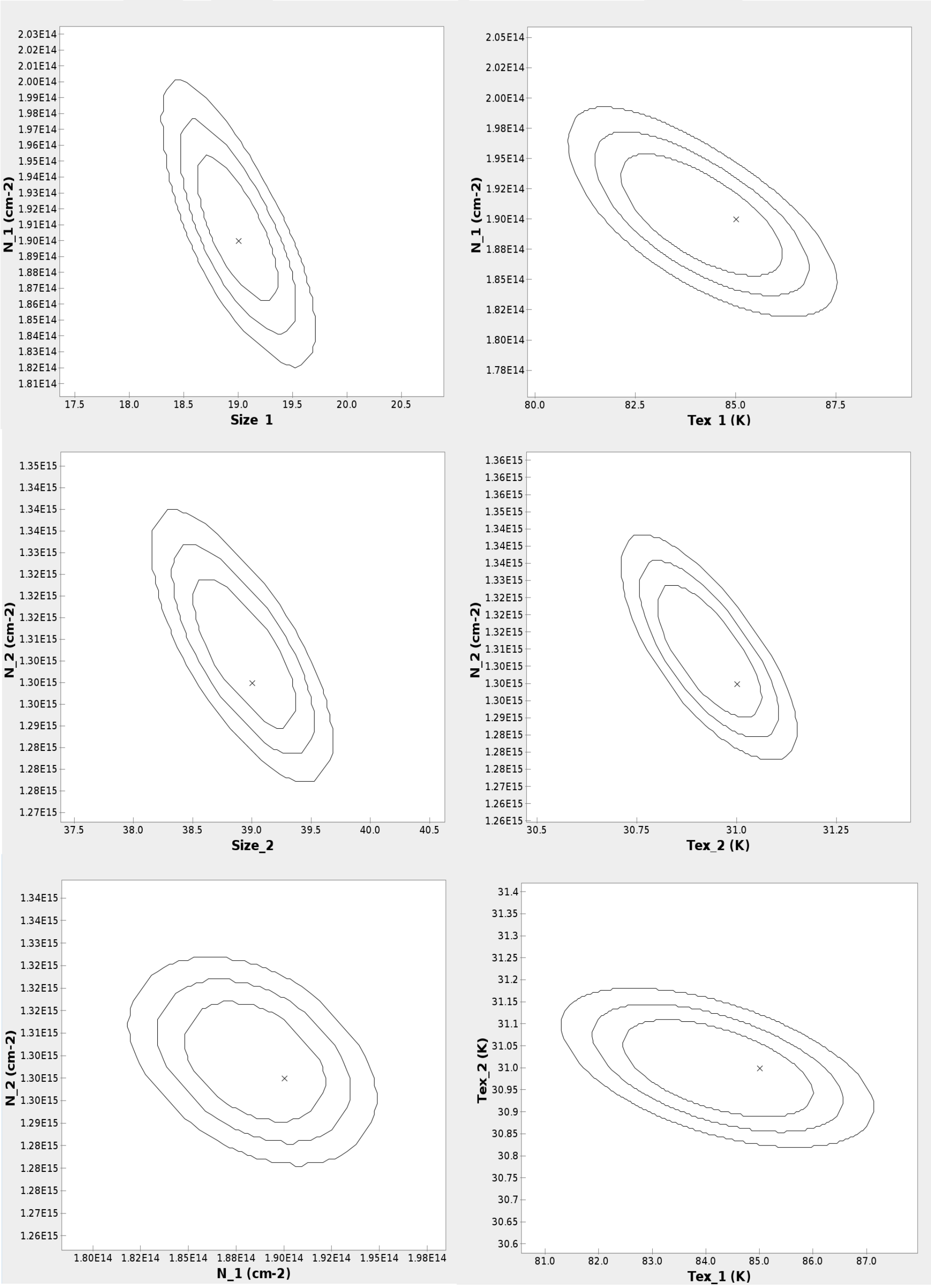

Figure 4.12: *The surface plots for two component model of* CS *in different variables space. The x shows the best fit to the data and the contours show* $\delta\chi^2 = 1$, 2, 3 *going from the inner to the outer contour, where* $\delta\chi^2 = \chi^2 - \chi^2_{Best}$. *Subscript 1 and 2 stand for respectively warm compact and cold extended region.*

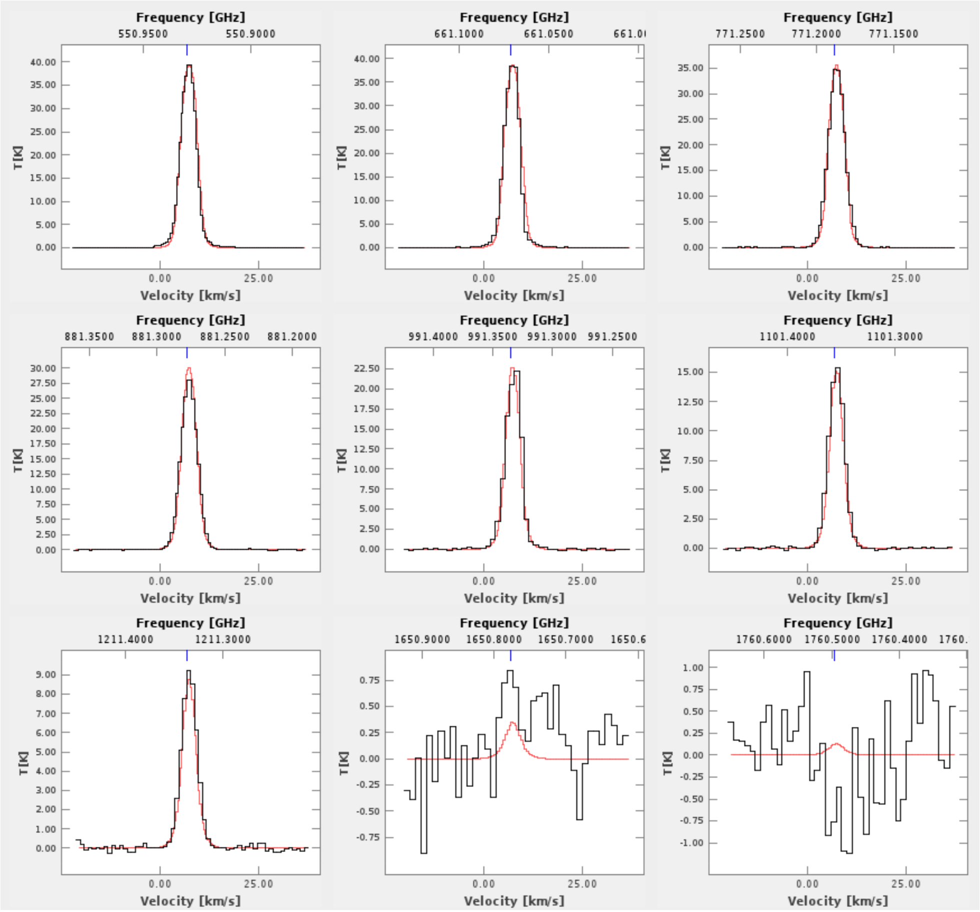

Figure 4.13: *HIFI ^{13}CO spectra. The black histogram shows the data and the red lines show the best fit LTE model which incorporates emission from both a warm and a cooler extended component.*

Table 4.7: *Population diagram results.*

Species	Source size (Arcsec)	Best source size range (Arcsec)	χ^2	Best value of $T(K)$	Best value of $N_t(cm^{-2})$
CCH	10-60	$22 < 41 < 60$	0.84	38.0	1.91×10^{14}
CN	10-60	$37 < 39 < 60$	4.25	36.0	3.24×10^{13}
^{13}CO	10-60	$31.5 < 33 < 35$	3.42	59.6	1.45×10^{17}
$C^{17}O$	10-60	$29 < 31 < 32$	224.32	39.0	8.71×10^{17}
$C^{18}O$	10-60	$35 < 40 < 60$	1.61	62.4	2.19×10^{16}
CO_{comp1}	10-60	$36 < 37.5 < 60$	3.54	92.0	4.27×10^{18}
CO_{comp2}	10-60	$35 < 37.5 < 40$	3.04	223.6	1.10×10^{17}
$C^{34}S$	10-60	$43 < 45 < 60$	12.97	70.5	6.92×10^{12}
CS_{comp1}	10-60	$40 < 41 < 60$	25.83	84.8	4.07×10^{13}
CS_{comp2}	10-60	$28.8 < 29.4 < 30.6$	17.03	80.5	3.55×10^{13}
H_2CS	10-60	$43 < 45 < 60$	16.18	82.0	1.55×10^{13}
$H^{13}CN!$	10-60	$10 < 42 < 60$	1.15	71.3	6.46×10^{11}
	10		1.97	42.1	1.74×10^{13}
	30		1.89	44.2	1.69×10^{12}
	40		1.10	73.2	6.31×10^{11}
$H^{13}CO^+$	10-60	$25 < 42 < 60$	3.27	44.2	2.95×10^{12}
HCO^+	10-60	$39 < 41 < 60$	2.33	76.9	4.68×10^{13}
$HNC!$	10-60	$23 < 40 < 60$	3.89	33.8	8.32×10^{12}
	10		25.28	26.6	2.29×10^{14}
	30		5.60	25.5	2.84×10^{13}
	40		3.80	33.5	8.32×10^{12}
$o-H_2CO$	10-60	$44 < 44 < 60$	31.53	120.9	2.45×10^{13}
$p-H_2CO$	10-60	$42 < 43 < 60$	44.10	158.4	3.72×10^{13}
H_2S	10-60	$28.88 < 29.28 < 30.64$	19.56	14.0	2.09×10^{16}
$o-H_2S!$	10-60	$29 < 43 < 60$	30.31	15.0	9.77×10^{14}
	10		212.81	30.7	5.75×10^{16}
	30		30.57	15.0	2.67×10^{15}
	40		30.63	15.2	1.00×10^{15}
$p-H_2S!$	10-60	$31 < 32 < 60$	2.34	13.0	4.07×10^{16}
	10		100.91	25.8	3.86×10^{15}
	30		3.04	13.0	3.98×10^{16}
	40		2.36	13.1	3.89×10^{16}
SO	10-60	$4.3 < 4.3 < 4.3$	6.84	56.5	2.29×10^{16}
SO_2	10-60	$44 < 45 < 60$	6.88	138.0	1.95×10^{14}

(!) after the species names means we see only three transitions.
If the best source size range ends in 60 it means it is uncertain.

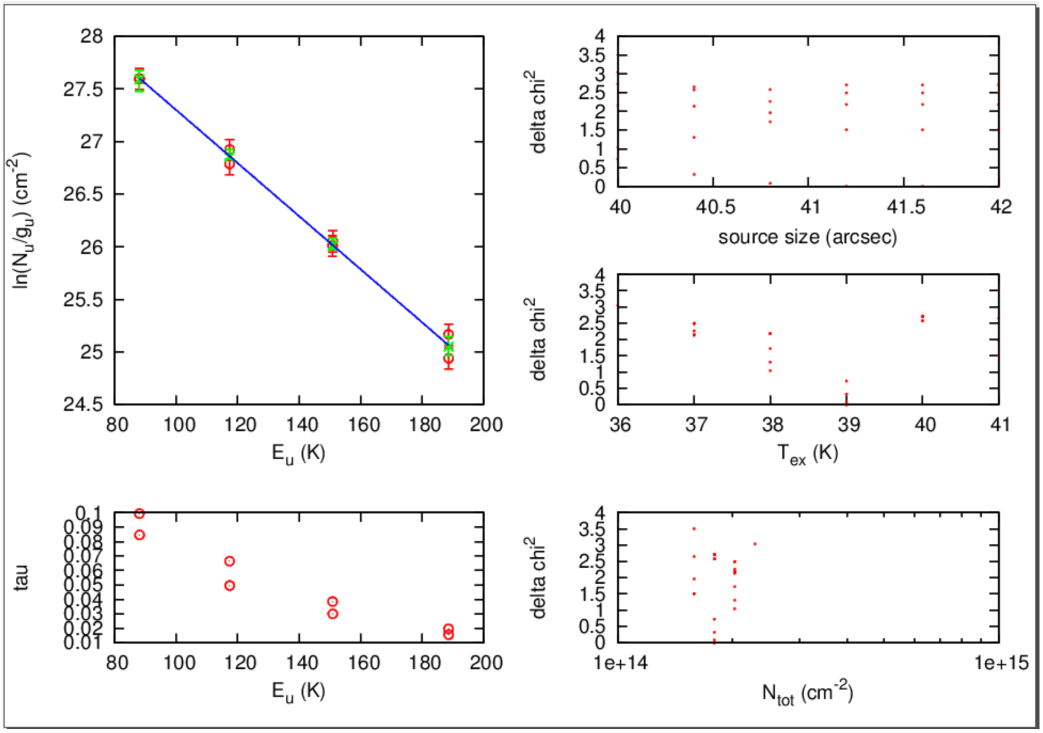

Figure 4.14: *CCH population diagram.*

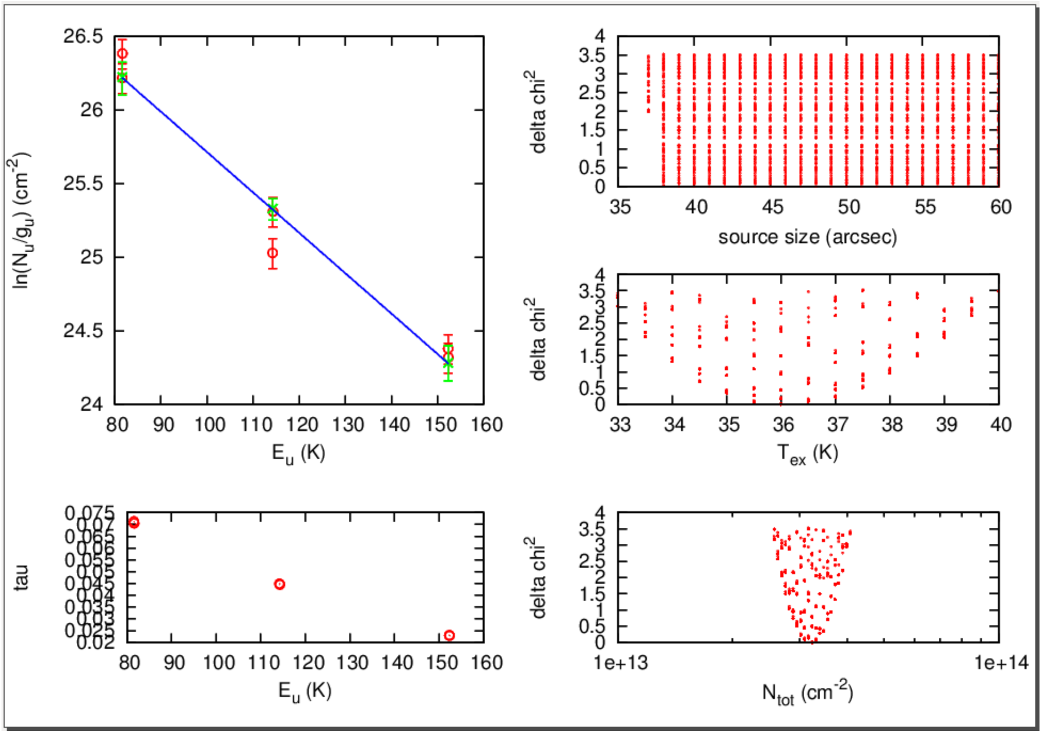

Figure 4.15: *CN population diagram.*

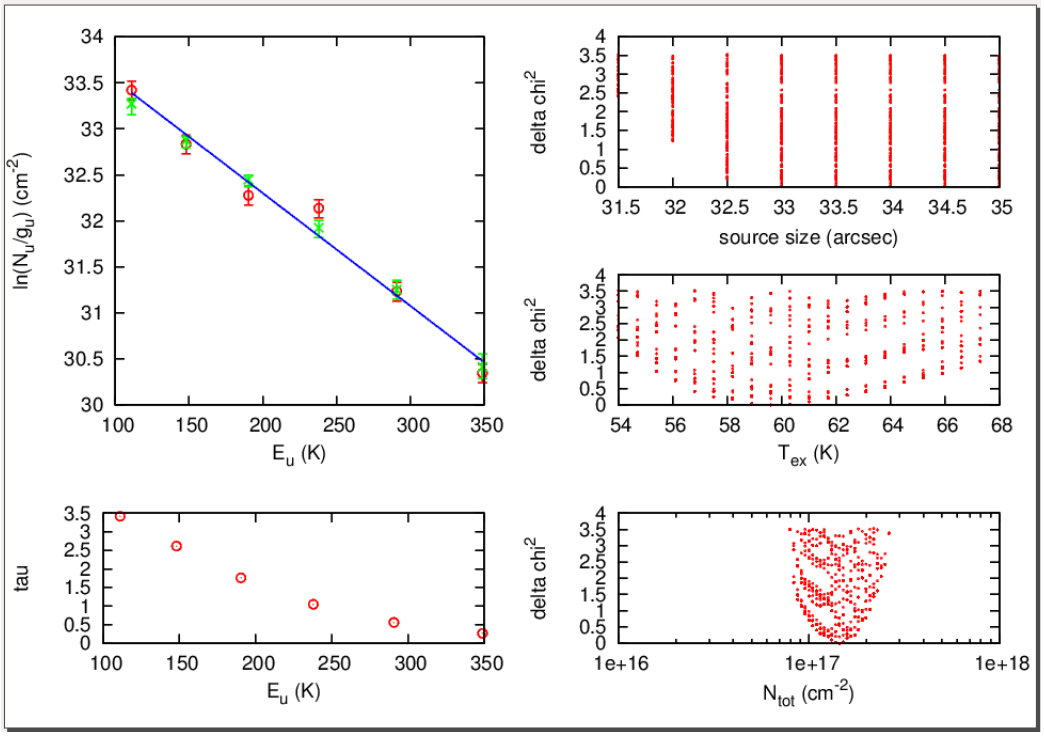

Figure 4.16: ^{13}*CO population diagram.*

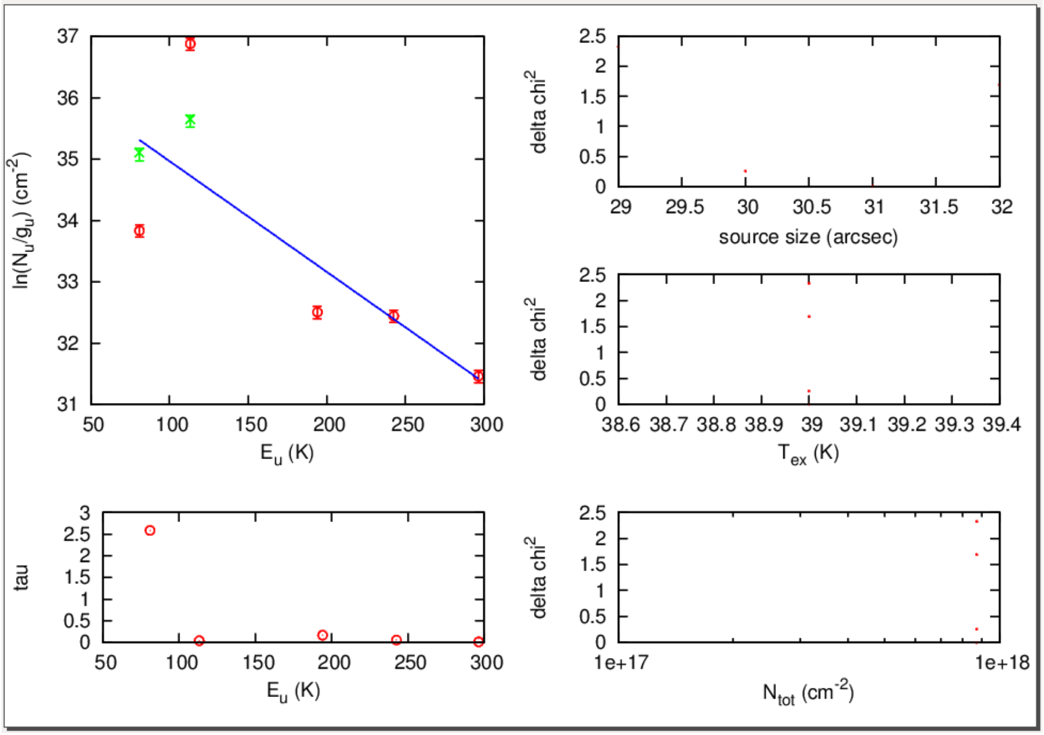

Figure 4.17: *$C^{17}O$ population diagram.*

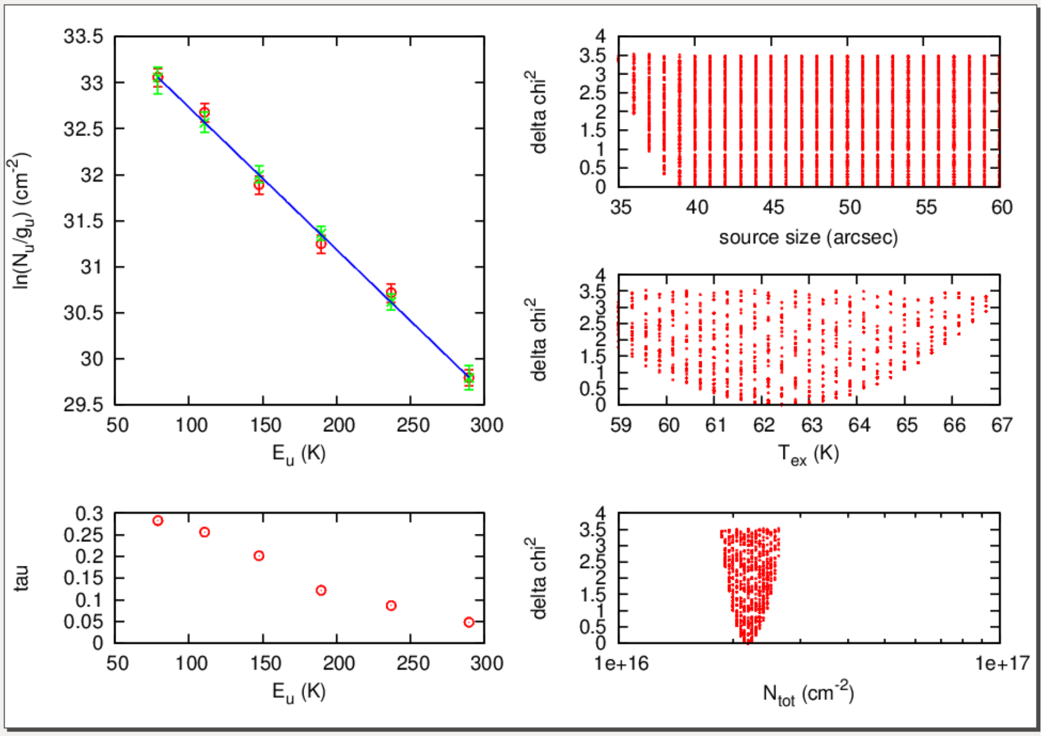

Figure 4.18: *$C^{18}O$ population diagram.*

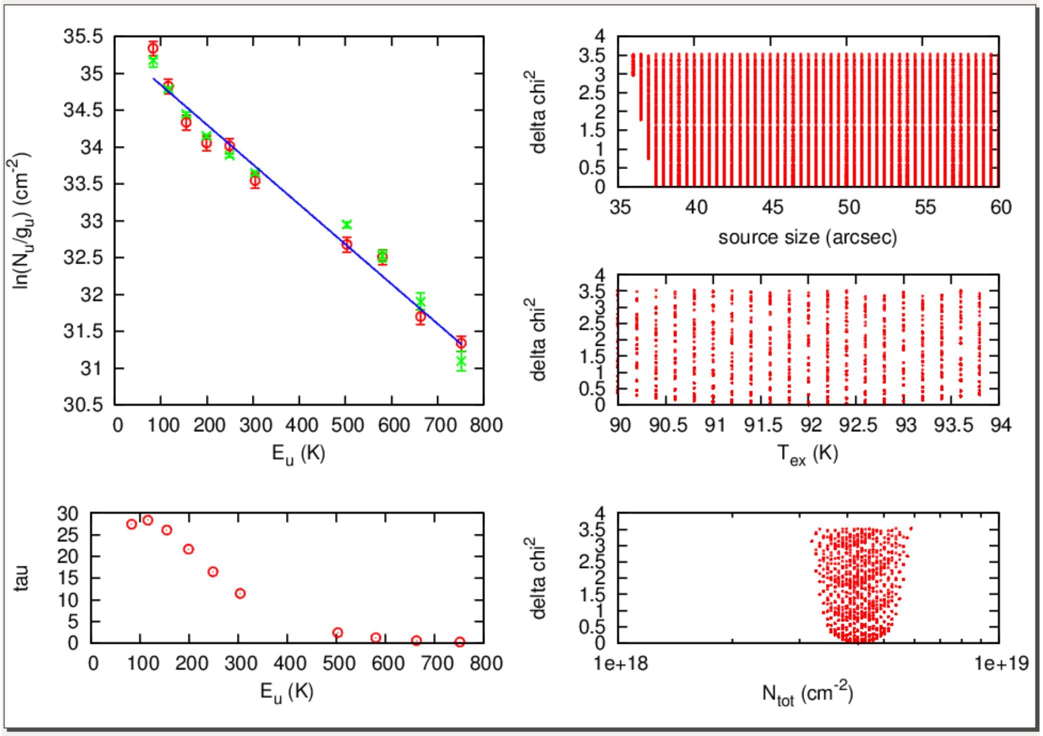

Figure 4.19: *CO population diagram of the more extended region and outflow.*

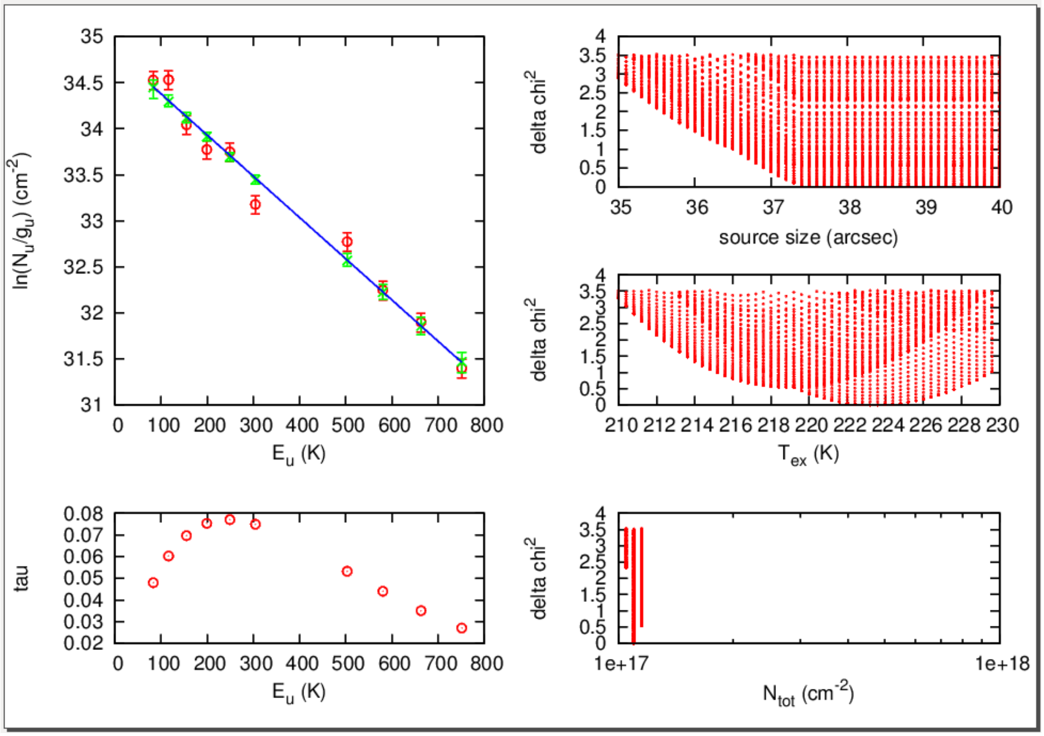

Figure 4.20: *$C^{18}O$ population diagram of the hot core.*

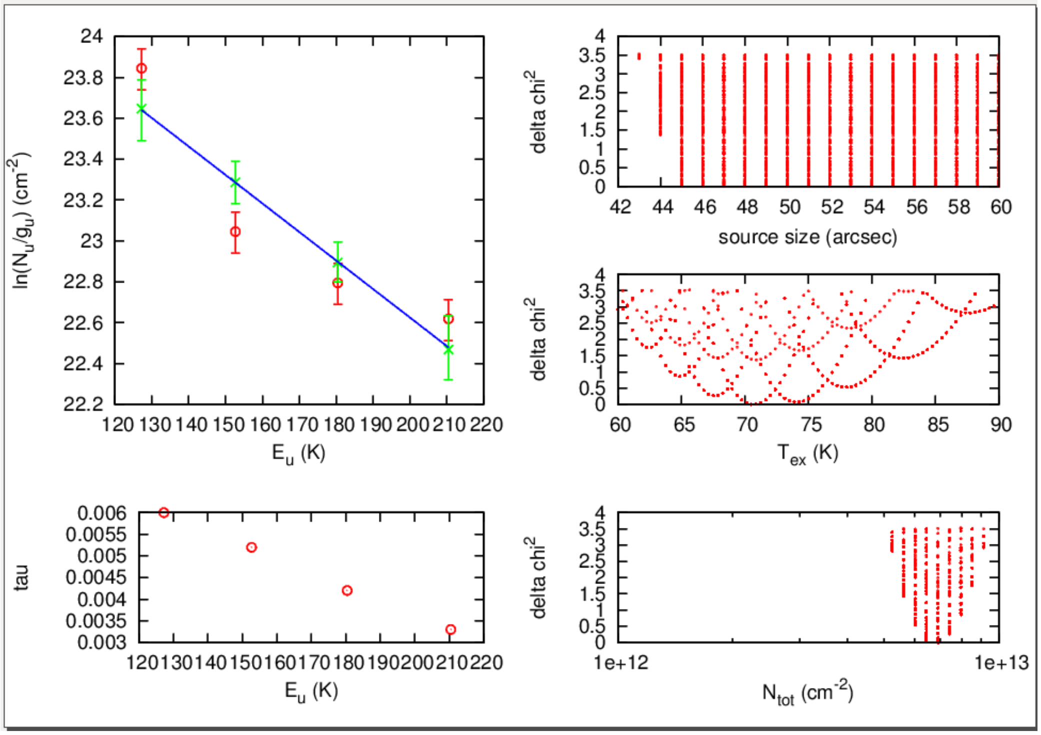

Figure 4.21: *$C^{34}S$ population diagram.*

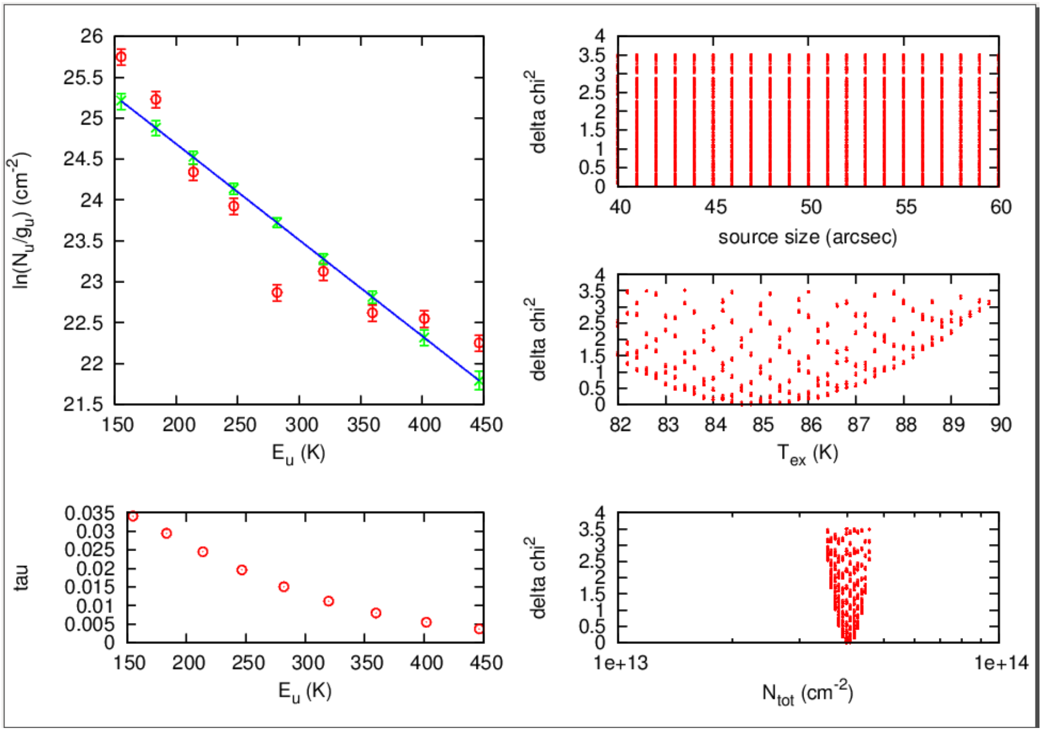

Figure 4.22: *CS population diagram of the more extended region.*

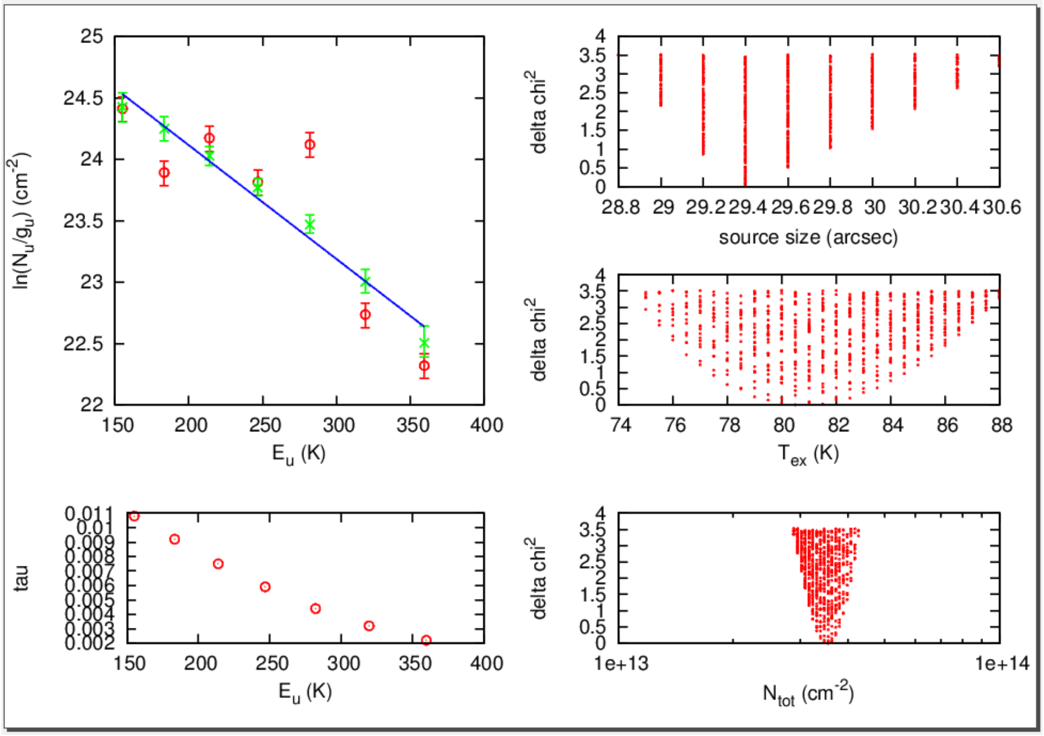

Figure 4.23: *CS population diagram of the hot core.*

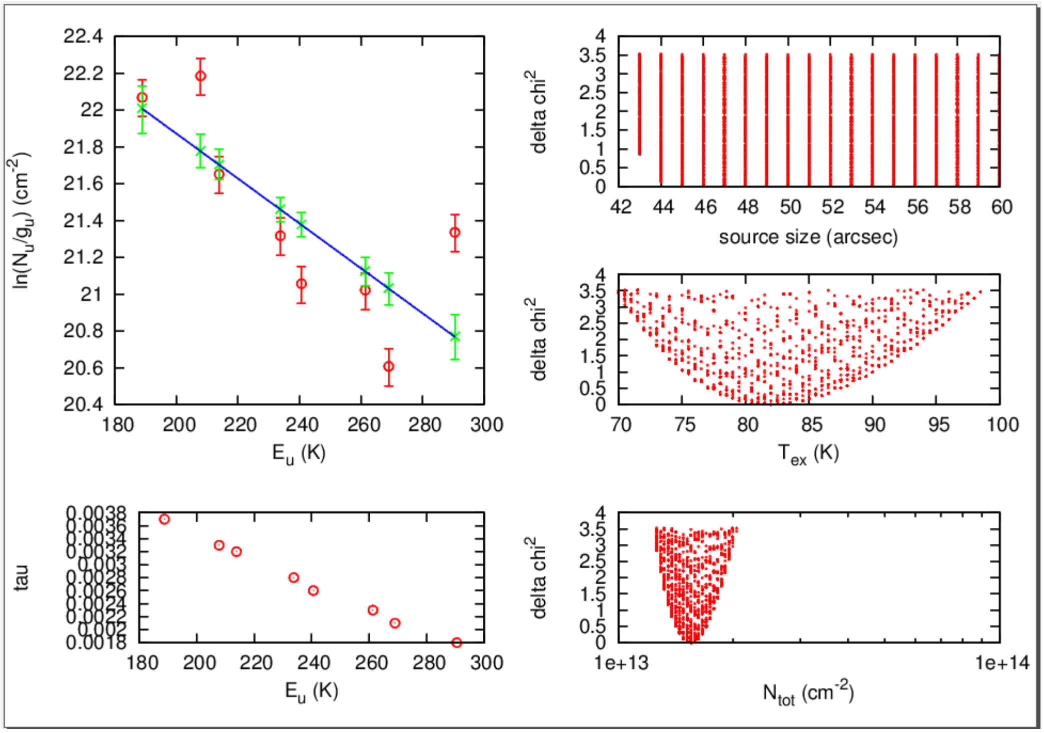

Figure 4.24: *H_2CS population diagram.*

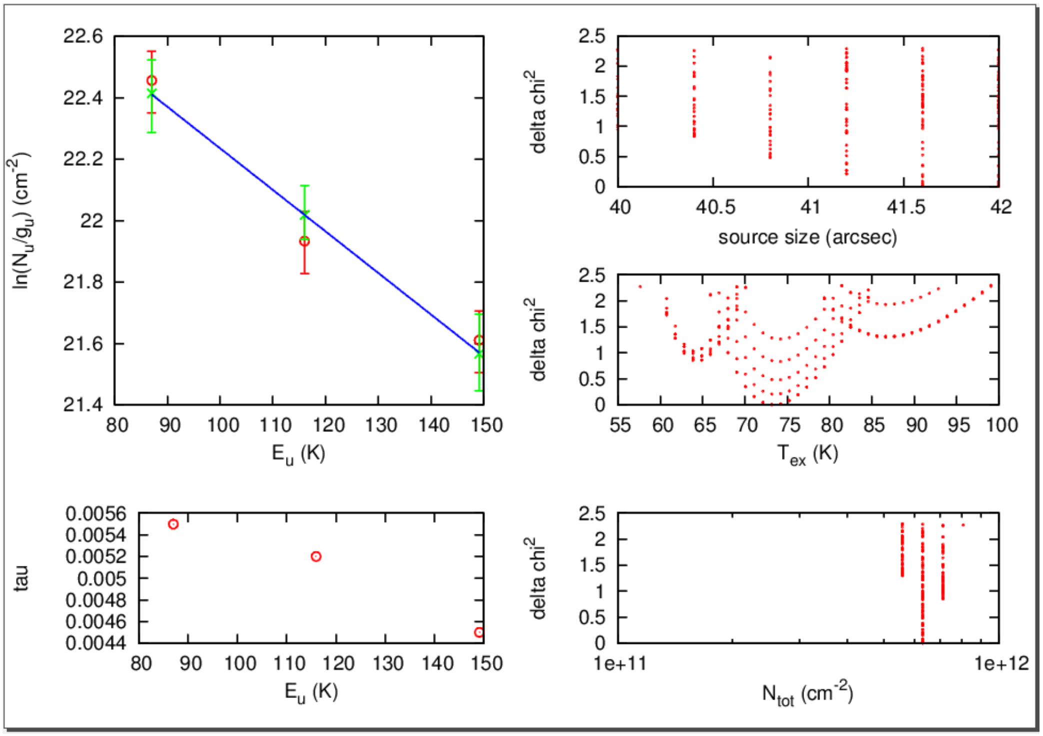

Figure 4.25: *$H^{13}CN$ population diagram at the fixed source size of* $41''$.

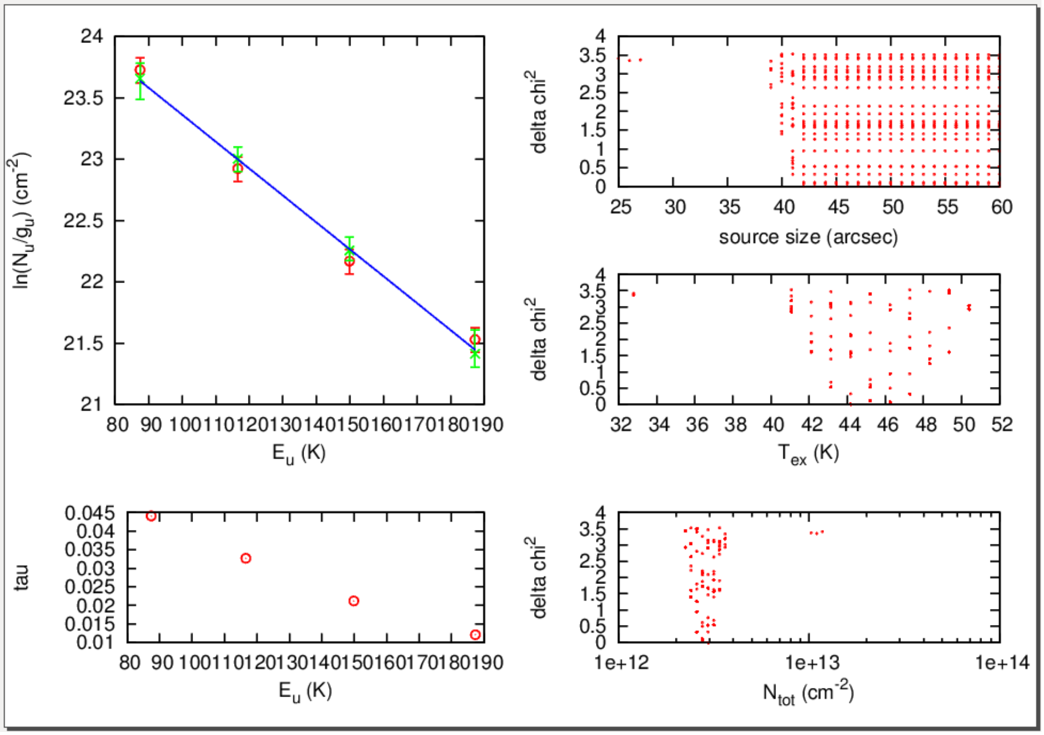

Figure 4.26: *$H^{13}CO^{+}$ population diagram.*

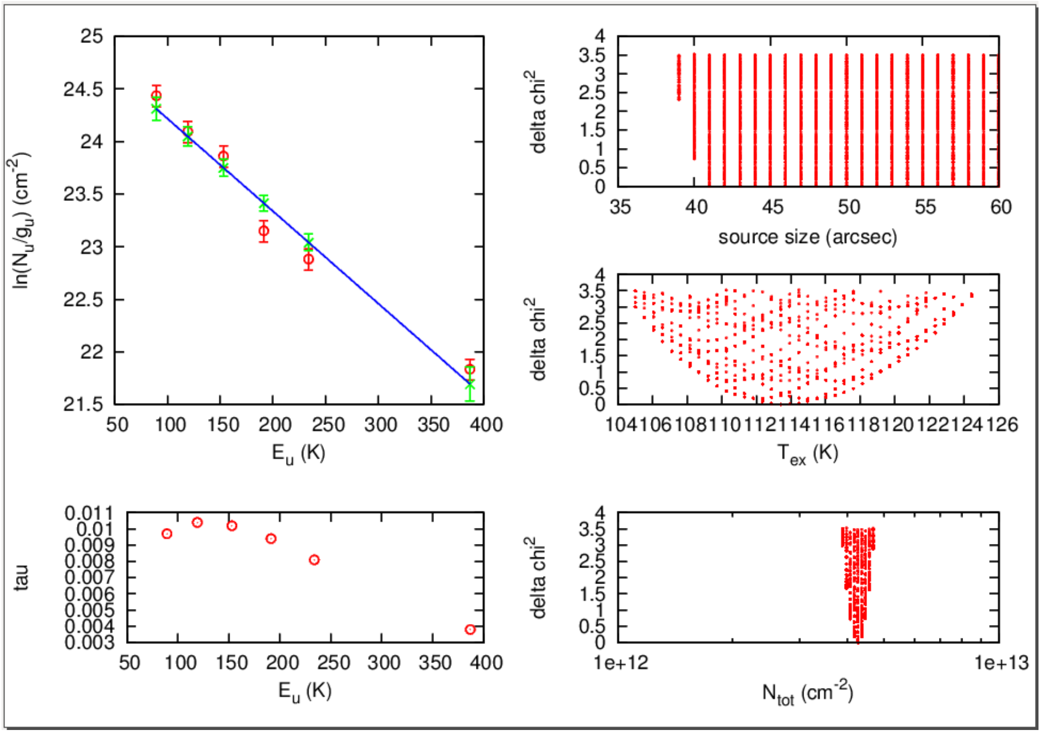

Figure 4.27: *HCN population diagram of the more extended region.*

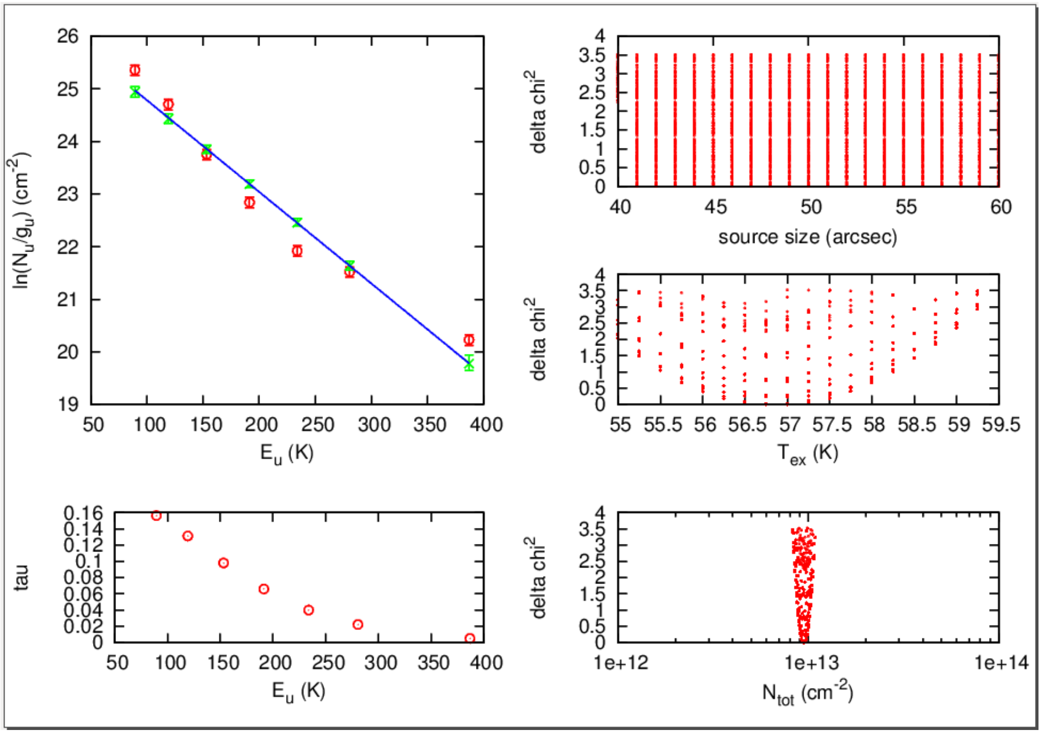

Figure 4.28: *HCN population diagram of the hot core.*

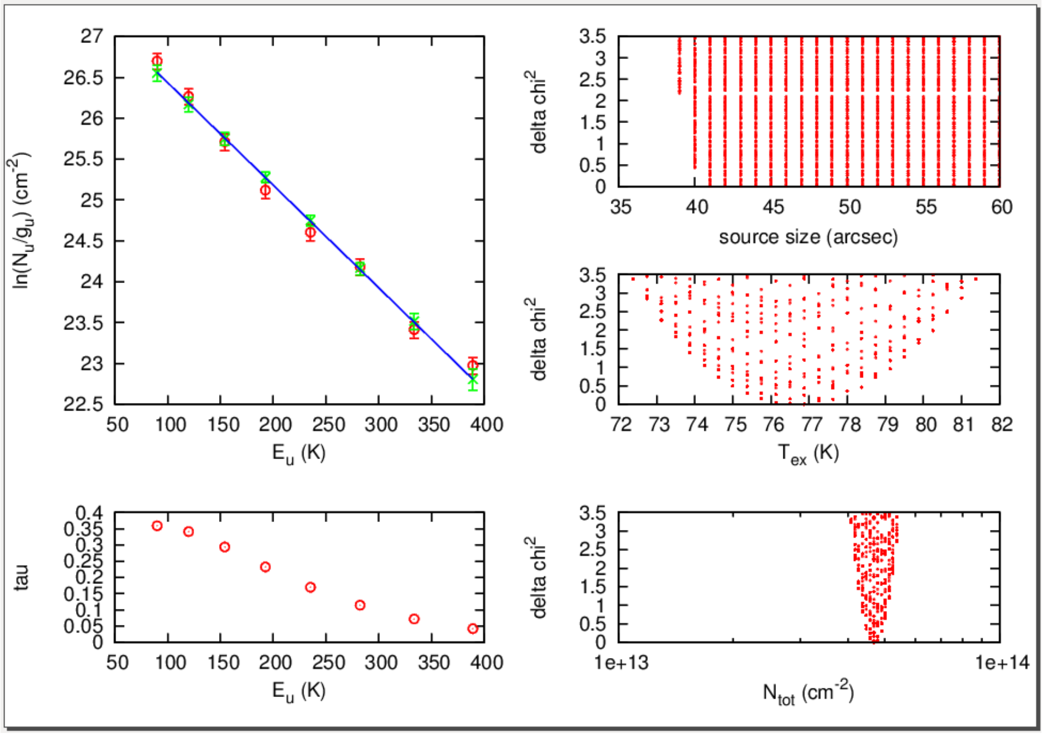

Figure 4.29: *HCO^+ population diagram.*

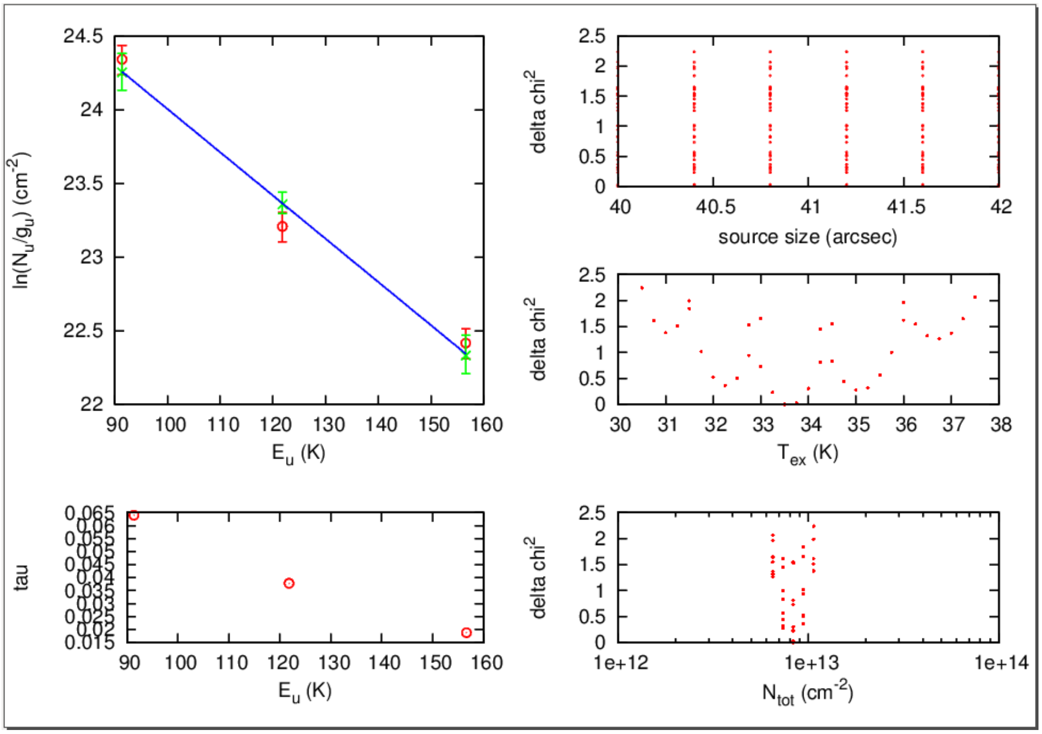

Figure 4.30: *HNC population diagram with the fixed source size of* $41''$.

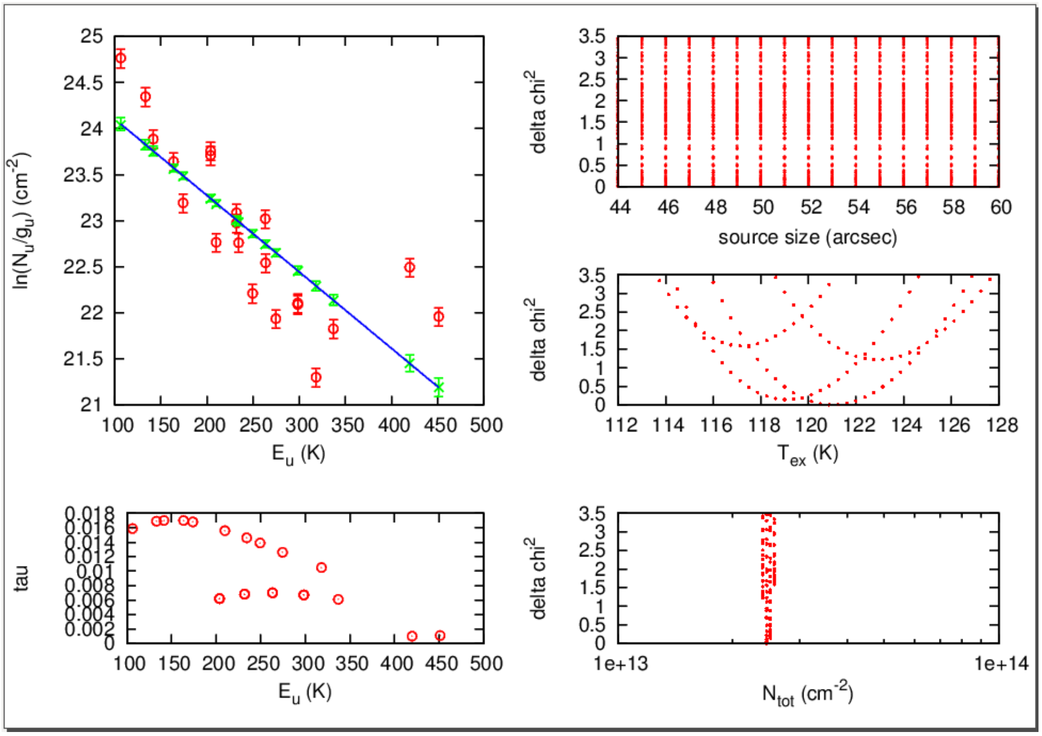

Figure 4.31: $o - H_2CO$ *population diagram.*

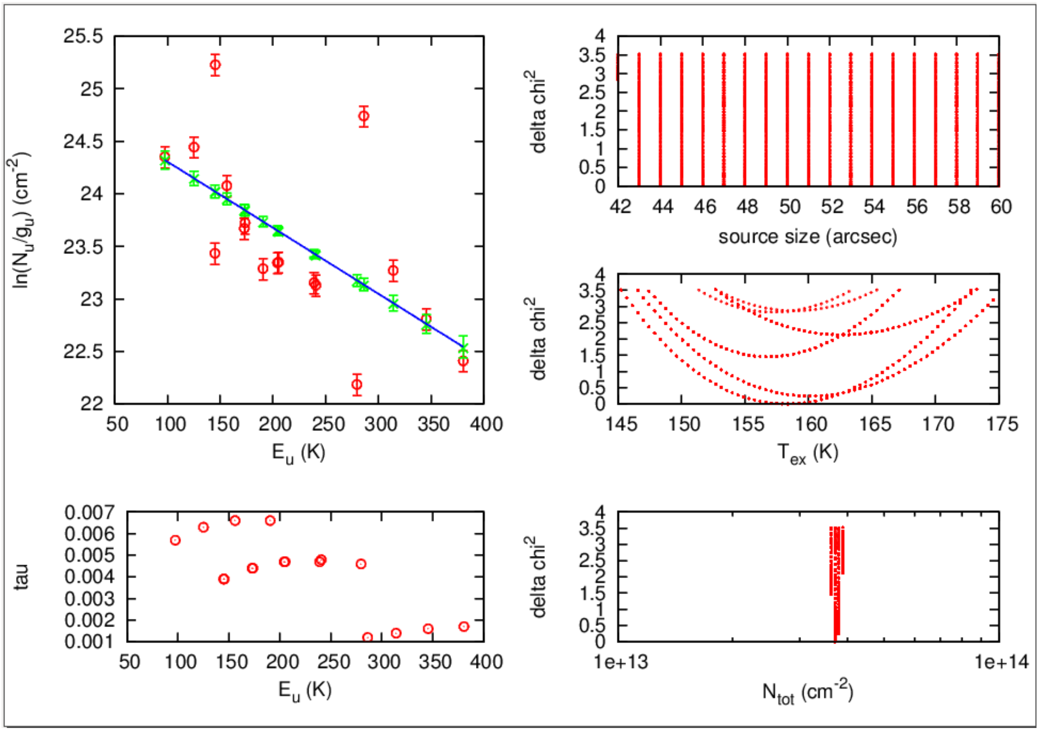

Figure 4.32: $p - H_2CO$ *population diagram.*

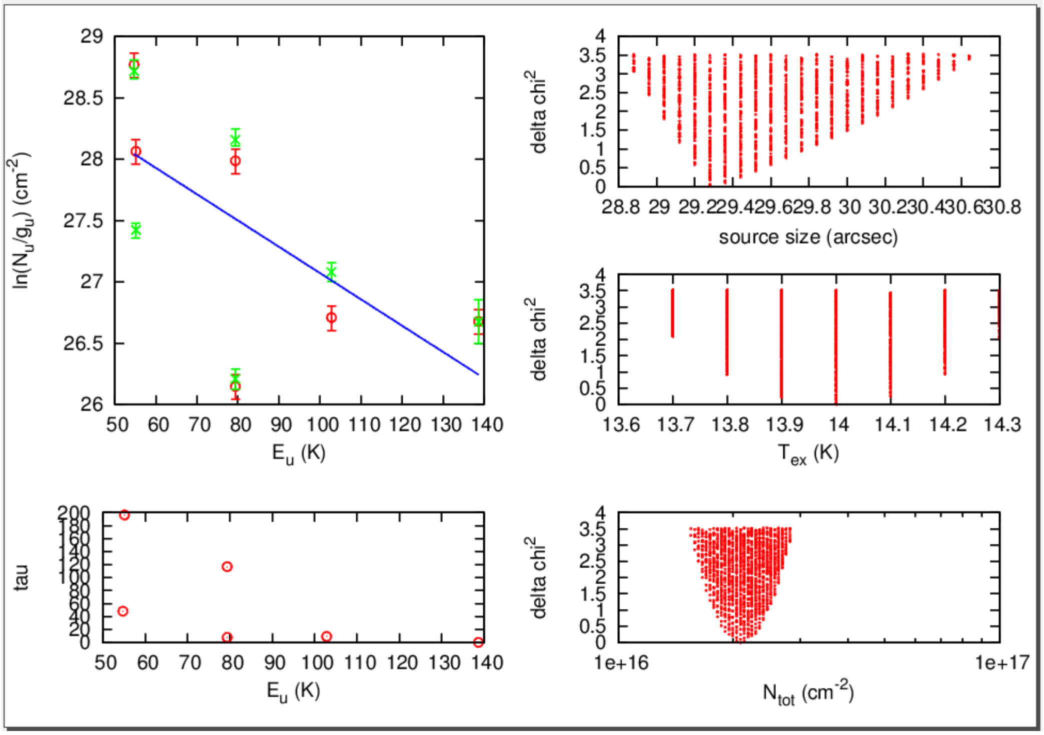

Figure 4.33: H_2S *population diagram.*

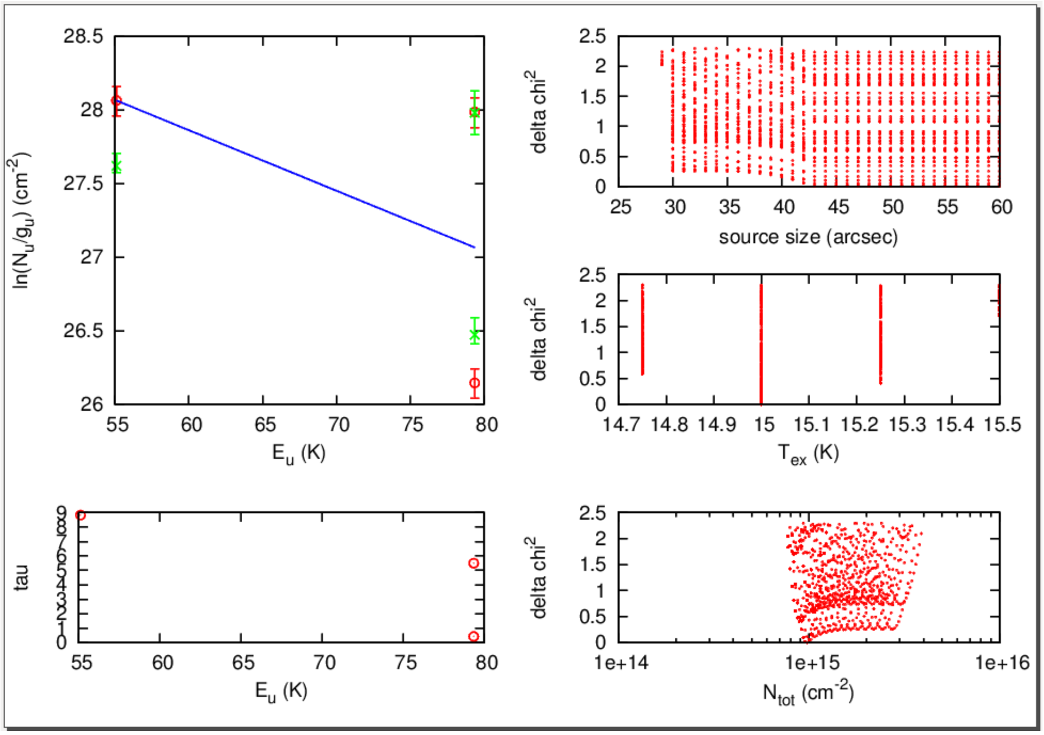

Figure 4.34: $o-H_2S$ *population diagram.*

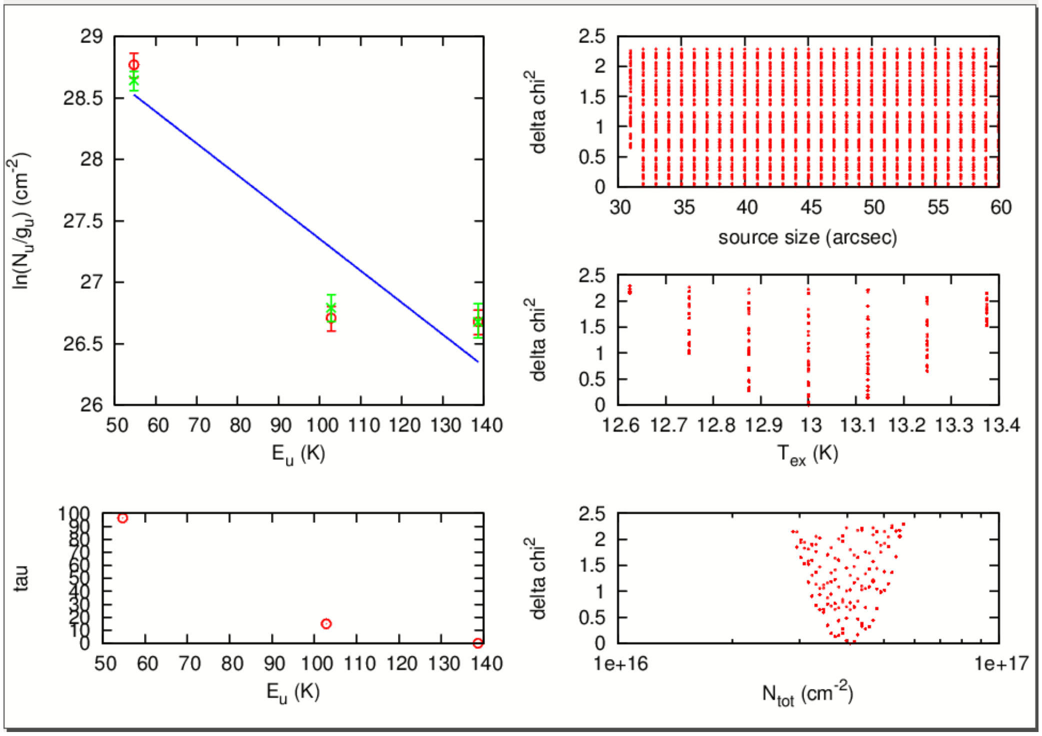

Figure 4.35: $p-H_2S$ *population diagram.*

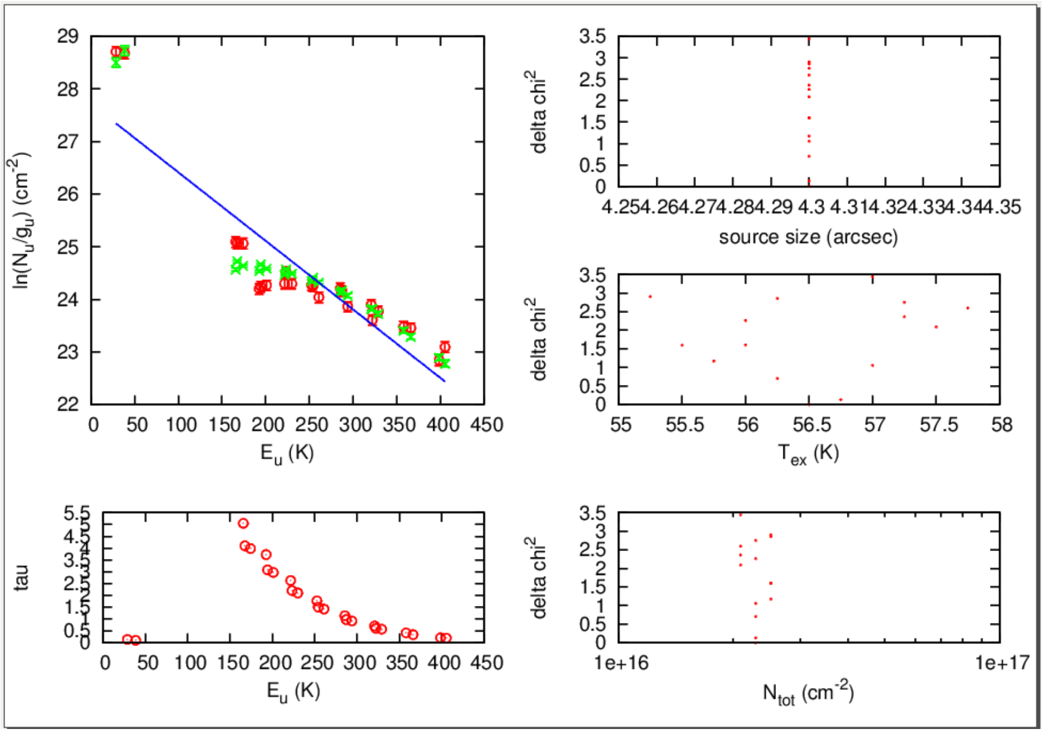

Figure 4.36: *SO population diagram.*

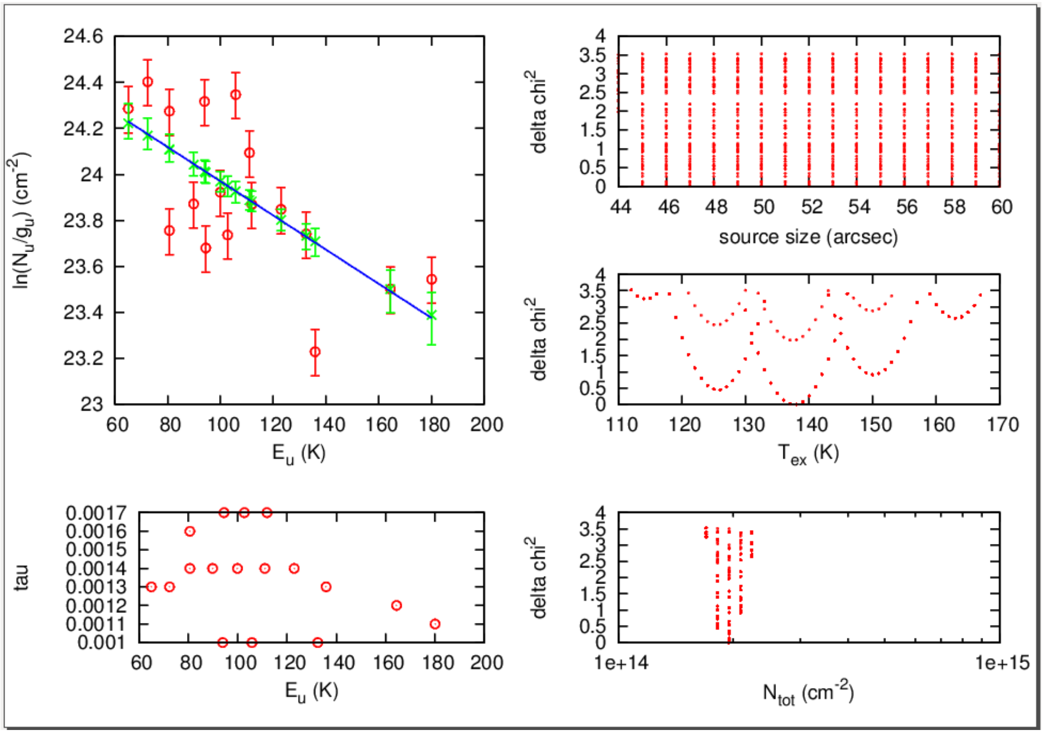

Figure 4.37: *SO_2 population diagram.*

Chapter 5

Conclusion

The study of massive stars is essential in understanding the evolution of the Universe for a number of reasons. They are believed to be a principle source of heavy elements. They can also have an important effect on the ISM through the combination of their winds, outflows, high energy photons (UV radiation) and magnetic fields. Supernova explosions can provide an important source of turbulence in the ISM. Therefore, massive stars can affect the star and planet formation process on large scales (Bally, Moeckel, & Throop 2005).

Although gravitational collapse explains, in a most basic sense, how stars are formed, the details of the process of star formation are still uncertain and depend critically on the initial conditions. Studying HMSF is even more challenging since high mass stars are statistically far less numerous than low mass stars (only 1% of stars have masses more than $10M_{\odot}$) and high mass stars evolve at least a factor of 10 faster than low mass stars. Studying them theoretically is also extremely complex. Therefore, in spite of the dominant role of high mass stars in the Galaxy, our understanding of their formation and evolution is still poor (Zinnecker & Yorke 2007).

Orion-KL and Orion-S, in the Orion nebula, are the closest regions of high mass star formation, in which Orion-S is believed to be at an earlier stellar evolutionary stage. The chemical signature of a star forming cloud changes as a function of core evolution (Bergin & Tafalla 2007). This may help to trace the history of gas contraction. Thus, extracting the detailed physical conditions of the HMSF regions in different sources can provide us with the key to understanding massive star formation. Finally, we can compare the results of the chemical abundances and physical conditions of one HMSF (Orion-S in our case) with other HMSF regions to see how chemical complexity and physical conditions changes from one region to another. These are both crucial parameters to compare against dynamical and chemical models of cloud evolution and star formation. Therefore, surveys of the physical and chemical conditions of a variety of star forming regions (both high and low mass) will help us determine differences in the process.

One of the goals of the HEXOS key project with the Herschel Space Observatory was to provide us with a better understanding of the chemical composition of massive star forming regions. Using the HIFI instrument aboard the Herschel space observatory, which operated over 479 GHz to 1901 GHz, we detected $\sim$ 800 spectral lines originating from 47 different species as well as some unidentified lines in Orion-S. We used two different methods to extract physical conditions in Orion-S, namely the population diagram method and LTE modelling. These results are listed in tables 4.7 and 4.6.

Our work, to obtain a complete chemical inventory of a young massive star forming region as well as to determine the physical conditions of the gas, is the first initial step in the process of cross region chemical and physical comparison. One of the future projects will be a comparison between our Orion-S results and Orion-KL, which is believed to be a more evolved stellar object. Although our analysis of Orion S is complete, we await the results of a similar analysis of the chemical abundances in Orion KL.

In addition to HEXOS, the CHESS survey (Chemical HErschel Surveys of Star forming regions) has surveyed a number of low mass star forming regions (at different stages of their evolution) over the same frequency range as HEXOS allowing for a direct comparison between high mass and low mass star forming regions. We also await the chemical analysis of these data in order to begin the cross comparison of HMSF regions vs LMSF regions.

Thus, ultimately, the work presented in this thesis will be used by myself and others to begin comparisons across regions of different masses and evolutionary stages. The goals of these comparisons are simple, and yet of fundamental importance to our understanding of star formation and the origin of chemical complexity in the Universe:

1. Using the full spectral scans from the HEXOS and CHESS surveys we will assess the chemical composition and abundances, as well as the physical parameters (column-density, density, temperature, emission size, etc.) of every detectable species in a sample of high and low mass star forming regions.
2. Using the information from 1. we will determine the physical and chemical conditions that are unique to each type of star forming region at each evolutionary stage and compare this to theoretical predictions of star formation models.
3. Using sophisticated chemical models (such as the Nahoon code developed at the U. of Bordeaux) we will determine the route by which the observed chemical complexity has arisen.

By comparing our observations and analysis in regions of low mass star formation, and those obtained for regions of high mass star formation, we will be able to address questions concerning how different star forming regions evolve both dynamically and chemically. What are the differences and similarities in the two processes? What chemical species specifically trace which stage of evolution in these different regions?

Bibliography

[1] : Adams, W. S. 1943, PASP. 55. 217A

[2] : Andre P., Menshchikov A., Bontemps S., et al., 2010, A& A, 518, L102

[3] : Arzoumanian, D., Andre, P., Didelon, P. et al., 2011, A& A, 529, L6

[4] : Baan, W. A., Henkel, C., Loenen, A. F., Baudry, A., & Wiklind, T. 2008, A& A, 477, 747

[5] : Bachiller, R., & Perez Gutierrez, M. 1997, ApJ, 487, L93

[6] : Beltrn M. T., Girart J. M., Estalella R., and Ho P. T. P. (2004a) Astron. Astrophys., 426, 941949.

[7] : Bennett, C. L., Fixsen, D. J., Hinshaw, G., et al. 1994, ApJ, 434, 587

[8] : Bergin, E. A., Phillips, T. G., Comito, C., et al. 2010, A& A, 521, L20+

[9] : Bergin, Plume, Williams and Myers, 1999, ApJ, 512, 724

[10] : Bergin, E., Tafalla, M., 2007, ARA& A, 45, 339

[11] : Beuther, H., Zhang, Q., Greenhill, L. J., et al. 2005, ApJ, 632, 355

[12] : Beuther, H., Zhang, Q., Sridharan, T. K., Lee, C.-F., & Zapata, L. A. 2006, A& A, 454, 221

[13] : Binney, J., & Tremaine, S. 1987, Nature, 326, 219

[14] : Blake G. A., Keene J., Phillips T. G., 1985, ApJ, 295, 501

[15] : Bonnell, I. A., Bate, M. R., Clarke, C. J., & Pringle, J. E. 2001, MNRAS, 323, 785

[16] : Boonman, A. M. S., Doty, S. D., van Dishoeck, E. F., et al. 2003, A& A, 406, 937

[17] : Boonman, A. M. S., Stark, R., van der Tak, F. F. S., van Dishoeck, E. F., van der Wal, P. B., Schafer, F., de Lange, G., & Laauwen, W. M. 2001, ApJ, 553, L63

[18] : Cambresy, L. 1999, A& A, 345, 965

[19] : Carr, J. S., Evans, N. J., II, Lacy, J. H., & Zhou, S. 1995, ApJ, 450, 667

[20] : Caselli, P., Benson, P. J., Myers, P. C., & Tafalla, M. 2002, ApJ, 572, 238

[21] : Caselli, P., Benson, P. J., Myers, P. C., & Tafalla, M. 2002, ApJ, 572, 238

[22] : Caselli, P., Keto, E., & Pagani, L., et al. 2011, A& A, 521, L29

[23] : Ceccarelli, C., Hollenbach, D.J., Tielens, A.G.G.M. 1996, ApJ, 471, 400

[24] : Cesaroni, R. 2005, Ap& SS, 295, 5

[25] : Class "Continumum and Line Analysis Single-dish Software, GILDAS software, 2006 ver.1.1

[26] : Crovisier J. 1999, In formation and Evolution of Solids in space, ed. JM Greenberg and A Li, p. 389. Dordecht: Kluwer.

[27] : de Graauw, T., Helmich, F. P., Phillips, T. G., et al. 2010, A& A, 518, L6

[28] : De Lucia, F. C., Helminger, P., & Gordy, W. 1971, Phys. Rev. A, 3, 1849

[29] : Dobashi K. and Uehara H. (2001) Publ. Astron. Soc. Japan, 53, 799 809

[30] : ESO - VLT Instruments. N.p., n.d. Web. 29 Apr. 2013

[31] : Evans, II, N. J. 1999, ARA& A, 37, 311

[32] : Ferriere K. M. 2001, Rev. Mod. Phys. 73, 1031

[33] : Field G. B., Goldsmith D. W., Habing H. J., 1969, ApJL, 155, L149

[34] : Fuente, A., Martin-Pintado, J., Cernicharo, J., & Bachiller, R. 1993, A& A, 276, 473

[35] : Fuente, A., Rizzo, J. R., Caselli, P., Bachiller, R., & Henkel, C. 2005b, A& A, 433, 535

[36] : Genzel, R. & Stutzki, J. 1989, ARA& A, 27, 41

[37] : Gerin, M. et al. 2010, A& A, 512, L16

[38] : Girart, J. M., Ho, P.T.P., Rudolph, A. L., Estalella

[39] : Goldreich P, Kwan J. 1974. Ap. J. Lett. 243:L75-78

[40] : Gomez-Gonzalez, J. 1997, ApJ, 476, 730

[41] : Gottlieb, C. A., Gottlieb, E. W., Litvak, M. M., Ball, J. A., & Peneld, H. 1978, ApJ, 219, 77

[42] : HIFI Observer's Manual 2011, ver. 20.4

[43] : HIFI Observers Manual, HERSCHEL-HSC-DOC-0784, ver. 2.4, 1 June 2011

[44] : Hollenbach, D. J. & Tielens, A. G. G. M. 1997, ARA& A, 35, 179

[45] : Iglesias E., Silk J., 1977, ApJ, 226, 851

[46] : Jijina J., Myers P. C., & Adams F. C. 1999, ApJSS, 125, 161

[47] : Juvela, M.; Harju, J.; Ysard, N.; Lunttila, T 2012, A& A, 538A.133J

[48] : Krugel 2003, The Physics of Interstellar Dust

[49] : Kwok S. 2007, Physics and Chemistry of the ISM

[50] : Langer W. D., Velusamy T., Pineda J. L., Goldsmith P. F., Li D., Yorke H. W., 2010, A& A, 521, L17

[51] : Lequeux 2003, The Interstellar Medium

[52] : Levrier F, Le Petit F, Hennebelle P, Lesaffre P, Gerin M, Falgarone E (2012) Astron Astrophys 544:22

[53] : Loren, R. B. 1989a, ApJ, 338, 902

[54] : Loren, R. B. 1989b, ApJ, 338, 925

[55] : Maret, S. & Bergin, E. A. 2007, ApJ, 664, 956.

[56] : Martin-Pintado, J., Bachiller, R., & Fuente, A. 1992, A& A, 254, 315

[57] : Mckee C. F., Ostriker J. P. 1977, ApJ, 218, 148

[58] : McMullin, J. P., Mundy, L. G., & Blake, G. A. 1993, ApJ, 405, 599

[59] : McMullin, J. P., Mundy, L. G., Wilking, B. A. et al. 1992, 1992AAS.18110302M

[60] : Melnick, G. J., et al. 2000a, ApJ, 539, L77

[61] : Motte F., Andre P., Neri R., 1998, A& A, 336, 150

[62] : Mul, P. M., & McGowan, J. W. 1980, ApJ, 237, 749

[63] : Myers, P.C. & Benson, P.J. 1983, ApJ, 266, 309

[64] : Naylor, D. A., Dartois, E., Habart, E., et al. 2010, A& A, 518, L117

[65] : Neufeld, D.A., Melnick, G.J. 1987, ApJ, 322, 266

[66] : Ossenkopf, V., & Henning, T. 1994, A& A, 291, 943

[67] : Palla, F. & Stahler, S. W. 1993, ApJ, 418, 414

[68] : Palmer, P., Zuckerman, B., Buhl, D., & Snyder, L. E. 1969, ApJ, 156, L147

[69] : Papadopoulos, P. P., Thi, W.-F., & Viti, S. 2004, MNRAS, 351, 147

[70] : Plume et al. 2013

[71] : Plume, R., Jae, D. T., & Evans, II, N. J. 1992, ApJS, 78, 505

[72] : Plume, R., Jae, D. T., Evans, N. J., II, Martin-Pintado, J., & Gomez-Gonzalez, J. 1997, ApJ, 476, 730

[73] : Roberts, H., Herbst, E., & Millar, T. J. 2003, ApJ, 591, L41

[74] : Robitaille T. P., Whitney B. A., 2010, ApJ, 710, L11

[75] : Rodgers, S. D., & Charnley, S. B. 2001a, ApJ, 546, 324

[76] : Rodrguez-Franco, A., Martn-Pintado, Wilson, T. L., 1999A& A, 351, 1103

[77] : Roelfsema, P. R., Helmich, F. P., Teyssier, D., et al. 2012, A& A, 537, A17

[78] : Romanini 2007, Sideband ratio in double side band

[79] : Salez, M., Frerking, M. A., & Langer, D. A. 1996, ApJ, 467, 708

[80] : Schilke P., Phillips T. G., Wang N., 1995, ApJ, 441, 334

[81] : Schilke, P., Benford, D. J., Hunter, T. R., Lis, D. C., & Phillips, T. G. 2001, ApJS, 132, 281

[82] : Schilke, P., Walmsley, C. M., Pineau Des Forets, G., et al. 1992, A& A, 256, 595

[83] : Sheer, Y., Rogers, M., & Federman, S. R. 2008, ApJ, 687, 1075

[84] : Shirley, Y.L., et al. 2003, ApJS, 149, 375

[85] : Spectrometer Spectral Resolution and Instrumental Profile. N.p., n.d. Web. 29 Apr. 2013.

[86] : Suzuki, H., Yamamoto, S., Ohishi, M., Kaifu, N., Ishikawa, S., Hirahara, Y., & Takano, S. 1992, ApJ, 392, 551

[87] : Swade D. A., 1989, ApJ, 345, 828

[88] : Swings, P., & Rosenfeld, L. 1937, ApJ, 86, 483

[89] : Tafalla M. and Myers P. C. (1997) Astrophys. J., 491, 653662

[90] : Takakuwa S., Ohashi N., and Hirano N. (2003) Astrophys. J., 590, 932 943.

[91] : Tielens 2005, The Physics and Chemistry of Interstellar Medium

[92] : Tielens A. G. G. M., Hollenbach D., 1985, ApJ, 291, 722

[93] : Tielens, A. G. G. M., & Hollenbach, D. 1985a, ApJ, 291, 747

[94] : van der Tak, F. F. S., van Dishoeck, E. F., Evans, II, N. J., Bakker, E. J., & Blake, G. A. 1999, ApJ, 522, 991

[95] : van Dishoeck EF, Blake GA. 1999 Annu. Rev. Astron. Astrophys. 36:317-68

[96] : van Dishoeck, E. F., & Black, J. H. 1988, ApJ, 334, 771

[97] : Vastel, Toulouse: IRAP, *http : //userpages.irap.omp.eu/ ∼ cvastel/Welcome_files/submm.pdf*

[98] : Velusamy, T., Langer, W. D., Pineda, J. L., & Goldsmith, P. F. 2012, A& A, 541, 10

[99] : Wannier, P. G., & Linke, R. A. 1978, ApJ, 226, 817

[100] : Washington, D.C.: National Academies, 2007. Exploring Organic Environments in the Solar System.

[101] : Wang, S., Bergin, E.A., Crockett, N.R., et al., 2011, Astron. & Astrophys., 527, A95.

[102] : Williams J. P., de Geus E. J., Blitz L., 1994, ApJ, 428, 693

[103] : Wilson T.L, Rohlf K,& Huttemeister S 2009, Tools of Radio Astronomy, 5th Ed

[104] : Wilson, T. L. & Matteucci, F. 1992, A& A Rev., 4, 1

[105] : Wolfire, M. G., Hollenbach, D. & McKee, C. F. 2010, ApJ 716, 1191

[106] : Womack, M., Ziurys, L. M., & Wycko, S. 1992, ApJ, 387, 417

[107] : Wootten, A., Loren, R. B., & Snell, R. L. 1982, ApJ, 255, 160

[108] : Wu, J., Evans, N. J., II, Shirley, Y. L., & Knez, C. 2010, ApJS, 188, 313

[109] : Young J. S., Scoville N. Z., 1991, ARA& A, 29, 581

[110] : Zapata, L. A., Rodrguez, L. F., Kurtz, S. E., & ODell, C. R. 2004, AJ, 127, 2252

[111] : Zapata, L. A., Rodriguez, L. F., Kurtz, S. E., ODell C. R., & Ho, P. T. P., 2004 ApJ, 610,121

[112] : Zinnecker, H. & Yorke, H. W. 2007, ARA& A, 45, 481

[113] : Ziurys, L. M., Wilson, T. L., Mauersberger, R., 1990, ApJ, 356, 25

Appendix A

Frequency List

Table A.1: *All observed lines above the 3σ noise level in order of increasing frequency.*

Band 1a

Frequency (GHz)	Intensity (K)	Species
480.2699	0.9	$A-CH_3OH$
481.5056	0.9	$A-CH_3OH$
481.9167	0.4	$C^{34}S$
482.2179	0.2	$A-CH_3OH$
482.2833	1.0	$E-CH_3OH$
482.9598	1.8	$E-CH_3OH$
483.0808	0.2	$A-CH_3OH$
483.1418	2.2	$E-CH_3OH$
483.3898	0.4	$E-CH_3OH$
483.3983	0.2	$A-CH_3OH$
483.4623	0.2	$A-CH_3OH$
483.4728	0.2	$E-CH_3OH$
483.5393	0.2	$A-CH_3OH$
483.5533	0.4	$A-CH_3OH$
483.5668	0.4	$E-CH_3OH$
483.5818	0.2	$A-CH_3OH$
483.6868	0.8	$E-CH_3OH$
483.7633	0.4	$A-CH_3OH$
484.0058	1.0	$A-CH_3OH$
484.0238	0.9	$E-CH_3OH$
484.0718	0.5	$E-CH_3OH$
484.2703	0.2	SO_2
485.2638	1.2	$A-CH_3OH$
486.9419	1.2	$A-CH_3OH$
487.5319	0.8	$A-CH_3OH$
487.6639	0.3	H_2CS
489.0379	1.1	$A-CH_3OH$
489.7509	6.0	CS
490.5970	0.3	HDO
491.5520	0.9	$A-CH_3OH$
491.9335	0.2	SO_2
491.9690	4.0	$o-H_2CO$
492.1615	6.2	$C-atom$
492.2795	2.6	$A-CH_3OH$
493.7000	1.8	$A-CH_3OH$
493.7350	1.8	$A-CH_3OH$
494.4820	0.8	$A-CH_3OH$
494.7781	0.3	SO_2
495.1741	1.6	$E-CH_3OH$
496.9226	0.1	$E-CH_3OH$
497.8296	0.6	$A-CH_3OH$
501.5897	0.5	$A-CH_3OH$
503.0142	0.1	$H_2^{34}S$
504.2008	0.3	DCO^+
504.2948	1.7	$E-CH_3OH$
504.6783	0.2	SO
505.5658	2.0	$o-H_2S$
505.7633	0.4	$A-CH_3OH$
505.8343	2.2	$p-H_2CO$
506.1548	0.3	$E-CH_3OH$
506.7728	0.3	H_2CS
506.8273	0.3	DCN
508.5369	0.2	^{13}CS
508.7069	0.2	SO_2
509.0924	0.2	$A-CH_3OH$
509.1469	1.0	$p-H_2CO$
509.2939	0.4	HDO
509.5654	1.0	$E-CH_3OH$ $\&o-H_2CO$
509.8314	0.4	$p-H_2CO$
510.1559	1.1	$o-H_2CO$
510.2389	1.2	$o-H_2CO$
510.3459	0.3	$A-CH_3OH$
510.9114	0.2	$HC^{18}O^+$
511.0904	0.2	SO_2
511.5024	0.2	SO_2
511.7199	0.1	U
511.9455	0.3	$A-CH_3OH$
512.2500	0.1	U
513.0775	0.9	$p-H_2CO$
513.3610	0.2	H_2CS
514.8535	0.9	SO
515.1700	0.3	$A-CH_3OH$
515.3335	0.2	$A-CH_3OH$
515.8230	0.2	U
516.2616	0.2	$A-CH_3OH$
516.3361	1.0	SO $\&H_2CS$
516.9826	0.1	U
517.3551	1.2	SO
517.9706	0.5	$H^{13}CN$
520.1801	1.6	$E-CH_3OH$
520.4612	1.5	$H^{13}CO^+$
520.7297	0.2	$A-CH_3OH$
520.8817	0.2	SiO
522.4057	0.2	H_2CS
523.1002	0.1	$E-CH_3OH$

Frequency (GHz)	Intensity (K)	Species
523.2752	0.4	$E-CH_3OH$
523.4827	0.1	$^{13}C^{18}O$
523.9727	2.9	CCH
524.0352	2.4	CCH
524.2682	0.1	$E-CH_3OH$
524.5847	0.1	$E-CH_3OH$
524.6673	0.1	$E-CH_3OH$
524.7418	0.2	$E-CH_3OH$
524.8053	0.2	$E-CH_3OH$
524.8628	0.3	$E-CH_3OH$
524.9098	0.3	$E-CH_3OH$
524.9483	0.2	$E-CH_3OH$
525.0548	0.1	$E-CH_3OH$
525.6663	3.3	$o-H_2CO$
526.0363	0.1	SH^+
526.0453	0.2	SH^+
526.5233	0.1	$A-CH_3OH$
526.5483	0.1	$E-CH_3OH$
526.7878	0.1	$E-CH_3OH$
527.0548	0.5	$A-CH_3OH$
527.1738	0.1	$E-CH_3OH$
527.2483	0.1	U
527.4523	0.1	U
527.6608	0.1	$E-CH_3OH$
528.1813	0.2	$E-CH_3OH$
528.2578	0.1	U
528.6833	0.1	$E-CH_3OH$
529.1419	0.2	$E-CH_3OH$
529.2904	0.2	SO_2
529.5409	0.3	$E-CH_3OH$
529.8679	0.3	$E-CH_3OH$
529.9739	0.2	SO_2
530.0699	0.3	$A-CH_3OH$
530.1234	0.4	$C^{34}S$
530.1849	0.8	$E-CH_3OH$
530.0244	0.1	$E-CH_3OH$
530.3174	0.5	$E-CH_3OH$
530.4559	0.6	$E-CH_3OH$
530.5499	0.6	$E-CH_3OH$
530.6124	0.6	$E-CH_3OH$
530.6484	0.6	$E-CH_3OH$
530.8244	0.2	$E-CH_3OH$
531.0804	1.5	$E-CH_3OH$
531.3199	1.7	$A-CH_3OH$
531.6384	0.3	$A-CH_3OH$
531.7159	9.9	HCN
531.8709	0.5	$A-CH_3OH$
531.8924	0.4	$A-CH_3OH$
532.0334	0.6	$E-CH_3OH$
532.0709	0.3	$E-CH_3OH$
532.1349	0.4	$A-CH_3OH$
532.3239	0.2	U
532.4669	0.8	$E-CH_3OH$
532.5684	0.5	$E-CH_3OH$
532.7214	3.2	CH
532.7909	1.3	CH
533.3810	0.2	U
535.0610	19.2	HCO^+
536.1925	0.8	$A-CH_3OH$
536.7585	2.8	CH
536.7805	0.7	CH
536.7925	1.2	CH
538.5716	2.8	$A-CH_3OH$
538.6891	4.5	CS
539.2806	0.1	$E-CH_3OH$
539.7551	0.1	U
540.4656	0.2	H_2CS
540.9236	0.2	$E-CH_3OH$
541.7536	0.2	SO_2
541.8162	0.2	SO_2
541.8502	0.2	U
542.0022	1.8	$A-CH_3OH$
542.0347	0.2	U
542.0832	1.8	$A-CH_3OH$
542.1472	0.2	U
542.4451	-0.1	U
542.4787	0.3	U
543.0777	1.5	$E-CH_3OH$
543.1107	1.8	U
543.3837	0.2	U
543.8987	0.1	HNC
544.4912	0.2	U
545.0437	0.2	$E-CH_3OH$ $\&A-CH_3OH$
545.1032	0.2	U
545.8872	0.2	U
546.2488	0.2	$A-CH_3OH$
546.4693	0.1	U
547.3003	0.2	U
547.6768	0.4	$H_2^{18}O$
548.0593	0.1	U

Frequency (GHz)	Intensity (K)	Species
548.4773	0.1	U
548.8313	10.7	$C^{18}O$
549.2998	0.2	SO_2
549.5533	0.1	NO
550.6564	0.1	$A-CH_3OH$
550.9254	38.7	^{13}CO
551.1874	0.4	NO
551.2309	0.1	$A-CH_3OH$ &NO
551.5159	0.1	U
551.5344	0.4	NO
553.1474	1.3	$E-CH_3OH$
553.2059	0.1	NO
553.7644	0.1	$A-CH_3OH$
553.8944	0.1	U
554.0569	0.2	$E-CH_3OH$
554.4989	0.0	U
554.5269	0.1	U
554.5784	0.1	NO
554.7275	0.1	^{13}CS
555.6670	0.1	SO_2
556.8340	0.3	U
556.9370	9.5	$o-H_2O$
557.1260	0.2	H_2CS
558.0870	0.4	SO
558.3465	0.5	$E-CH_3OH$
558.9681	3.3	N_2H^+
559.3216	0.6	SO
560.1781	0.6	SO
560.2496	0.3	$E-CH_3OH$
560.2716	0.3	$E-CH_OH$
560.3001	0.2	U

Band 1b

Frequency (GHz)	Intensity (K)	Species
556.9370	11.1	$o-H_2O$
558.0875	0.6	SO
558.3460	0.6	$E-CH_3OH$
558.9681	4.5	N_2H^+
559.3206	0.7	SO
560.1781	0.8	SO
560.2781	-0.3	U
561.7136	3.9	$C^{17}O$
561.9001	3.5	$o-H_2CO$
563.4825	-0.3	U
564.2522	0.2	SiO
566.7312	1.7	CN
566.9052	0.2	U
566.9477	2.1	CN
567.2612	0.2	U
567.4618	0.3	SiN
567.5953	0.2	SO_2
568.2358	0.2	$E-CH_3OH$
568.4383	0.2	U
568.5673	1.7	$E-CH_3OH$
568.7853	0.2	$A-CH_3OH$
572.4974	4.3	$o-NH_3$
572.8984	0.3	$E-CH_3OH$
572.9119	0.1	$A-CH_3OH$
573.4714	0.1	$E-CH_3OH$
574.1399	0.2	H_2CS
574.8084	0.2	SO_2
574.8694	0.4	$A-CH_3OH$
576.2050	0.7	DCO^+
576.2660	81.6	CO
576.3835	0.4	U
576.7095	1.5	$p-H_2CO$
578.0080	0.6	$E-CH_3OH$
578.2165	0.2	$C^{34}S$
579.0860	1.8	$A-CH_3OH$
579.1520	1.1	$E-CH_3OH$
579.1995	0.1	DCN
579.4605	1.2	$A-CH_3OH$
579.8590	0.3	$A-CH_3OH$
579.9225	1.9	$A-CH_3OH$
580.0600	0.2	$A-CH_3OH$
580.1760	0.3	$A-CH_3OH$
580.2135	0.3	$A-CH_3OH$
580.3696	0.4	$E-CH_3OH$
580.4446	0.2	$E-CH_3OH$

Frequency (GHz)	Intensity (K)	Species
580.5026	0.3	$A-CH_3OH$
580.9036	0.6	$E-CH_3OH$
581.0916	0.3	$E-CH_3OH$
581.6131	0.6	$p-H_2CO$
582.3841	0.3	$o-H_2CO$
582.7246	0.3	$p-H_2CO$
583.1456	0.8	$o-H_2CO$
583.3096	0.7	$o-H_2CO$
584.2841	0.2	U
584.4511	2.6	$A-CH_3OH$
584.5602	0.1	U
584.8227	0.6	$A-CH_3OH$
585.5087	0.2	U
587.0032	0.2	U
587.4537	0.6	$p-H_2CO$
587.5702	0.2	SO_2
587.6167	3.0	CS
587.6582	0.2	U
588.1618	-0.3	U
589.8703	0.1	CO^+ *
590.2793	1.5	$A-CH_3OH$
590.4418	1.5	$A-CH_3OH$
590.7533	0.2	U
590.7923	1.2	$E-CH_3OH$
591.8218	0.2	H_2CS
593.9424	0.2	SO_2
593.9624	0.1	SO_2
597.2084	0.1	U
598.5485	-0.1	U
599.9280	0.3	HDO
600.0380	0.1	U
600.3320	2.3	$o-H_2CO$
600.9065	0.1	^{13}CS
601.2570	0.6	SO
601.8521	0.2	$E-CH_3OH$
602.2346	1.1	$E-CH_3OH$
602.2916	0.5	SO
603.0236	0.6	SO
604.2641	0.3	$H^{13}CN$
604.3696	0.2	SO_2
605.8801	0.2	$E-CH_3OH$
607.1762	1.0	$H^{13}CO^+$
607.2167	0.4	$E-CH_3OH$
607.6112	0.2	SiO
607.7982	0.2	H_2CS
608.0027	0.2	U

Frequency (GHz)	Intensity (K)	Species
608.1007	0.1	U
609.7122	0.1	U
611.2688	1.6	CCH
611.3308	1.3	CCH
611.5518	0.2	SO
613.0798	0.2	SO_2
615.2824	0.1	U
616.9814	1.6	$E-CH_3OH$
620.3035	7.4	HCN
620.7045	0.7	$o-H_2O$
622.5705	0.2	$A-CH_3OH$
622.6605	0.4	$A-CH_3OH$
622.7755	0.3	$E-CH_3OH$
624.1801	0.2	$E-CH_3OH$
624.2081	17.4	HCO^+
624.9616	1.3	$H^{37}Cl$
624.9751	1.8	$H^{37}Cl$
624.9856	0.9	$H^{37}Cl$
625.7521	0.5	$E-CH_3OH$
625.7601	0.2	$A-CH_3OH$
625.8996	2.8	HCl
625.9166	3.7	HCl
625.9296	2.0	HCl
626.0896	0.2	SO_2
626.3521	0.2	$C^{34}S$
626.4996	0.2	H_2CS
626.5141	0.1	$A-CH_3OH$
626.5566	0.2	$E-CH_3OH$
626.6271	2.0	$A-CH_3OH$
627.0261	0.2	U
627.1036	0.1	U
627.1721	0.8	$E-CH_3OH$
627.5602	0.9	$A-CH_3OH$
628.0522	0.3	$A-CH_3OH$
628.1422	0.2	$^{13}C^{18}O$
628.3302	0.2	$E-CH_3OH$
628.4482	0.2	$E-CH_3OH$
628.4717	0.4	$A-CH_3OH$
628.5142	0.3	$A-CH_3OH$
628.5272	0.3	$A-CH_3OH$
628.6722	0.2	U
628.6982	0.4	$E-CH_3OH$
628.8182	0.3	$E-CH_3OH$
628.8682	0.3	$A-CH_3OH$
122629.1417	2.1	$A-CH_3OH$
629.3232	0.5	$E-CH_3OH$

Frequency (GHz)	Intensity (K)	Species
629.6517	0.3	$E-CH_3OH$
629.9222	2.3	$A-CH_3OH$
631.0137	0.2	U
631.2847	0.3	U
631.7038	2.2	$o-H_2CO$
632.1918	0.2	SO_2
633.4248	0.5	$A-CH_3OH$
634.5118	0.7	HNC
635.8673	0.4	$A-CH_3OH$
636.3394	0.7	$A-CH_3OH$
636.3979	0.6	$A-CH_3OH$
636.4209	0.8	$A-CH_3OH$

Band 2a

Frequency (GHz)	Intensity (K)	Species
626.5191	0.9	$A-CH_3OH$
626.6271	1.7	$A-CH_3OH$
627.1711	0.8	$E-CH_3OH$
627.5607	0.7	$A-CH_3OH$
629.1417	1.3	$A-CH_3OH$
629.3242	0.5	$E-CH_3OH$
628.5798	-0.5	U
629.6482	0.4	$E-CH_3OH$
629.9232	1.6	$A-CH_3OH$
630.9572	0.2	$A-CH_3OH$
631.7038	1.7	$o-H_2CO$
632.5258	0.3	U
633.4233	0.4	$A-CH_3OH$
634.5113	0.7	HNC
636.2514	0.3	$A-CH_3OH$
636.2749	0.4	$A-CH_3OH$
636.3059	0.4	$A-CH_3OH$
636.3349	0.4	$A-CH_3OH$
636.3669	0.5	$A-CH_3OH$
636.3949	0.5	$A-CH_3OH$
636.4209	0.4	$A-CH_3OH$
636.5199	0.4	$A-CH_3OH$
636.5339	1.7	CS
638.2429	0.2	U
638.2804	1.0	$E-CH_3OH$
638.5259	1.3	$A-CH_3OH$
638.8194	1.2	$A-CH_3OH$
644.3790	0.5	SO
645.2211	0.3	U
645.2576	0.5	SO
645.8756	0.5	SO
646.3781	0.2	U
647.0676	0.2	U
647.0831	1.1	$p-H_2CO$
647.6146	0.3	U
648.1956	0.3	DCO^+
649.5402	0.2	$E-CH_3OH$
651.2997	0.2	SO_2
651.4352	0.4	NO
651.6177	0.8	$E-CH_3OH$
651.7742	0.5	NO
652.0972	3.8	N_2H^+
653.9703	0.6	$p-H_2CO$
655.0433	0.2	U
655.0553	0.2	U

Frequency (GHz)	Intensity (K)	Species
655.2128	0.3	$o{-}H_2CO$
655.6353	0.3	$p{-}H_2CO$
656.1653	0.8	$o{-}H_2CO$
656.1723	0.5	$E{-}CH_3OH$
656.4663	0.7	$o{-}H_2CO$
658.5544	10.2	$C^{18}O$
661.0659	40.4	^{13}CO
662.2105	0.6	$p{-}H_2CO$
665.2485	0.2	SO_2
665.4440	1.7	$E{-}CH_3OH$
670.3602	0.2	SO_2
670.4242	0.4	$A{-}CH_3OH$
670.5663	-0.4	U
672.4117	0.2	U
672.5657	0.2	SO_2
672.7747	0.2	U
672.8362	0.2	$A{-}CH_3OH$
672.9037	0.4	$E{-}CH_3OH$
673.0102	0.3	U
673.4172	0.5	$E{-}CH_3OH$
673.7472	1.9	$A{-}CH_3OH$
674.0107	3.1	$C^{17}O$
674.8113	1.5	$o{-}H_2CO$
674.9913	1.8	$A{-}CH_3OH$ $\&E{-}CH_3OH$
675.0558	0.3	H_2CS
675.1353	0.7	$E{-}CH_3OH$
675.6138	0.7	$A{-}CH_3OH$
675.7748	1.0	$E{-}CH_3OH$
675.9168	-0.4	U
676.2143	0.4	$A{-}CH_3OH$
676.4618	0.2	SO_2
676.7523	0.4	$A{-}CH_3OH$
676.8298	0.4	$A{-}CH_3OH$
677.0138	0.3	$E{-}CH_3OH$
677.3354	-0.4	U
677.7113	0.5	$E{-}CH_3OH$
678.2528	0.3	$E{-}CH_3OH$
678.7688	0.2	U
678.7864	2.1	$A{-}CH_3OH$
680.0223	-0.5	U
680.0429	0.8	CN
680.2599	1.0	CN
681.3079	-0.4	U
681.5069	0.2	U
681.5354	0.2	U

Frequency (GHz)	Intensity (K)	Species
681.9919	0.6	$A{-}CH_3OH$
685.4375	1.4	CS
685.5050	0.8	$E{-}CH_3OH$
686.7325	0.9	$A{-}CH_3OH$
687.1515	0.2	$H_2^{33}S$
687.2270	1.0	$A{-}CH_3OH$
687.3040	3.0	$p{-}H_2S$
687.4571	0.5	SO
688.2021	0.4	SO
688.7286	0.4	SO
690.5551	0.3	$H^{13}CN$
691.4706	85.9	CO
693.8787	0.6	$H^{13}CO^+$
697.1083	0.2	U
697.1448	0.2	$E{-}CH_3OH$
698.5458	0.8	CCH
698.6083	0.8	CCH
701.3709	1.8	$o{-}H_2CO$ $OrE{-}CH_3OH$
701.4529	0.4	U
701.7549	0.2	U
702.7149	0.3	U
703.2294	0.1	$A{-}CH_3OH$
703.5174	0.2	U
703.9509	0.4	U
704.2609	0.2	U
704.4134	0.2	U
704.7775	0.2	U
704.9400	0.6	U
705.1840	0.4	$E{-}CH_3OH$
705.2325	0.5	U
705.4000	0.3	U
705.9605	0.5	U
706.6255	0.4	U
706.7675	0.4	U
707.3180	0.6	U
707.7905	0.6	U
708.4735	0.7	$O{-}H_2S$ $\&H_2^{33}S$
708.7085	0.5	U
708.8256	0.3	U
708.8741	4.2	HCN
709.2771	0.4	U
713.3422	13.3	HCO^+
124713.9837	1.3	$E{-}CH_3OH$
716.9402	0.7	$p{-}H_2CO$

Frequency (GHz)	Intensity (K)	Species
718.1618	0.3	$A-CH_3OH$
718.4378	1.2	$E-CH_3OH$
719.6653	1.5	$A-CH_3OH$
719.7293	1.4	U
719.8603	0.5	U
719.9548	1.9	U
720.0118	1.2	$E-CH_3OH$
720.4418	1.6	$A-CH_3OH$
721.0118	0.3	$E-CH_3OH$
723.0404	0.6	$E-CH_3OH$
723.6219	0.5	$A-CH_3OH$
724.1224	1.0	$E-CH_3OH$
724.3489	0.5	$A-CH_3OH$
725.0954	1.2	U

Band 2b

Frequency (GHz)	Intensity (K)	Species
716.9412	0.8	$p-H_2CO$
718.1623	0.4	$A-CH_3OH$
718.4378	1.3	$E-CH_3OH$
719.6668	1.5	$A-CH_3OH$
720.4433	1.9	$A-CH_3OH$
721.0093	0.5	$E-CH_3OH$
723.0429	0.6	$E-CH_3OH$
723.2824	0.4	$E-CH_3OH$
723.6199	0.6	$A-CH_3OH$
724.1219	1.1	$E-CH_3OH$
724.3409	0.3	$A-CH_3OH$
725.1089	0.4	HNC
725.1279	0.4	$A-CH_3OH$
725.3169	0.3	$E-CH_3OH$
726.0540	0.3	$E-CH_3OH$
726.2100	0.5	$p-H_2CO$
726.9025	0.4	$E-CH_3OH$
728.0535	0.4	$o-H_2CO$
728.5860	0.3	$p-H_2CO$
728.5960	0.3	$p-H_2CO$
728.8650	2.0	$A-CH_3OH$
729.2120	0.7	$o-H_2CO$
729.7260	0.5	$o-H_2CO$
730.5006	0.5	SO
730.5206	0.5	$A-CH_3OH$
731.1416	0.4	SO
731.5981	0.4	SO
732.4336	0.7	$A-CH_3OH$
732.7761	0.2	$^{13}C^{18}O$
734.2706	0.5	$H_2^{34}S$
734.3286	1.1	CS
734.8952	0.8	$A-CH_3OH$
735.6762	0.8	$A-CH_3OH$
736.0317	5.7	$o-H_2S$
737.3407	0.5	$p-H_2CO$
737.6272	0.2	$?A-CH_3OH?$
740.0043	0.3	$?A-CH_3OH?$
741.2263	0.3	$E-CH_3OH$
742.2408	0.2	H_2CS
745.2119	2.4	N_2H^+
747.3035	0.4	$p-H_2S$
749.0735	1.1	$o-H_2CO$
751.5560	0.5	$E-CH_3OH$
751.6766	0.4	NO
752.0321	10.6	$p-H_2O$

Frequency (GHz)	Intensity (K)	Species
752.1076	0.8	$E\!-\!CH_3OH$
752.1366	0.6	$E\!-\!CH_3OH$
752.1716	0.4	$E\!-\!CH_3OH$
752.3111	0.4	$E\!-\!CH_3OH$
753.4161	0.2	HDO
753.7041	0.2	U
753.8671	0.1	$E\!-\!CH_3OH$
754.2226	0.3	$E\!-\!CH_3OH$
762.6378	1.1	$E\!-\!CH_3OH$
763.6248	0.2	U
763.8823	0.4	$E\!-\!CH_3OH$
763.9533	1.1	$A\!-\!CH_3OH$
764.5828	-0.5	*down*
764.8119	0.3	$E\!-\!CH_3OH$
765.5134	0.3	$E\!-\!CH_3OH$
765.9404	0.2	
766.0309	0.4	$E\!-\!CH_3OH$
766.3974	0.5	$E\!-\!CH_3OH$
766.6489	0.7	$E\!-\!CH_3OH$
766.7124	1.6	$A\!-\!CH_3OH$
766.7624	1.1	$E\!-\!CH_3OH$
766.8114	0.6	$E\!-\!CH_3OH$
766.9094	0.6	$E\!-\!CH_3OH$
766.9614	0.7	$E\!-\!CH_3OH$
766.9844	0.7	$E\!-\!CH_3OH$
768.2529	7.5	$C^{18}O$
768.5404	0.3	$E\!-\!CH_3OH$
768.7645	0.2	U
770.8855	0.5	$E\!-\!CH_3OH$
770.8980	1.2	$o\!-\!H_2CO$
771.1825	36.1	^{13}CO
771.5770	0.5	$A\!-\!CH_3OH$
772.4425	0.3	$A\!-\!CH_3OH$
772.4545	0.8	$E\!-\!CH_3OH$
773.2611	0.3	$A\!-\!CH_3OH$
773.4226	0.4	$A\!-\!CH_3OH$
773.5136	0.4	SO
773.8896	0.3	$E\!-\!CH_3OH$
773.9481	0.3	$A\!-\!CH_3OH$
774.0666	0.3	SO
774.3331	0.4	$E\!-\!CH_3OH$
774.4541	0.3	SO
775.5996	0.5	$E\!-\!CH_3OH$
776.3411	0.3	U
778.1672	0.3	U
779.0072	0.7	$A\!-\!CH_3OH$
779.0322	0.6	$E\!-\!CH_3OH$
779.3822	1.7	$A\!-\!CH_3OH$
780.5672	0.4	$H^{13}CO^+$
781.6783	0.2	U
783.0028	0.6	$A\!-\!CH_3OH$
783.1993	0.7	CS
784.1793	0.5	$A\!-\!CH_3OH$
785.8058	0.3	CCH
785.8679	0.2	CCH
786.2829	2.0	$C^{17}O$ &$p\!-\!H_2CO$
788.1949	0.3	U
788.4619	0.3	U
789.9244	1.0	U
790.9360	0.9	U
793.3410	0.5	CN
793.5480	0.5	CN
794.5211	0.3	U
794.8206	0.3	U
796.2961	0.3	U
797.4306	2.2	HCN
798.3106	0.2	$p\!-\!H_2CO$
800.9837	1.4	U

Band 3a

Frequency (GHz)	Intensity (K)	Species
802.2430	0.4	$E-CH_3OH$
802.2810	0.4	$o-H_2CO$
802.4590	9.5	HCO^+
803.1130	0.4	$o-H_2CO$
806.6501	79.2	CO
807.8661	0.8	$A-CH_3OH$
809.3431	9.1	$C-atom$
811.4452	0.8	$E-CH_3OH$
812.5522	1.1	$A-CH_3OH$
813.5442	0.2	$A-CH_3OH$
814.9003	0.6	U
815.0723	1.0	$E-CH_3OH$
815.6503	0.3	U
815.6943	0.1	HNC
816.0153	0.2	$E-CH_3OH$
816.4953	0.2	SO
816.8123	0.3	U
816.9743	0.2	SO
817.3143	0.2	SO
817.6293	0.4	U
818.2414	0.3	U
818.6674	0.3	$E-CH_3OH$
819.4844	0.4	$A-CH_3OH$
820.5024	0.3	$A-CH_3OH$
820.7644	0.6	$E-CH_3OH$
821.4142	-0.3	U
821.4774	0.3	$A-CH_3OH$
821.7014	0.3	$A-CH_3OH$
821.8694	0.3	$E-CH_3OH$
822.1675	-0.4	U
822.5475	0.4	$E-CH_3OH$
823.0845	0.8	$o-H_2CO$
824.2335	0.2	SiO
824.3525	0.3	$E-CH_3OH$
824.7255	0.2	$E-CH_3OH$
825.2795	0.4	$E-CH_3OH$
827.4516	0.3	$A-CH_3OH$
829.8906	0.9	$A-CH_3OH$
830.3506	1.3	$A-CH_3OH$
831.0487	0.4	$A-CH_3OH$
832.0627	0.7	CS
832.7567	0.5	$A-CH_3OH$
834.6517	0.3	$E-CH_3OH$
834.7517	0.2	$E-CH_3OH$
834.8397	0.2	$E-CH_3OH$
834.9017	0.2	$E-CH_3OH$
834.9577	0.3	$E-CH_3OH$
835.0037	0.2	$E-CH_3OH$
835.1358	4.1	CH^+
836.6438	0.2	U
838.3088	1.1	N_2H^+
840.2779	0.7	$o-H_2CO$
851.4161	1.0	$A-CH_3OH$
851.9151	0.3	NO
853.5112	0.4	$E-CH_3OH$
855.1542	0.4	$p-H_2CO$
857.9613	0.9	$A-CH_3OH$

Band 3b

Frequency (GHz)	Intensity (K)	Species
860.4618	0.7	$E-CH_3OH$
863.3639	0.9	$E-CH_3OH$
863.4269	0.3	$E-CH_3OH$
867.3250	0.3	$A-CH_3OH$
869.0370	0.7	$E-CH_3OH$
869.5321	0.5	U
869.9821	0.3	$A-CH_3OH$
870.1091	0.3	$E-CH_3OH$
870.2811	0.3	$p-H_2CO$
873.0361	0.2	CCH
873.7811	0.2	$o-H_2CO$
875.3692	0.2	$o-H_2CO$
876.6462	0.2	$o-H_2CO$
877.9232	4.5	$C^{18}O$
878.2273	0.9	$A-CH_3OH$
879.0153	0.3	$A-CH_3OH$
880.9043	0.5	CS
881.2703	28.8	^{13}CO
881.4223	0.4	$A-CH_3OH$
881.7833	1.1	$A-CH_3OH$
885.9014	0.2	U
885.9664	1.6	HCN
890.1265	0.3	$E-CH_3OH$
891.5586	7.4	HCO^+
891.7045	-0.3	U
892.9375	-0.3	U
893.6387	-0.7	HDO
894.6146	0.6	$A-CH_3OH$
896.8077	0.4	$o-H_2CO$
898.5247	1.2	$C^{17}O$
898.9777	0.2	U
900.9658	0.2	$E-CH_3OH$
902.9388	0.7	$A-CH_3OH$
902.9838	0.3	U
905.3959	0.3	$E-CH_3OH$
906.5939	0.3	CN
906.8029	0.2	CN
906.9998	-0.3	U
909.5120	0.4	$o-H_2CO$
909.7400	0.5	$E-CH_3OH$
910.8110	0.3	$E-CH_3OH$
911.6440	0.6	$E-CH_3OH$
912.1100	1.1	$E-CH_3OH$
916.1771	0.7	$p-H_2O$
916.6502	0.4	$E-CH_3OH$
917.2702	0.5	$E-CH_3OH$
917.4082	0.3	$E-CH_3OH$
921.7973	79.4	CO
921.9873	0.6	$E-CH_3OH$
923.5853	0.3	$p-H_2CO$
926.5564	0.6	$A-CH_3OH$
926.8944	0.3	$A-CH_3OH$
929.7315	0.4	CS
930.2035	0.4	$A-CH_3OH$
931.3885	0.6	N_2H^+
933.6945	0.8	$A-CH_3OH$
933.8126	0.1	$down$
937.4826	0.5	$A-CH_3OH$
947.4759	0.5	$A-CH_3OH$
952.5740	-1.1	U

Band 4a

Frequency (GHz)	Intensity (K)	Species
960.4732	0.9	$E-CH_3OH$
965.4513	0.6	$E-CH_3OH$
974.4895	1.0	HCN
974.5895	0.5	U
974.6895	0.4	$A-CH_3OH$
974.8795	0.7	$A-CH_3OH$
980.0316	0.5	$A-CH_3OH$
980.6376	5.8	HCO^+
986.1018	0.8	$A-CH_3OH$
987.5618	3.0	$C^{18}O$
987.9298	11.5	$p-H_2O$
991.3259	23.8	^{13}CO
991.5839	0.7	$A-CH_3OH$
993.1019	2.3	$o-H_2S$
1002.7782	1.1	$p-H_2S$
1006.1242	0.6	$E-CH_3OH$
1008.8183	0.8	$E-CH_3OH$
1010.7323	0.9	$C^{17}O$
1013.5664	0.6	$E-CH_3OH$
1014.1764	0.5	U
1023.1986	0.8	$A-CH_3OH$
1024.8185	-0.8	U
1025.1307	0.7	U
1027.2887	0.4	U
1036.6990	1.4	SO_2
1036.9070	90.4	CO
1039.0150	0.7	$A-CH_3OH$
1057.1194	0.7	$E-CH_3OH$

Band 4b

1057.1239	0.7	$E-CH_3OH$
1061.9200	0.9	
1062.9821	1.3	HCN
1069.6982	3.7	HCO^+
1072.8303	1.3	$o-H_2S$
1092.4668	0.6	$A-CH_3OH$
1097.1589	1.9	$C^{18}O$
1097.3689	4.6	$o-H_2O$
1101.3450	17.0	^{13}CO
1101.6990	-0.7	U
1105.3691	0.6	$E-CH_3OH$
1113.3472	5.4	$p-H_2O$

Band 5a

Frequency (GHz)	Intensity (K)	Species
1113.3477	5.4	$p-H_2O$
1119.8339	0.7	$A-CH_3OH$
1122.9060	0.4	$C^{17}O$
1151.4506	0.9	HCN
1151.9826	79.7	CO
1152.9207	1.0	U
1153.1267	6.8	$o-H_2O$
1153.5527	1.0	$E-CH_3OH$
1158.7328	2.7	HCO^+
1162.7149	0.9	$A-CH_3OH$ $\&E-CH_3OH$
1162.9129	6.8	$o-H_2O$
1168.1190	0.8	$A-CH_3OH$
1168.4524	-1.1	$p-NH_3$
1196.0197	0.7	$o-H_2S$
1206.7279	1.1	$C^{18}O$
1207.6540	0.8	$p-H_2O$
1211.3260	10.7	^{13}CO
1214.8529	-1.0	$o-NH_3$
1215.2457	-1.3	$p-NH_3$
1228.7924	2.1	$p-H_2O$
1232.4685	-2.2	U

Band 5b

1228.7922	2.7	$p-H_2O$
1232.4724	-1.2	U
1239.9125	0.6	HCN
1247.7406	1.3	HCO^+
1267.0091	69.6	CO

Band 6a

1496.9192	58.3	CO

Band 6b

1611.7859	51.9	CO

Band 7a

1726.5976	39.0	CO

Band 7b

1841.3367	29.2	CO
1900.5261	84.9	C^+

Appendix B

Table of Species

Table B.1: *Gaussian fits to observed lines of each species. Superscript "b" means it is a blended line and excluded.*

CO

	Transition J	Frequency MHz	T_{mb} (K)	V_{lsr} (km s^{-1})	ΔV_{FWHM} (km s^{-1})	$\int T_{mb}dV$ (K km s^{-1})
Main	5 → 4	576267.409	69.09	7.27	6.31	463.75
Wing	5 → 4	576267.626	10.16	7.16	19.07	206.14
Main	6 → 5	691472.705	64.29	7.16	5.83	398.72
Wing	6 → 5	691472.711	15.87	7.16	17.57	296.87
Main	7 → 6	806653.108	62.08	6.52	5.01	331.27
Wing	7 → 6	806651.379	10.38	7.16	22.42	247.34
Main	8 → 7	921801.294	60.25	6.48	5.08	325.95
Wing	8 → 7	921799.213	9.74	7.16	23.80	245.97
Main	9 → 8	1036911.446	61.83	7.27	6.00	394.88
Wing	9 → 8	1036911.845	15.76	7.16	18.02	302.33
Main	10 → 9	1151987.559	61.44	6.45	4.64	303.25
Wing	10 → 9	1151987.373	8.61	6.50	22.97	209.93
Main	11 → 10	1267014.098	48.72	7.09	5.00	259.32
Wing	11 → 10	1267016.599	16.94	6.50	15.00	270.43
Main	13 → 12	1496920.455	41.40	7.49	4.82	212.16
Wing	13 → 12	1496925.406	12.01	6.50	18.24	233.22
Main	14 → 13	1611790.990	39.60	7.47	4.90	206.43
Wing	14 → 13	1611792.666	6.82	7.16	21.94	159.10
Main	15 → 14	1726597.844	28.26	7.81	3.49	104.88
Wing	15 → 14	1726601.593	8.60	7.16	14.00	128.17
Main	16 → 15	1841340.607	19.37	7.80	4.00	82.46
Wing	16 → 15	1841344.532	5.50	7.16	15.00	87.77
					Total flux:	5470.34

$^{13}C^{18}O$

	Transition J	Frequency MHz	T_{mb} (K)	V_{lsr} (km s^{-1})	ΔV_{FWHM} (km s^{-1})	$\int T_{mb}dV$ (K km s^{-1})
	5 → 4	523484.353	0.15	6.90	3.64	0.58
	6 → 5	628141.567	0.14	6.75	3.00	0.46
	7 → 6	732775.976	0.19	7.06	3.87	0.78
					Total flux:	1.82

^{13}CO

Transition J	Frequency MHz	T_{mb} (K)	V_{lsr} (km s^{-1})	ΔV_{FWHM} (km s^{-1})	$\int T_{mb}dV$ (K km s^{-1})
5 → 4	550926.285	39.26	7.25	4.53	189.30
6 → 5	661067.277	41.11	7.15	4.30	188.07
7 → 6	771184.125	38.21	6.89	3.50	142.16
8 → 7	881272.808	30.81	6.89	3.23	106.03
9 → 8	991329.305	24.26	7.54	4.50	116.19
10 → 9	1101349.597	16.05	6.86	3.39	57.92
11 → 10	1211329.661	8.04	6.30	3.36	28.72
				Total flux:	828.39

$C^{17}O$

Transition J	Frequency MHz	T_{mb} (K)	V_{lsr} (km s^{-1})	ΔV_{FWHM} (km s^{-1})	$\int T_{mb}dV$ (K km s^{-1})
5 → 4	561713.006	3.83	6.54	4.11	16.77
6 → 5	674009.484	3.07	6.65	3.56	11.62
7 → 6	786282.9^{b}	–	–	–	–
8 → 7	898523.384	1.30	6.66	2.97	4.11
9 → 8	1010731.409	0.72	6.91	5.04	3.87
10 → 9	1122902.893	0.50	6.82	2.73	1.45
				Total flux:	37.82

$C^{18}O$

Transition J	Frequency MHz	T_{mb} (K)	V_{lsr} (km s^{-1})	ΔV_{FWHM} (km s^{-1})	$\int T_{mb}dV$ (K km s^{-1})
5 → 4	548831.115	10.72	6.94	3.97	45.34
6 → 5	658553.653	10.15	6.83	4.12	44.56
7 → 6	768252.152	8.07	6.78	3.21	27.60
8 → 7	877922.544	5.11	6.80	3.03	16.47
9 → 8	987559.089	2.99	7.39	4.41	14.02
10 → 9	1097163.801	2.01	6.75	3.21	6.85
				Total flux:	154.84

$CS, v = 0$

	Transition J	Frequency MHz	T_{mb} (K)	V_{lsr} (km s^{-1})	ΔV_{FWHM} (km s^{-1})	$\int T_{mb}dV$ (K km s^{-1})
Main	$10 \rightarrow 9$	489750.853	5.65	7.04	4.37	26.27
Wing	$10 \rightarrow 9$	489750.921	0.40	7.00	14.00	5.90
Main	$11 \rightarrow 10$	538688.843	4.20	7.09	4.64	20.72
Wing	$11 \rightarrow 10$	538688.919	0.35	7.04	14.62	5.44
Main	$12 \rightarrow 11$	587616.406	2.80	7.04	4.92	14.66
Wing	$12 \rightarrow 11$	587619.039	0.22	5.70	16.67	3.85
Main	$13 \rightarrow 12$	636532.245	1.30	7.10	5.11	7.08
Wing	$13 \rightarrow 12$	636531.412	0.37	7.49	15.00	5.98
Main	$14 \rightarrow 13$	685435.930	1.04	7.00	4.89	5.42
Wing	$14 \rightarrow 13$	685437.573	0.35	6.28	13.00	4.85
Main	$15 \rightarrow 14$	734325.784	0.52	7.06	3.89	2.16
Wing	$15 \rightarrow 14$	734327.696	0.55	6.28	13.00	7.56
Main	$16 \rightarrow 15$	783201.359	0.50	7.06	5.97	3.18
Wing	$16 \rightarrow 15$	783203.399	0.16	6.28	13.00	2.15
Main	$17 \rightarrow 16$	832061.553	0.37	7.06	5.45	2.16
Wing	$17 \rightarrow 16$	832063.720	0.12	6.28	12.29	1.60
Main	$18 \rightarrow 17$	880903.853	0.43	7.59	5.00	2.26
Wing	$18 \rightarrow 17$	–	–	–	–	–
Main	$19 \rightarrow 18$	929733.808	0.35	6.46	5.00	1.87
Wing	$19 \rightarrow 18$	–	–	–	–	–
					Total flux:	123.11

^{13}CS

	Transition J	Frequency MHz	T_{mb} (K)	V_{lsr} (km s^{-1})	ΔV_{FWHM} (km s^{-1})	$\int T_{mb}dV$ (K km s^{-1})
	$11 \rightarrow 10$	508535.834	0.13	6.35	3.46	0.49
	$12 \rightarrow 11$	554727.670	0.11	5.97	4.00	0.46
	$13 \rightarrow 12$	600905.634	0.09	7.42	2.72	0.25
					Total flux:	1.20

$C^{34}S$

	Transition J	Frequency MHz	T_{mb} (K)	V_{lsr} (km s^{-1})	ΔV_{FWHM} (km s^{-1})	$\int T_{mb}dV$ (K km s^{-1})
	$10 \rightarrow 9$	481916.666	0.40	6.47	5.84	2.51
	$11 \rightarrow 10$	530071.145	0.24	7.23	5.44	1.37
	$12 \rightarrow 11$	578215.878	0.20	7.62	5.98	1.26
	$13 \rightarrow 12$	626351.092	0.20	7.14	5.84	1.24
					Total flux:	6.38

C^+

Transition $^{2s+1}L_{\|L+S\|}$	Frequency MHz	T_{mb} (K)	V_{lsr} (km s^{-1})	ΔV_{FWHM} (km s^{-1})	$\int T_{mb}dV$ (K km s^{-1})
$^2P_{3/2} \rightarrow ^2 P_{1/2}$	1900527.547	84.44	8.48	3.44	309.43
				Total flux:	309.43

$C{-}atom$

Transition $^{2s+1}L_{\|L+S\|}$	Frequency MHz	T_{mb} (K)	V_{lsr} (km s^{-1})	ΔV_{FWHM} (km s^{-1})	$\int T_{mb}dV$ (K km s^{-1})
$^3P_1 \rightarrow ^3 P_0$	492161.278	6.31	6.62	2.81	18.86
$^3P_2 \rightarrow ^3 P_1$	809342.914	9.74	6.65	2.69	27.94
				Total flux:	46.80

CCH

Transition N_{J,F_1}	Frequency MHz	T_{mb} (K)	V_{lsr} (km s^{-1})	ΔV_{FWHM} (km s^{-1})	$\int T_{mb}dV$ (K km s^{-1})
$6_{6.5,7} \rightarrow 5_{5.5,6}$	523972.067	2.88	6.72	4.08	12.48
$6_{5.56} \rightarrow 5_{4.5,5}$	524034.397	2.35	6.72	4.24	10.59
$7_{7.5,8} \rightarrow 6_{6.5,7}$	611267.056	1.55	7.07	4.49	7.41
$7_{6.5,6} \rightarrow 6_{5.5,5}$	611329.636	1.24	7.04	4.80	6.35
$8_{8.5,9} \rightarrow 7_{7.5,8}$	698544.470	0.79	7.13	5.24	4.39
$8_{7.5,7} \rightarrow 7_{6.5,6}$	698607.427	0.73	7.01	4.61	3.56
$9_{9.5,10} \rightarrow 8_{8.5,9}$	785801.643	0.43	7.17	5.11	2.36
$9_{8.5,8} \rightarrow 8_{7.5,7}$	785864.192	0.28	7.30	5.09	1.50
				Total flux:	48.64

CH

Transition N_{K,J,F_1}	Frequency MHz	T_{mb} (K)	V_{lsr} (km s^{-1})	ΔV_{FWHM} (km s^{-1})	$\int T_{mb}dV$ (K km s^{-1})
$1_{1,1.5,1} \rightarrow 1_{-1,0.5,1}$	532721.727	3.15	8.24	4.24	14.21
$1_{1,1.5,1} \rightarrow 1_{-1,0.5,0}$	532791.464	1.24	8.04	4.14	5.46
$1_{-1,1.5,2} \rightarrow 1_{1,0.5,1}$	536759.116	2.79	8.13	4.01	11.89
$1_{-1,1.5,1} \rightarrow 1_{1,0.5,1}$	536779.687	0.71	8.27	3.70	2.81
$1_{-1,1.5,1} \rightarrow 1_{1,0.5,0}$	536793.543	1.21	8.19	4.03	5.20
				Total flux:	39.57

CH^+

Transition J	Frequency MHz	T_{mb} (K)	V_{lsr} (km s^{-1})	ΔV_{FWHM} (km s^{-1})	$\int T_{mb}dV$ (K km s^{-1})
1 → 0	835135.839	4.11	7.60	4.41	19.27
				Total flux:	19.27

$CN, v = 0$

Transition N_{J,F_1}	Frequency MHz	T_{mb} (K)	V_{lsr} (km s^{-1})	ΔV_{FWHM} (km s^{-1})	$\int T_{mb} dV$ (K km s^{-1})
$5_{4.5,5.5} \rightarrow 4_{3.5,4.5}$	566729.480	9.26	7.23	4.98	1.75
$5_{5.5,5.5} \rightarrow 4_{4.5,4.5}$	566946.096	10.82	7.37	4.69	2.17
$6_{5.5,6.5} \rightarrow 5_{4.5,5.5}$	680046.287	4.04	7.25	5.09	0.75
$6_{6.5,6.5} \rightarrow 5_{5.5,5.5}$	680263.145	5.31	7.33	5.17	0.97
$7_{6.5,7.5} \rightarrow 6_{5.5,6.5}$	793337.051	2.86	6.65	6.10	0.44
$7_{7.5,7.5} \rightarrow 6_{6.5,6.5}$	793552.119	2.67	7.44	7.68	0.33
				Total flux:	6.41

$DCN, v = 0$

Transition N_k	Frequency MHz	T_{mb} (K)	V_{lsr} (km s^{-1})	ΔV_{FWHM} (km s^{-1})	$\int T_{mb} dV$ (K km s^{-1})
$7_0 \rightarrow 6_0$	506825.63	0.25	6.78	5.45	1.47
$8_0 \rightarrow 7_0$	579199.24	0.09	7.99	5.58	0.52
				Total flux:	1.99

DCO^+

Transition J	Frequency MHz	T_{mb} (K)	V_{lsr} (km s^{-1})	ΔV_{FWHM} (km s^{-1})	$\int T_{mb} dV$ (K km s^{-1})
$7 \rightarrow 6$	504200.27	0.21	6.96	3.81	0.85
$8 \rightarrow 7$	576205.0^b	–	–	–	–
$9 \rightarrow 8$	648195.15	0.24	6.07	1.54	0.39
				Total flux:	1.24

HCl

Transition N_J	Frequency MHz	T_{mb} (K)	V_{lsr} (km s^{-1})	ΔV_{FWHM} (km s^{-1})	$\int T_{mb} dV$ (K km s^{-1})
$1_{1.5} \rightarrow 0_{1.5}$	625900.033	2.69	7.75	4.35	12.45
$1_{2.5} \rightarrow 0_{1.5}$	625916.496	3.49	8.08	4.81	17.89
$1_{0.5} \rightarrow 0_{1.5}$	625929.733	1.79	8.09	5.01	9.56
				Total flux:	39.90

$H^{37}Cl$

Transition N_J	Frequency MHz	T_{mb} (K)	V_{lsr} (km s^{-1})	ΔV_{FWHM} (km s^{-1})	$\int T_{mb} dV$ (K km s^{-1})
$1_{1.5} \rightarrow 0_{1.5}$	624962.479	1.20	7.91	4.72	6.03
$1_{2.5} \rightarrow 0_{1.5}$	624975.926	1.74	7.91	4.72	8.76
$1_{0.5} \rightarrow 0_{1.5}$	624986.439	1.04	7.91	4.72	5.23
				Total flux:	20.02

$H_2^{18}O$

Transition $J_{K_{-1},K_{+1},v}$	Frequency MHz	T_{mb} (K)	V_{lsr} (km s^{-1})	ΔV_{FWHM} (km s^{-1})	$\int T_{mb}dV$ (K km s^{-1})
$1_{1,0,0} \rightarrow 1_{0,1,0}$	547676.359	0.32	7.04	5.55	1.88
				Total flux:	1.88

H_2CS

Transition J_{K_a,K_c}	Frequency MHz	T_{mb} (K)	V_{lsr} (km s^{-1})	ΔV_{FWHM} (km s^{-1})	$\int T_{mb}dV$ (K km s^{-1})
$14_{1,13} \rightarrow 13_{1,12}$	487664.025	0.27	6.57	4.39	1.27
$15_{1,15} \rightarrow 14_{1,14}$	506771.495	0.28	6.67	5.34	1.60
$15_{0,15} \rightarrow 14_{0,14}$	513361.943	0.18	5.70	6.54	1.25
$15_{2,13} \rightarrow 14_{2,12}$	516336.1[b]	–	–	–	–
$15_{1,14} \rightarrow 14_{1,13}$	522403.631	0.19	6.72	4.82	0.96
$16_{1,16} \rightarrow 15_{1,15}$	540465.306	0.17	6.17	4.15	0.76
$16_{1,15} \rightarrow 15_{1,14}$	557124.939	0.15	5.98	3.84	0.61
$17_{1,17} \rightarrow 16_{1,16}$	574140.119	0.12	6.78	5.11	0.64
$17_{1,16} \rightarrow 16_{1,15}$	591821.645	0.11	6.91	3.61	0.44
$18_{1,18} \rightarrow 17_{1,17}$	607798.207	0.18	6.79	5.20	0.98
				Total flux:	8.51

$o{-}NH_3$

	Transition $N_{K,v}$	Frequency MHz	T_{mb} (K)	V_{lsr} (km s^{-1})	ΔV_{FWHM} (km s^{-1})	$\int T_{mb}dV$ (K km s^{-1})
Main	$1_{0,0} \rightarrow 0_{0,1}$	572498.197	4.33	6.98	5.80	26.70
Wing	$1_{0,0} \rightarrow 0_{0,1}$	572494.299	0.17	9.02	21.68	3.93
					Total flux:	30.63

HCO^+

Transition J	Frequency MHz	T_{mb} (K)	V_{lsr} (km s^{-1})	ΔV_{FWHM} (km s^{-1})	$\int T_{mb}dV$ (K km s^{-1})
6 → 5	535061.307	19.61	7.15	5.51	115.11
7 → 6	624208.401	18.07	6.98	5.29	101.73
8 → 7	713341.513	13.53	6.88	5.29	76.17
9 → 8	802458.758	9.70	6.79	5.17	53.38
10 → 9	891558.144	7.44	6.71	4.98	39.40
11 → 10	980636.969	5.79	6.86	5.07	31.21
12 → 11	1069696.072	3.68	6.39	4.40	17.23
13 → 12	1158730.025	2.48	6.28	4.94	13.05
				Total flux:	447.28

$H^{13}CO^{+}$

Transition J	Frequency MHz	T_{mb} (K)	V_{lsr} (km s^{-1})	ΔV_{FWHM} (km s^{-1})	$\int T_{mb}dV$ (K km s^{-1})
$6 \rightarrow 5$	520460.323	1.42	6.75	3.81	5.74
$7 \rightarrow 6$	607175.527	0.89	6.57	3.69	3.49
$8 \rightarrow 7$	693877.574	0.53	6.43	3.78	2.15
$9 \rightarrow 8$	780563.188	0.35	6.86	3.81	1.43
				Total flux:	12.81

$HC^{18}O^{+}$

Transition J	Frequency MHz	T_{mb} (K)	V_{lsr} (km s^{-1})	ΔV_{FWHM} (km s^{-1})	$\int T_{mb}dV$ (K km s^{-1})
$6 \rightarrow 5$	510910.351	0.15	6.58	3.56	0.58
				Total flux:	0.58

HDO

Transition $J_{K_{-1},K_{+1}}$	Frequency MHz	T_{mb} (K)	V_{lsr} (km s^{-1})	ΔV_{FWHM} (km s^{-1})	$\int T_{mb}dV$ (K km s^{-1})
$2_{0,2} \rightarrow 1_{1,1}$	490596.998	0.24	6.78	3.91	0.98
$1_{1,0} \rightarrow 1_{1,1}$	509293.663	0.36	6.27	3.43	1.30
$2_{1,1} \rightarrow 2_{0,2}$	599927.693	0.28	6.51	2.89	0.85
				Total flux:	3.13

HCN

	Transition J	Frequency MHz	T_{mb} (K)	V_{lsr} (km s^{-1})	ΔV_{FWHM} (km s^{-1})	$\int T_{mb}dV$ (K km s^{-1})
Main	$6 \rightarrow 5$	531716.095	9.29	7.14	5.33	52.72
Wing	$6 \rightarrow 5$	531718.599	0.98	5.73	20.07	20.94
Main	$7 \rightarrow 6$	620303.703	6.62	7.14	5.31	37.38
Wing	$7 \rightarrow 6$	620305.685	0.92	6.19	20.64	20.27
Main	$8 \rightarrow 7$	708876.272	3.34	7.31	5.30	18.86
Wing	$8 \rightarrow 7$	708878.306	0.98	6.45	20.07	20.94
Main	$9 \rightarrow 8$	797432.272	1.54	7.37	5.84	9.58
Wing	$9 \rightarrow 8$	797434.998	0.63	6.35	19.48	13.03
Main	$10 \rightarrow 9$	885969.747	0.78	7.32	5.63	4.70
Wing	$10 \rightarrow 9$	885973.426	0.79	6.08	14.56	12.29
Main	$11 \rightarrow 10$	974486.550	0.78	7.20	4.59	3.81
Wing	$11 \rightarrow 10$	–	–	–	–	–
Main	$13 \rightarrow 12$	1151448.540	0.26	7.14	5.35	1.46
Wing	$13 \rightarrow 12$	1151453.962	0.36	5.73	18.90	7.28
Main	$12 \rightarrow 11$	1062986.194	0.96	5.45	8.17	8.33
Main	$13 \rightarrow 12$	1151453.992	0.69	5.72	7.02	5.14
					Total flux:	236.73

$H^{13}CN$

Transition J	Frequency MHz	T_{mb} (K)	V_{lsr} (km s^{-1})	ΔV_{FWHM} (km s^{-1})	$\int T_{mb}dV$ (K km s^{-1})
$6 \rightarrow 5$	517969.281	0.49	7.31	5.35	2.82
$7 \rightarrow 6$	604266.220	0.27	7.84	7.90	2.27
$8 \rightarrow 7$	690552.867	0.19	6.66	10.59	2.15
				Total flux:	7.24

HNC

Transition J_{K_a,K_c}	Frequency MHz	T_{mb} (K)	V_{lsr} (km s^{-1})	ΔV_{FWHM} (km s^{-1})	$\int T_{mb}dV$ (K km s^{-1})
$6_{0,0} \rightarrow 5_{0,0}$	543897.757	1.57	6.89	4.07	6.79
$7_{0,0} \rightarrow 6_{0,0}$	634510.405	0.59	7.20	4.75	2.97
$8_{0,0} \rightarrow 7_{0,0}$	725106.533	0.34	7.33	4.80	1.76
				Total flux:	11.52

N_2H^+

Transition J	Frequency MHz	T_{mb} (K)	V_{lsr} (km s^{-1})	ΔV_{FWHM} (km s^{-1})	$\int T_{mb}dV$ (K km s^{-1})
$6 \rightarrow 5$	558967.762	4.47	6.33	2.48	11.79
$7 \rightarrow 6$	652097.225	3.67	6.24	2.27	8.87
$8 \rightarrow 7$	745211.797	2.23	6.22	2.13	5.04
$9 \rightarrow 8$	838309.704	1.14	6.14	2.11	2.57
$10 \rightarrow 9$	931388.749	0.58	6.03	2.71	1.68
				Total flux:	29.95

NO

Transition $N_{\Lambda F_1 F_2}$	Frequency MHz	T_{mb} (K)	V_{lsr} (km s^{-1})	ΔV_{FWHM} (km s^{-1})	$\int T_{mb}dV$ (K km s^{-1})
$6_{-1,5.5,4.5} \rightarrow 5_{-1,4.5,3.5}$	549551.072	0.13	7.28	3.87	0.54
$6_{-1,5.5,5.5} \rightarrow 5_{1,4.5,4.5}$	551187.545	0.34	6.89	3.87	1.38
$--$	551230.900	–	–	–	–
$6_{1,5.5,4.5} \rightarrow 5_{-1,4.5,3.5}$	551533.179	0.34	7.44	4.29	1.56
$6_{1,6.5,6.5} \rightarrow 6_{-1,5.5,5.5}$	651432.948	0.45	6.89	4.97	2.39
$6_{-1,6.5,5.5} \rightarrow 6_{1,5.5,4.5}$	651772.994	0.43	6.99	3.82	1.75
				Total flux:	7.62

CO^+

Transition N_J	Frequency MHz	T_{mb} (K)	V_{lsr} (km s^{-1})	ΔV_{FWHM} (km s^{-1})	$\int T_{mb}dV$ (K km s^{-1})
$5_{5.5} \rightarrow 4_{4.5}$	589869.200	0.12	8.51	3.29	0.43
				Total flux:	0.43

SiN

Transition	Frequency	T_{mb}	V_{lsr}	ΔV_{FWHM}	$\int T_{mb}dV$
N_{JF_1}	MHz	(K)	(km s^{-1})	(km s^{-1})	(K km s^{-1})
$13_{13.5,12.5} \rightarrow 12_{12.5,11.5}$	567458.911	0.24	9.99	8.13	2.07
				Total flux:	2.07

$o{-}H_2CO$

Transition	Frequency	T_{mb}	V_{lsr}	ΔV_{FWHM}	$\int T_{mb}dV$
J_{K_a,K_c}	MHz	(K)	(km s^{-1})	(km s^{-1})	(K km s^{-1})
$7_{1,7} \rightarrow 6_{1,6}$	491968.656	3.96	6.83	4.45	18.75
$7_{5,3} \rightarrow 6_{5,2}$	509565.4[b]	–	–	–	–
$7_{3,5} \rightarrow 6_{3,4}$	510156.094	1.08	6.79	5.16	5.92
$7_{3,4} \rightarrow 6_{3,3}$	510238.147	1.08	6.82	4.91	5.63
$7_{1,6} \rightarrow 6_{1,5}$	525666.249	3.19	6.76	4.59	15.59
$8_{1,8} \rightarrow 7_{1,7}$	561899.669	3.36	6.81	4.52	16.18
$8_{5,3} \rightarrow 7_{5,2}$	582382.423	0.27	6.82	5.76	1.63
$8_{3,6} \rightarrow 7_{3,5}$	583144.943	0.73	6.83	5.34	4.16
$8_{3,5} \rightarrow 7_{3,4}$	583308.771	0.70	6.89	4.97	3.72
$8_{1,7} \rightarrow 7_{1,6}$	600331.129	2.16	6.72	4.75	10.91
$9_{1,9} \rightarrow 8_{1,8}$	631703.503	2.03	6.67	4.70	10.14
$9_{1,9} \rightarrow 8_{1,8}$	631703.379	1.61	6.73	4.68	8.03
$9_{5,5} \rightarrow 8_{5,4}$	655213.921	0.23	6.17	5.54	1.37
$9_{3,7} \rightarrow 8_{3,6}$	656166.562	0.78	6.15	6.15	5.10
$9_{3,6} \rightarrow 8_{3,5}$	656465.165	0.59	6.73	5.01	3.16
$9_{1,8} \rightarrow 8_{1,7}$	674810.418	1.37	6.72	4.75	6.92
$10_{3,8} \rightarrow 9_{3,7}$	729213.492	0.49	6.61	4.82	2.54
$10_{3,7} \rightarrow 9_{3,6}$	729726.341	0.43	6.45	5.65	2.59
$10_{1,9} \rightarrow 9_{1,8}$	749073.051	1.01	6.56	5.18	5.58
$11_{1,11} \rightarrow 10_{1,10}$	770895.493	0.96	7.22	6.17	6.30
$11_{3,8} \rightarrow 10_{3,7}$	803113.450	0.36	6.32	6.25	2.41
$11_{1,10} \rightarrow 10_{1,9}$	823084.804	0.65	6.26	5.61	3.88
$12_{1,12} \rightarrow 11_{1,11}$	840277.353	0.57	6.40	5.46	3.29
$12_{5,7} \rightarrow 11_{5,6}$	873777.678	0.13	6.22	3.62	0.51
$12_{3,10} \rightarrow 11_{3,9}$	875367.401	0.21	6.58	7.10	1.60
$12_{3,9} \rightarrow 11_{3,8}$	876651.037	0.20	6.35	9.75	2.03
$12_{1,11} \rightarrow 11_{1,10}$	896807.849	0.36	6.10	5.81	2.24
$13_{1,13} \rightarrow 12_{1,12}$	909509.667	0.38	6.34	5.09	2.04
				Total flux:	152.22

$p\text{−}H_2CO$

Transition J_{K_a,K_c}	Frequency MHz	T_{mb} (K)	V_{lsr} (km s^{-1})	ΔV_{FWHM} (km s^{-1})	$\int T_{mb}dV$ (K km s^{-1})
$7_{0,7} \rightarrow 6_{0,6}$	505834.190	2.15	6.72	4.24	9.73
$7_{2,6} \rightarrow 6_{2,5}$	509146.870	0.99	6.63	4.13	4.34
$7_{4,4} \rightarrow 6_{4,3}$	509830.540	0.29	6.42	5.15	1.60
$7_{2,5} \rightarrow 6_{2,4}$	513077.060	0.87	6.59	4.69	4.35
$8_{0,8} \rightarrow 7_{0,7}$	576709.070	1.34	6.61	4.35	6.20
$8_{2,7} \rightarrow 7_{2,6}$	581612.440	0.59	6.70	4.28	2.71
$8_{4,5} \rightarrow 7_{4,4}$	582724.460	0.27	6.23	5.16	1.46
$8_{2,6} \rightarrow 7_{2,5}$	587454.360	0.57	6.64	4.78	2.88
$9_{0,9} \rightarrow 8_{0,8}$	647082.630	1.06	6.58	4.79	5.42
$9_{2,8} \rightarrow 8_{2,7}$	653971.320	0.49	6.47	4.81	2.50
$9_{4,6} \rightarrow 8_{4,5}$	655640.550	0.20	6.71	5.82	1.24
$9_{2,7} \rightarrow 8_{2,6}$	662210.020	0.51	6.61	4.73	2.55
$10_{0,10} \rightarrow 9_{0,9}$	716938.720	0.52	6.85	5.52	3.03
$10_{2,9} \rightarrow 9_{2,8}$	726209.570	0.44	6.45	5.50	2.58
$10_{4,6} \rightarrow 9_{4,5}$	728591.340	0.17	7.09	5.79	1.08
$10_{2,8} \rightarrow 9_{2,7}$	737342.600	0.39	7.03	6.11	2.55
$11_{2,9} \rightarrow 10_{2,8}$	812829.170	0.19	7.82	5.95	1.22
				Total flux:	55.44

$o\text{−}H_2S$

Transition $J_{\Omega,\Lambda}$	Frequency MHz	T_{mb} (K)	V_{lsr} (km s^{-1})	ΔV_{FWHM} (km s^{-1})	$\int T_{mb}dV$ (K km s^{-1})
$2_{2,1} \rightarrow 2_{1,2}$	505565.219	1.96	7.01	4.95	10.34
$2_{1,2} \rightarrow 1_{0,1}$	736034.210	6.03	6.95	4.56	29.28
$5_{2,3} \rightarrow 5_{1,4}$	993107.064	2.31	5.41	5.74	14.11
$2_{2,1} \rightarrow 1_{1,0}$	1072837.042	1.03	6.86	5.72	6.27
				Total flux:	60.00

$p\text{−}H_2S$

Transition $J_{\Omega,\Lambda}$	Frequency MHz	T_{mb} (K)	V_{lsr} (km s^{-1})	ΔV_{FWHM} (km s^{-1})	$\int T_{mb}dV$ (K km s^{-1})
$2_{0,2} \rightarrow 1_{1,1}$	687303.344	3.11	7.05	4.79	15.86
$3_{2,2} \rightarrow 3_{1,3}$	747301.595	0.32	7.12	4.83	1.67
$3_{1,3} \rightarrow 2_{0,2}$	1002777.304	1.01	7.42	5.15	5.52
				Total flux:	23.05

$H_2^{33}S$

Transition $N_{K_a,K_c,J}$	Frequency MHz	T_{mb} (K)	V_{lsr} (km s^{-1})	ΔV_{FWHM} (km s^{-1})	$\int T_{mb}dV$ (K km s^{-1})
$2_{0,2,2.5} \rightarrow 1_{1,1,2.5}$	687152.939	0.17	6.97	4.24	0.77
$3_{1,2,4.5} \rightarrow 3_{0,3,3.5}$	708473.5^b	–	–	–	–
				Total flux:	0.77

$H_2^{34}S$

Transition N_{K_a,K_c}	Frequency MHz	T_{mb} (K)	V_{lsr} (km s^{-1})	ΔV_{FWHM} (km s^{-1})	$\int T_{mb}dV$ (K km s^{-1})
$2_{2,1} \rightarrow 2_{1,2}$	503015.029	0.09	6.20	4.39	0.41
$2_{1,2} \rightarrow 1_{0,1}$	734269.666	0.47	6.60	5.34	2.66
				Total flux:	3.07

SH^+

Transition N_{J,F_1}	Frequency MHz	T_{mb} (K)	V_{lsr} (km s^{-1})	ΔV_{FWHM} (km s^{-1})	$\int T_{mb}dV$ (K km s^{-1})
$1_{2,1.5} \rightarrow 0_{1,0.5}$	526036.200	0.16	8.44	0.86	0.14
$1_{2,2.5} \rightarrow 0_{1,1.5}$	526045.440	0.19	8.43	1.40	0.28
				Total flux:	0.42

SiO

Transition J_K	Frequency MHz	T_{mb} (K)	V_{lsr} (km s^{-1})	ΔV_{FWHM} (km s^{-1})	$\int T_{mb}dV$ (K km s^{-1})
$12_0 \rightarrow 11_0$	520879.520	0.13	7.91	17.99	2.53
$13_0 \rightarrow 12_0$	564249.440	0.11	6.77	18.00	2.06
				Total flux:	4.59

SO

Transition N_J	Frequency MHz	T_{mb} (K)	V_{lsr} (km s^{-1})	ΔV_{FWHM} (km s^{-1})	$\int T_{mb} dV$ (K km s^{-1})
$4_3 \rightarrow 1_2$	504676.684	0.16	6.76	3.79	0.66
$12_{11} \rightarrow 11_{10}$	514853.391	0.86	7.21	6.71	6.14
$12_{12} \rightarrow 11_{11}$	516335.628	0.82	7.12	7.60	6.66
$12_{13} \rightarrow 11_{12}$	517354.088	1.10	7.26	6.38	7.50
$13_{12} \rightarrow 12_{11}$	558087.150	0.51	7.27	5.89	3.18
$13_{13} \rightarrow 12_{12}$	559319.679	0.50	7.02	6.60	3.54
$13_{14} \rightarrow 12_{13}$	560178.460	0.59	7.10	5.69	3.58
$14_{13} \rightarrow 13_{12}$	601257.878	0.48	7.29	9.61	4.91
$14_{14} \rightarrow 13_{13}$	602291.952	0.44	7.53	9.00	4.22
$14_{15} \rightarrow 13_{14}$	603021.650	0.52	7.00	8.15	4.55
$5_4 \rightarrow 2_3$	611551.861	0.14	7.27	3.67	0.53
$15_{14} \rightarrow 14_{13}$	644377.526	0.45	7.65	9.00	4.34
$15_{15} \rightarrow 14_{14}$	645253.673	0.39	7.59	9.00	3.75
$15_{16} \rightarrow 14_{15}$	645874.952	0.45	7.45	10.49	5.06
$16_{15} \rightarrow 15_{14}$	687457.555	0.34	7.06	12.57	4.53
$16_{16} \rightarrow 15_{15}$	688204.386	0.32	7.11	10.49	3.57
$16_{17}\| \rightarrow 15_{16}$	688733.813	0.34	7.82	14.92	5.38
$17_{16} \rightarrow 16_{15}$	730500.255	0.37	7.22	7.47	2.95
$17_{17} \rightarrow 16_{16}$	731135.604	0.25	9.34	14.13	3.69
$17_{18} \rightarrow 16_{17}$	731597.279	0.29	6.67	14.21	4.45
$18_{18} \rightarrow 17_{17}$	774063.444	0.25	7.27	11.28	3.01
$18_{19} \rightarrow 17_{18}$	774454.800	0.22	6.95	14.06	3.26
$19_{18} \rightarrow 18_{17}$	816492.540	0.15	7.97	11.11	1.72
$19_{19} \rightarrow 18_{18}$	816971.234	0.20	7.40	11.00	2.34
				Total flux:	93.52

SO_2

Transition N_{K_a,K_c}	Frequency MHz	T_{mb} (K)	V_{lsr} (km s^{-1})	ΔV_{FWHM} (km s^{-1})	$\int T_{mb}dV$ (K km s^{-1})
$13_{3,11} \rightarrow 12_{2,10}$	484270.336	0.25	7.34	4.46	1.20
$7_{4,4} \rightarrow 6_{3,3}$	491933.632	0.17	7.66	5.82	1.07
$12_{3,9} \rightarrow 11_{2,10}$	494779.215	0.24	7.31	4.21	1.06
$15_{3,13} \rightarrow 14_{2,12}$	508708.907	0.16	7.54	4.32	0.76
$8_{4,4} \rightarrow 7_{3,5}$	511088.6	0.20	7.65	6.16	1.30
$9_{4,6} \rightarrow 8_{3,5}$	529974.424	0.16	7.29	7.11	1.24
$10_{4,6} \rightarrow 9_{3,7}$	549303.355	0.16	7.01	5.30	0.89
$11_{4,8} \rightarrow 10_{3,7}$	567593.3	0.13	6.70	7.17	1.01
$6_{5,1} \rightarrow 5_{4,2}$	574807.283	0.13	7.05	6.06	0.87
$12_{4,8} \rightarrow 11_{3,9}$	587567.878	0.16	7.24	7.31	1.28
$13_{4,10} \rightarrow 12_{3,9}$	604367.596	0.16	6.92	6.21	1.07
$8_{5,3} \rightarrow 7_{4,4}$	613076.701	0.14	6.78	5.96	0.91
$14_{4,10} \rightarrow 13_{3,11}$	626085.781	0.10	7.74	5.55	0.61
$9_{5,5} \rightarrow 8_{4,4}$	632195.465	0.09	6.01	10.83	1.02
$10_{5,5} \rightarrow 9_{4,6}$	651299.092	0.17	7.38	6.71	1.24
$16_{4,12} \rightarrow 15_{3,13}$	665245.959	0.18	7.40	4.77	0.90
$17_{4,14} \rightarrow 16_{3,13}$	672567.493	0.18	5.67	5.19	0.98
				Total flux:	17.41

$A{-}CH_3OH$

Transition $J_{K,\,v^{\pi}}$	Frequency MHz	T_{mb} (K)	V_{lsr} (km s^{-1})	ΔV_{FWHM} (km s^{-1})	$\int T_{mb}dV$ (K km s^{-1})
$3_{2,0^+} \rightarrow 3_{1,0^-}$	480269.825	0.92	6.65	3.67	3.59
$2_{2,0^+} \rightarrow 2_{1,0^-}$	481505.550	0.88	6.14	3.30	3.09
$10_{1,1^-} \rightarrow 9_{1,1^-}$	482668.407	0.16	6.00	6.06	1.03
$10_{0,0^+} \rightarrow 9_{0,0^+}$	483141.473	2.01	6.55	4.26	9.12
$10_{2,0^-} \rightarrow 9_{2,0^-}$	483388.951	0.34	6.76	4.94	1.81
$10_{3,0^+} \rightarrow 9_{3,0^+}$	483553.399	0.32	5.51	6.36	2.19
$10_{3,0^-} \rightarrow 9_{3,0^-}$	483566.433	0.38	6.48	3.90	1.56
$10_{2,0^+} \rightarrow 9_{2,0^+}$	483762.050	0.31	6.58	5.67	1.84
$2_{2,0^-} \rightarrow 2_{1,0^+}$	484005.485	0.89	6.49	4.18	3.98
$3_{2,0^-} \rightarrow 3_{1,0^+}$	485263.938	1.09	6.55	3.97	4.59
$4_{2,0^-} \rightarrow 4_{1,0^+}$	486941.551	1.13	6.51	4.08	4.91
$10_{1,0^-} \rightarrow 9_{1,0^-}$	487532.703	0.82	6.49	4.41	3.86
$5_{2,0^-} \rightarrow 5_{1,0^+}$	489037.528	1.05	6.56	4.13	4.61
$6_{2,0^-} \rightarrow 6_{1,0^+}$	491551.865	0.89	6.30	4.05	3.84
$4_{1,0^+} \rightarrow 3_{0,0^+}$	492279.271	2.57	6.65	4.22	11.54
$5_{3,0^+} \rightarrow 4_{2,0^+}$	493699.963	1.72	6.48	3.65	6.68
$5_{3,0^-} \rightarrow 4_{2,0^-}$	493734.646	1.79	6.42	3.65	6.95
$7_{2,0^-} \rightarrow 7_{1,0^+}$	494482.354	0.77	6.52	4.25	3.48
$8_{2,0^-} \rightarrow 8_{1,0^+}$	497829.067	0.57	6.43	4.32	2.60
$9_{2,0^-} \rightarrow 9_{1,0^+}$	501589.386	0.47	6.70	4.03	2.03
$10_{2,0^-} \rightarrow 10_{1,0^+}$	505762.882	0.37	6.43	4.47	1.76
$11_{2,0^-} \rightarrow 11_{1,0^+}$	510345.789	0.27	6.41	4.70	1.34
$16_{0,0^+} \rightarrow 15_{1,0^+}$	515170.913	0.27	6.61	4.90	1.40
$12_{2,0^-} \rightarrow 12_{1,0^+}$	515333.672	0.18	7.53	5.64	1.09
$13_{2,0^-} \rightarrow 13_{1,0^+}$	520728.657	0.11	6.49	6.17	0.72
$11_{1,0^+} \rightarrow 10_{1,0^+}$	527054.339	0.52	6.52	3.93	2.16
$11_{0,0^+} \rightarrow 10_{0,0^+}$	531320.091	1.56	6.57	4.28	7.12
$11_{2,0^-} \rightarrow 10_{2,0^-}$	531636.157	0.30	7.12	6.89	2.17
$11_{4,0^-} \rightarrow 10_{4,0^-}$	531869.531	0.47	7.47	6.17	3.08
$11_{3,0^-} \rightarrow 10_{3,0^-}$	531893.144	0.37	6.85	4.81	1.89
$11_{2,0^+} \rightarrow 10_{2,0^+}$	532133.994	0.35	6.21	4.07	1.49
$11_{1,0^-} \rightarrow 10_{1,0^-}$	536192.131	0.79	6.40	3.71	3.10
$5_{1,0^+} \rightarrow 4_{0,0^+}$	538571.190	2.71	6.65	4.40	12.71
$6_{3,0^+} \rightarrow 5_{2,0^+}$	542002.045	1.60	6.40	3.67	6.24
$6_{3,0^-} \rightarrow 5_{2,0^-}$	542082.941	1.58	6.45	3.70	6.24
$17_{0,0^+} \rightarrow 16_{1,0^+}$	568785.513	0.17	5.93	5.62	1.04
$12_{1,0^+} \rightarrow 11_{1,0^+}$	574869.738	0.42	6.33	4.19	1.88
$2_{2,0^-} \rightarrow 1_{1,0^-}$	579085.750	1.74	6.45	3.70	6.84
$12_{0,0^+} \rightarrow 11_{0,0^+}$	579460.654	1.12	6.46	4.39	5.24
$12_{2,0^-} \rightarrow 11_{2,0^-}$	579858.974	0.22	6.62	5.40	1.25
$2_{2,0^+} \rightarrow 1_{1,0^+}$	579922.265	1.72	6.47	4.11	7.54
$12_{5,0^+} \rightarrow 11_{5,0^+}$	580059.864	0.13	6.17	5.43	0.73

$A{-}CH_3OH$

Transition $J_{K,\,v^\pi}$	Frequency MHz	T_{mb} (K)	V_{lsr} (km s^{-1})	ΔV_{FWHM} (km s^{-1})	$\int T_{mb}dV$ (K km s^{-1})
$12_{3,0^+} \rightarrow 11_{3,0^+}$	580176.813	0.24	6.56	4.16	1.07
$12_{3,0^-} \rightarrow 11_{3,0^-}$	580212.189	0.26	7.30	5.34	1.46
$12_{2,0^+} \rightarrow 11_{2,0^+}$	580503.314	0.25	6.30	4.48	1.20
$6_{1,0^+} \rightarrow 5_{0,0^+}$	584450.718	2.46	6.62	4.30	11.25
$12_{1,0^-} \rightarrow 11_{1,0^-}$	584823.311	0.58	6.56	5.34	3.32
$7_{3,0^+} \rightarrow 6_{2,0^+}$	590278.732	1.37	6.48	3.91	5.69
$7_{3,0^-} \rightarrow 6_{2,0^-}$	590441.532	1.33	6.44	3.79	5.35
$18_{0,0^+} \rightarrow 17_{1,0^+}$	622570.600	0.16	5.95	7.17	1.25
$13_{1,0^+} \rightarrow 12_{1,0^+}$	622660.024	0.39	6.37	4.30	1.79
$3_{2,0^-} \rightarrow 2_{1,0^-}$	626627.336	1.77	6.47	3.86	7.27
$13_{0,0^+} \rightarrow 12_{0,0^+}$	627559.428	0.79	6.52	5.40	4.52
$13_{2,0^-} \rightarrow 12_{2,0^-}$	628052.231	0.24	6.84	5.99	1.55
$13_{3,0^+} \rightarrow 12_{3,0^+}$	628471.507	0.26	6.22	6.34	1.73
$13_{4,0^-} \rightarrow 12_{4,0^-}$	628513.718	0.23	6.26	3.54	0.87
$13_{3,0^-} \rightarrow 12_{3,0^-}$	628524.830	0.25	7.09	5.31	1.40
$13_{2,0^+} \rightarrow 12_{2,0^+}$	628868.084	0.26	7.46	5.09	1.42
$3_{2,0^+} \rightarrow 2_{1,0^+}$	629141.491	1.87	6.46	4.09	8.14
$7_{1,0^+} \rightarrow 6_{0,0^+}$	629922.006	2.12	6.69	4.58	10.36
$13_{1,0^-} \rightarrow 12_{1,0^-}$	633424.483	0.52	6.33	4.90	2.70
$7_{4,0^-} \rightarrow 7_{3,0^+}$	636336.967	0.36	7.22	4.12	1.57
$4_{4,0^-} \rightarrow 4_{3,0^+}$	636422.009	0.69	6.04	2.78	2.03
$3_{2,0^-} \rightarrow 2_{1,0^-}$	626627.672	1.47	6.31	3.99	6.25
$13_{0,0^+} \rightarrow 12_{0,0^+}$	627560.254	0.63	6.12	3.91	2.64
$3_{2,0^+} \rightarrow 2_{1,0^+}$	629141.288	1.25	6.55	4.16	5.52
$7_{1,0^+} \rightarrow 6_{0,0^+}$	629921.684	1.47	6.84	4.97	7.78
$13_{1,0^-} \rightarrow 12_{1,0^-}$	633425.216	0.32	5.98	5.18	1.75
$7_{4,0^-} \rightarrow 7_{3,0^+}$	636335.857	0.39	7.74	4.43	1.84
$6_{4,0^+} \rightarrow 6_{3,0^-}$	636365.902	0.45	6.14	4.44	2.14
$5_{4,0^-} \rightarrow 5_{3,0^+}$	636395.601	0.44	6.14	4.63	2.16
$4_{4,0^+} \rightarrow 4_{3,0^-}$	636420.699	0.34	6.60	3.51	1.25
$8_{3,0^+} \rightarrow 7_{2,0^+}$	638524.781	1.20	6.40	4.41	5.63
$8_{3,0^-} \rightarrow 7_{2,0^-}$	638818.881	1.13	6.50	4.42	5.31
$14_{1,0^+} \rightarrow 13_{1,0^+}$	670424.181	0.29	6.32	6.84	2.08
$4_{2,0^-} \rightarrow 3_{1,0^-}$	673747.183	1.71	6.45	4.22	7.68
$8_{1,0^+} \rightarrow 7_{0,0^+}$	674991.116	1.71	6.75	4.52	8.20
$14_{0,0^+} \rightarrow 13_{0,0^+}$	675613.750	0.63	6.50	5.51	3.72
$14_{2,0^-} \rightarrow 13_{2,0^-}$	676213.813	0.26	7.54	4.22	1.19
$14_{3,0^+} \rightarrow 13_{3,0^+}$	676751.278	0.23	6.20	6.82	1.70
$14_{3,0^-} \rightarrow 13_{3,0^-}$	676829.066	0.30	7.22	6.58	2.13
$4_{2,0^+} \rightarrow 3_{1,0^+}$	678786.359	1.91	6.54	3.88	7.87
$14_{1,0^-} \rightarrow 13_{1,0^-}$	681991.469	0.40	6.28	6.91	2.97

$A-CH_3OH$

Transition $J_{K,\,v^{\pi}}$	Frequency MHz	T_{mb} (K)	V_{lsr} (km s^{-1})	ΔV_{FWHM} (km s^{-1})	$\int T_{mb}dV$ (K km s^{-1})
$9_{3,0^+} \rightarrow 8_{2,0^+}$	686733.139	0.88	6.29	3.96	3.72
$9_{3,0^-} \rightarrow 8_{2,0^-}$	687225.614	0.95	6.56	4.69	4.73
$9_{1,0^+} \rightarrow 8_{0,0^+}$	719665.763	1.36	6.63	5.20	7.55
$5_{2,0^-} \rightarrow 4_{1,0^-}$	720442.766	1.48	6.45	3.88	6.11
$15_{0,0^+} \rightarrow 14_{0,0^+}$	723621.754	0.47	5.97	4.75	2.39
$9_{1,0^+} \rightarrow 8_{0,0^+}$	719665.580	1.46	6.71	4.62	7.17
$5_{2,0^-} \rightarrow 4_{1,0^-}$	720442.560	1.74	6.54	4.10	7.59
$15_{0,0^+} \rightarrow 14_{0,0^+}$	723620.678	0.57	6.42	6.12	3.70
$15_{2,0^-} \rightarrow 14_{2,0^-}$	724341.729	0.26	8.52	5.68	1.57
$5_{2,0^+} \rightarrow 4_{1,0^+}$	728863.716	1.84	6.49	4.26	8.34
$4_{3,0^+} \rightarrow 4_{1,0^-}$	730500.620	0.27	6.59	5.86	1.68
$15_{1,0^-} \rightarrow 14_{1,0^-}$	730520.329	0.38	6.66	5.07	2.05
$10_{3,0^+} \rightarrow 9_{2,0^+}$	734895.063	0.69	6.50	5.12	3.77
$10_{3,0^-} \rightarrow 9_{2,0^-}$	735674.315	0.75	6.48	4.98	3.96
$10_{1,0^+} \rightarrow 9_{0,0^+}$	763953.800	1.02	6.77	5.51	6.00
$6_{2,0^-} \rightarrow 5_{1,0^-}$	766711.663	1.34	6.48	3.76	5.39
$16_{1,0^-} \rightarrow 15_{1,0^-}$	779006.308	0.57	7.94	4.23	2.58
$6_{2,0^+} \rightarrow 5_{1,0^+}$	779381.813	1.54	6.43	4.32	7.11
$11_{3,0^+} \rightarrow 10_{2,0^+}$	783002.744	0.57	6.59	4.08	2.48
$11_{3,0^-} \rightarrow 10_{2,0^-}$	784178.534	0.47	6.55	4.82	2.41
$11_{1,0^+} \rightarrow 10_{0,0^+}$	807866.571	0.74	6.77	5.24	4.15
$7_{2,0^-} \rightarrow 6_{1,0^-}$	812551.631	1.08	6.51	4.39	5.07
$4_{4,0^-} \rightarrow 3_{3,0^-}$	829891.720	0.86	6.88	4.55	4.15
$7_{2,0^+} \rightarrow 6_{1,0^+}$	830351.195	1.19	6.34	4.19	5.30
$12_{3,0^+} \rightarrow 11_{2,0^+}$	831048.062	0.40	5.91	4.36	1.86
$12_{3,0^-} \rightarrow 11_{2,0^-}$	832755.306	0.43	6.44	5.28	2.43
$12_{1,0^+} \rightarrow 11_{0,0^+}$	851415.120	0.80	6.99	4.69	3.98
$8_{2,0^-} \rightarrow 7_{1,0^-}$	857960.158	0.80	6.64	3.77	3.20
$18_{0,0^+} \rightarrow 17_{0,0^+}$	867330.798	0.20	5.58	8.22	1.77
$5_{4,0^+} \rightarrow 4_{3,0^+}$	878227.107	0.76	6.79	4.47	3.60
$13_{3,0^+} \rightarrow 12_{2,0^+}$	879015.017	0.34	6.30	5.92	2.12
$13_{3,0^-} \rightarrow 12_{2,0^-}$	881420.967	0.34	6.86	6.59	2.38
$8_{2,0^+} \rightarrow 7_{1,0^+}$	881783.471	0.99	6.52	4.50	4.75
$13_{1,0^+} \rightarrow 12_{0,0^+}$	894614.921	0.50	6.75	4.70	2.50
$13_{1,0^+} \rightarrow 12_{0,0^+}$	894614.921	0.50	6.75	4.70	2.50
$9_{2,0^-} \rightarrow 8_{1,0^-}$	902936.659	0.59	6.40	5.25	3.29
$6_{4,0^+} \rightarrow 5_{3,0^+}$	926555.197	0.57	6.98	5.33	3.26
$14_{3,0^+} \rightarrow 13_{2,0^+}$	926896.631	0.26	5.95	5.89	1.62
$14_{3,0^-} \rightarrow 13_{2,0^-}$	930200.611	0.33	6.23	4.87	1.73
$9_{2,0^+} \rightarrow 8_{1,0^+}$	933694.545	0.73	6.45	4.59	3.55
$14_{1,0^+} \rightarrow 13_{0,0^+}$	937479.545	0.44	6.64	5.75	2.70
$7_{4,0^-} \rightarrow 6_{3,0^-}$	974878.742	0.58	6.37	6.39	3.93

$A\text{–}CH_3OH$

Transition $J_{K,\,v^{\pi}}$	Frequency MHz	T_{mb} (K)	V_{lsr} (km s^{-1})	ΔV_{FWHM} (km s^{-1})	$\int T_{mb}dV$ (K km s^{-1})
$10_{2,0^+} \rightarrow 9_{1,0^+}$	986100.370	0.73	6.22	5.11	3.98
$8_{4,0^+} \rightarrow 7_{3,0^+}$	1023196.727	0.65	7.15	4.35	2.99
				Total flux:	483.19

$E\text{–}CH_3OH$

Transition $J_{K,\,v}$	Frequency MHz	T_{mb} (K)	V_{lsr} (km s^{-1})	ΔV_{FWHM} (km s^{-1})	$\int T_{mb}dV$ (K km s^{-1})
$10_{1,1} \rightarrow 9_{1,1}$	482217.842	0.19	6.35	2.38	0.48
$10_{0,0} \rightarrow 9_{0,0}$	482283.126	0.92	6.38	3.75	3.68
$10_{-1,0} \rightarrow 9_{-1,0}$	482959.736	1.78	6.39	3.93	7.47
$10_{-4,0} \rightarrow 9_{-4,0}$	483472.797	0.21	6.81	4.57	1.00
$10_{1,0} \rightarrow 9_{1,0}$	483687.097	0.69	6.50	3.89	2.87
$10_{2,0} \rightarrow 9_{2,0}$	484023.818	0.83	6.59	4.50	3.97
$10_{-2,0} \rightarrow 9_{-2,0}$	484072.125	0.41	6.78	5.00	2.16
$7_{0,0} \rightarrow 6_{-1,0}$	495173.842	1.52	6.55	3.86	6.26
$14_{0,0} \rightarrow 13_{1,0}$	496922.440	0.13	8.20	2.22	0.30
$7_{1,0} \rightarrow 6_{0,0}$	504294.531	1.62	6.44	3.58	6.16
$11_{1,0} \rightarrow 10_{2,0}$	506153.776	0.24	6.58	5.06	1.27
$10_{2,0} \rightarrow 9_{1,0}$	509564.943	0.92	6.81	5.24	5.12
$2_{-2,0} \rightarrow 1_{-1,0}$	520179.579	1.50	6.70	4.09	6.53
$14_{-1,0} \rightarrow 13_{0,0}$	523275.245	0.36	6.46	4.92	1.88
$13_{-4,0} \rightarrow 13_{-3,0}$	524270.011	0.09	6.60	3.14	0.30
$12_{-4,0} \rightarrow 12_{-3,0}$	524384.143	0.09	7.30	2.49	0.25
$10_{-4,0} \rightarrow 10_{-3,0}$	524584.054	0.10	6.17	2.97	0.31
$9_{-4,0} \rightarrow 9_{-3,0}$	524666.995	0.17	6.56	5.66	1.05
$8_{-4,0} \rightarrow 8_{-3,0}$	524740.757	0.22	6.69	6.08	1.45
$7_{-4,0} \rightarrow 7_{-3,0}$	524806.056	0.20	6.38	4.99	1.07
$6_{-4,0} \rightarrow 6_{-3,0}$	524861.993	0.23	6.36	3.93	0.97
$5_{-4,0} \rightarrow 5_{-3,0}$	524908.768	0.24	6.68	4.03	1.05
$4_{-4,0} \rightarrow 4_{-3,0}$	524948.069	0.17	6.54	3.27	0.59
$4_{-3,0} \rightarrow 5_{-2,0}$	525056.316	0.08	6.67	2.05	0.18
$15_{3,0} \rightarrow 15_{2,0}$	527172.530	0.09	6.39	9.31	0.89
$13_{3,0} \rightarrow 13_{2,0}$	528179.132	0.14	5.93	7.30	1.07
$11_{3,0} \rightarrow 11_{2,0}$	529142.627	0.17	7.32	4.78	0.87
$10_{3,0} \rightarrow 10_{2,0}$	529540.993	0.23	6.59	6.03	1.49

$E-CH_3OH$

Transition $J_{K,\,v}$	Frequency MHz	T_{mb} (K)	V_{lsr} (km s^{-1})	ΔV_{FWHM} (km s^{-1})	$\int T_{mb}dV$ (K km s^{-1})
$9_{3,0} \rightarrow 9_{2,0}$	529867.102	0.22	6.78	5.36	1.24
$8_{3,0} \rightarrow 8_{2,0}$	530123.524	0.38	6.87	5.42	2.20
$11_{0,0} \rightarrow 10_{0,0}$	530184.874	0.68	6.60	4.64	3.34
$7_{3,0} \rightarrow 7_{2,0}$	530316.837	0.44	6.64	4.89	2.31
$6_{3,0} \rightarrow 6_{2,0}$	530455.522	0.57	6.52	4.12	2.49
$5_{3,0} \rightarrow 5_{2,0}$	530549.772	0.58	6.69	4.61	2.86
$4_{3,0} \rightarrow 4_{2,0}$	530611.056	0.58	6.55	4.34	2.68
$3_{3,0} \rightarrow 3_{2,0}$	530647.070	0.51	7.07	5.00	2.73
$11_{-1,0} \rightarrow 10_{-1,0}$	531080.098	1.39	6.51	4.34	6.42
$11_{1,0} \rightarrow 10_{1,0}$	532032.124	0.53	6.59	5.21	2.95
$11_{3,0} \rightarrow 10_{3,0}$	532070.164	0.14	6.44	3.29	0.50
$11_{2,0} \rightarrow 10_{2,0}$	532467.350	0.71	6.38	4.64	3.49
$11_{-2,0} \rightarrow 10_{-2,0}$	532567.787	0.40	6.43	5.23	2.25
$8_{0,0} \rightarrow 7_{-1,0}$	543076.994	1.43	6.55	4.49	6.82
$8_{1,0} \rightarrow 7_{0,0}$	553147.287	1.22	6.42	3.60	4.70
$12_{1,0} \rightarrow 11_{2,0}$	554056.561	0.19	6.38	5.91	1.18
$11_{2,0} \rightarrow 10_{1,0}$	558345.869	0.56	6.31	4.31	2.55
$11_{2,0} \rightarrow 10_{1,0}$	558345.385	0.62	6.57	4.52	2.98
$3_{-2,0} \rightarrow 2_{-1,0}$	568566.841	1.62	6.60	4.28	7.39
$8_{4,0} \rightarrow 9_{3,0}$	570620.266	0.12	6.27	3.58	0.45
$15_{-1,0} \rightarrow 14_{0,0}$	572900.168	0.30	6.24	5.00	1.59
$3_{-3,0} \rightarrow 4_{-2,0}$	573472.349	0.11	6.25	5.04	0.58
$12_{0,0} \rightarrow 11_{0,0}$	578007.584	0.52	6.40	4.58	2.52
$12_{-1,0} \rightarrow 11_{-1,0}$	579151.934	0.98	6.51	4.41	4.61
$12_{-4,0} \rightarrow 11_{-4,0}$	580059.906	0.13	6.28	5.39	0.73
$12_{1,0} \rightarrow 11_{1,0}$	580369.393	0.41	6.59	4.47	1.93
$12_{3,0} \rightarrow 11_{3,0}$	580443.250	0.18	6.51	5.06	0.98
$12_{2,0} \rightarrow 11_{2,0}$	580903.846	0.56	6.41	4.85	2.88
$12_{-2,0} \rightarrow 11_{-2,0}$	581092.641	0.33	6.51	4.82	1.67
$9_{0,0} \rightarrow 8_{-1,0}$	590791.902	1.11	6.51	4.06	4.80
$13_{1,0} \rightarrow 12_{2,0}$	601850.014	0.14	6.53	5.92	0.85
$9_{1,0} \rightarrow 8_{0,0}$	602234.232	1.04	6.43	4.02	4.44
$12_{2,0} \rightarrow 11_{1,0}$	607217.094	0.40	6.41	5.21	2.20
$4_{-2,0} \rightarrow 3_{-1,0}$	616980.698	1.54	6.60	4.11	6.72
$7_{-1,1} \rightarrow 6_{2,1}$	618720.048	0.07	4.93	6.27	0.49
$16_{-1,0} \rightarrow 15_{0,0}$	622775.503	0.26	6.14	5.00	1.37
$13_{0,0} \rightarrow 12_{0,0}$	625750.662	0.39	6.42	5.42	2.26
$13_{-1,0} \rightarrow 12_{-1,0}$	627171.602	0.75	6.47	4.92	3.91
$13_{1,0} \rightarrow 12_{1,0}$	628698.275	0.28	6.10	4.99	1.48
$13_{3,0} \rightarrow 12_{3,0}$	628817.622	0.26	6.28	4.00	1.11
$13_{2,0} \rightarrow 12_{2,0}$	629322.361	0.48	6.67	5.00	2.57
$13_{-2,0} \rightarrow 12_{-2,0}$	629653.222	0.29	6.32	7.83	2.45

$E{-}CH_3OH$

Transition	Frequency	T_{mb}	V_{lsr}	ΔV_{FWHM}	$\int T_{mb}dV$
$J_{K,\,v}$	MHz	(K)	(km s^{-1})	(km s^{-1})	(K km s^{-1})
$13_{-1,0} \rightarrow 12_{-1,0}$	627171.352	0.64	6.59	4.38	2.96
$13_{2,0} \rightarrow 12_{2,0}$	629321.481	0.33	7.09	6.00	2.09
$13_{-2,0} \rightarrow 12_{-2,0}$	629651.721	0.26	7.03	5.15	1.44
$10_{0,0} \rightarrow 9_{-1,0}$	638280.272	0.86	6.71	4.42	4.04
$10_{1,0} \rightarrow 9_{0,0}$	651618.525	0.79	6.46	4.59	3.84
$13_{2,0} \rightarrow 12_{1,0}$	656166.612	0.75	8.07	6.40	5.10
$5_{-2,0} \rightarrow 4_{-1,0}$	665443.128	1.53	6.68	4.25	6.90
$17_{-1,0} \rightarrow 16_{0,0}$	672901.707	0.26	7.37	6.72	1.83
$14_{0,0} \rightarrow 13_{0,0}$	673416.970	0.37	6.55	4.86	1.89
$14_{-1,0} \rightarrow 13_{-1,0}$	675135.725	0.58	6.47	6.01	3.73
$3_{3,0} \rightarrow 2_{2,0}$	675773.950	0.93	6.75	4.92	4.85
$14_{1,0} \rightarrow 13_{1,0}$	677011.822	0.31	7.45	8.32	2.73
$14_{2,0} \rightarrow 13_{2,0}$	677711.907	0.44	6.05	4.86	2.26
$14_{-2,0} \rightarrow 13_{-2,0}$	678253.976	0.22	6.38	2.23	0.53
$11_{0,0} \rightarrow 10_{-1,0}$	685505.143	0.68	6.96	5.87	4.23
$14_{2,0} \rightarrow 13_{1,0}$	705183.785	0.30	6.39	6.25	1.98
$6_{-2,0} \rightarrow 5_{-1,0}$	713983.433	1.17	6.59	4.12	5.13
$6_{-2,0} \rightarrow 5_{-1,0}$	713983.433	1.17	6.59	4.12	5.13
$4_{-4,0} \rightarrow 3_{-3,0}$	718436.930	1.08	6.70	3.99	4.60
$15_{0,0} \rightarrow 14_{0,0}$	721012.727	0.24	6.16	5.89	1.50
$15_{-1,0} \rightarrow 14_{-1,0}$	723040.582	0.47	6.92	5.43	2.71
$4_{3,0} \rightarrow 3_{2,0}$	724122.891	0.75	6.47	5.70	4.54
$4_{-4,0} \rightarrow 3_{-3,0}$	718437.011	1.21	6.67	4.81	6.18
$15_{0,0} \rightarrow 14_{0,0}$	721012.252	0.28	6.36	4.84	1.44
$15_{-1,0} \rightarrow 14_{-1,0}$	723041.882	0.47	6.38	8.06	4.03
$18_{-1,0} \rightarrow 17_{0,0}$	723280.153	0.24	6.91	3.69	0.95
$4_{3,0} \rightarrow 3_{2,0}$	724122.104	1.00	6.79	5.31	5.64
$15_{2,0} \rightarrow 14_{2,0}$	726054.078	0.20	6.16	5.20	1.13
$15_{-2,0} \rightarrow 14_{-2,0}$	726901.505	0.26	6.06	5.36	1.47
$12_{0,0} \rightarrow 11_{-1,0}$	732433.683	0.54	6.42	5.12	2.95
$12_{1,0} \rightarrow 11_{0,0}$	751552.499	0.48	6.42	5.84	3.01
$7_{-2,0} \rightarrow 6_{-1,0}$	762636.474	0.96	6.66	4.43	4.51
$12_{-3,0} \rightarrow 12_{-2,0}$	763882.502	0.27	7.13	5.33	1.53
$11_{-3,0} \rightarrow 11_{-2,0}$	764817.428	0.25	4.78	8.33	2.18
$10_{-3,0} \rightarrow 10_{-2,0}$	765514.838	0.23	6.11	4.07	0.98
$9_{-3,0} \rightarrow 9_{-2,0}$	766028.919	0.34	6.74	5.20	1.88
$8_{-3,0} \rightarrow 8_{-2,0}$	766396.969	0.49	6.58	5.86	3.04
$7_{-3,0} \rightarrow 7_{-2,0}$	766648.472	0.52	6.62	4.53	2.49
$5_{-4,0} \rightarrow 4_{-3,0}$	766761.676	1.08	6.55	3.32	3.81
$6_{-3,0} \rightarrow 6_{-2,0}$	766811.563	0.52	6.56	2.56	1.41
$5_{-3,0} \rightarrow 5_{-2,0}$	766908.513	0.58	6.81	4.16	2.58
$4_{-3,0} \rightarrow 4_{-2,0}$	766961.537	0.61	6.35	3.36	2.19

$E{-}CH_3OH$

Transition $J_{K,\,v}$	Frequency MHz	T_{mb} (K)	V_{lsr} (km s^{-1})	ΔV_{FWHM} (km s^{-1})	$\int T_{mb}dV$ (K km s^{-1})
$3_{-3,0} \rightarrow 3_{-2,0}$	766983.751	0.49	6.37	3.06	1.59
$5_{3,0} \rightarrow 4_{2,0}$	772453.477	0.70	7.15	7.09	5.26
$16_{2,0} \rightarrow 15_{2,0}$	774333.576	0.27	6.94	5.08	1.44
$13_{0,0} \rightarrow 12_{-1,0}$	779030.267	0.46	7.18	6.03	2.93
$8_{-2,0} \rightarrow 7_{-1,0}$	811444.675	0.72	6.95	6.01	4.59
$6_{-4,0} \rightarrow 5_{-3,0}$	815071.719	0.91	6.58	4.34	4.19
$6_{3,0} \rightarrow 5_{2,0}$	820764.657	0.52	6.18	4.42	2.45
$17_{1,0} \rightarrow 16_{1,0}$	821869.910	0.21	6.81	4.37	0.98
$17_{2,0} \rightarrow 16_{2,0}$	822542.664	0.27	6.20	6.00	1.72
$17_{-2,0} \rightarrow 16_{-2,0}$	824348.090	0.22	5.05	6.00	1.40
$14_{0,0} \rightarrow 13_{-1,0}$	825277.515	0.27	6.53	4.99	1.44
$8_{5,0} \rightarrow 8_{4,0}$	834839.837	0.20	6.09	4.03	0.84
$14_{1,0} \rightarrow 13_{0,0}$	853505.478	0.33	6.62	7.20	2.49
$13_{4,0} \rightarrow 14_{2,0}$	855152.868	0.30	4.19	3.89	1.25
$9_{-2,0} \rightarrow 8_{-1,0}$	860459.441	0.54	6.95	5.54	3.16
$7_{-4,0} \rightarrow 6_{-3,0}$	863365.781	0.70	6.71	5.19	3.89
$18_{0,0} \rightarrow 17_{0,0}$	863431.486	0.25	6.88	3.91	1.04
$7_{3,0} \rightarrow 6_{2,0}$	869039.059	0.63	6.60	5.18	3.48
$18_{-3,0} \rightarrow 17_{-3,0}$	869600.910	0.18	7.80	1.87	0.36
$10_{-2,0} \rightarrow 9_{-1,0}$	909738.072	0.43	6.86	4.66	2.12
$19_{0,0} \rightarrow 18_{0,0}$	910814.415	0.23	4.83	6.00	1.47
$8_{-4,0} \rightarrow 7_{-3,0}$	911643.691	0.58	6.49	4.47	2.75
$3_{-3,0} \rightarrow 2_{-2,0}$	912109.651	0.86	6.63	5.05	4.65
$16_{0,0} \rightarrow 15_{-1,0}$	916652.389	0.27	6.85	7.79	2.23
$8_{3,0} \rightarrow 7_{2,0}$	917269.034	0.47	7.31	4.94	2.49
$4_{-3,0} \rightarrow 3_{-2,0}$	960473.039	0.75	6.40	5.25	4.19
$9_{3,0} \rightarrow 8_{2,0}$	965448.164	0.43	7.02	5.35	2.44
$5_{-3,0} \rightarrow 4_{-2,0}$	1008811.829	0.51	7.10	5.51	3.01
$6_{-3,0} \rightarrow 5_{-2,0}$	1057119.879	0.62	6.39	5.58	3.68
$6_{-3,0} \rightarrow 5_{-2,0}$	1057118.804	0.60	6.69	4.69	3.02
$7_{-3,0} \rightarrow 6_{-2,0}$	1105371.685	0.42	6.65	4.80	2.17
$5_{3,0} \rightarrow 4_{-1,0}$	1119822.428	0.45	7.40	7.00	3.39
$8_{-3,0} \rightarrow 7_{-2,0}$	1153552.098	0.66	6.30	4.53	3.20
				Total flux:	387.08

Table B.2: *Summary of the observed water transitions. Table provided by kind permission of Nagy et. al. 2012.*

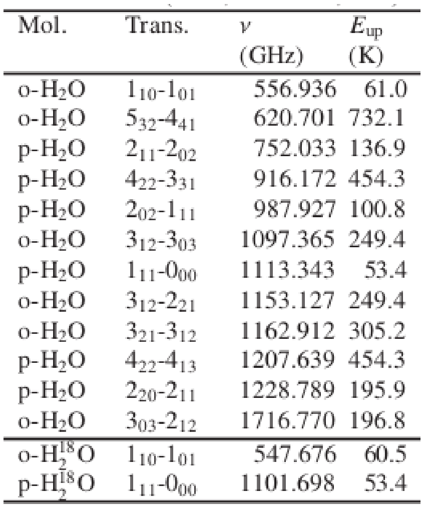

Mol.	Trans.	ν (GHz)	E_{up} (K)
o-H_2O	1_{10}-1_{01}	556.936	61.0
o-H_2O	5_{32}-4_{41}	620.701	732.1
p-H_2O	2_{11}-2_{02}	752.033	136.9
p-H_2O	4_{22}-3_{31}	916.172	454.3
p-H_2O	2_{02}-1_{11}	987.927	100.8
o-H_2O	3_{12}-3_{03}	1097.365	249.4
p-H_2O	1_{11}-0_{00}	1113.343	53.4
o-H_2O	3_{12}-2_{21}	1153.127	249.4
o-H_2O	3_{21}-3_{12}	1162.912	305.2
p-H_2O	4_{22}-4_{13}	1207.639	454.3
p-H_2O	2_{20}-2_{11}	1228.789	195.9
o-H_2O	3_{03}-2_{12}	1716.770	196.8
o-$H_2^{18}O$	1_{10}-1_{01}	547.676	60.5
p-$H_2^{18}O$	1_{11}-0_{00}	1101.698	53.4

Table B.3: *H_2O line parameters based on the average spectrum of H and V polarizations. Table provided by kind permission of Nagy et. al. 2012.*

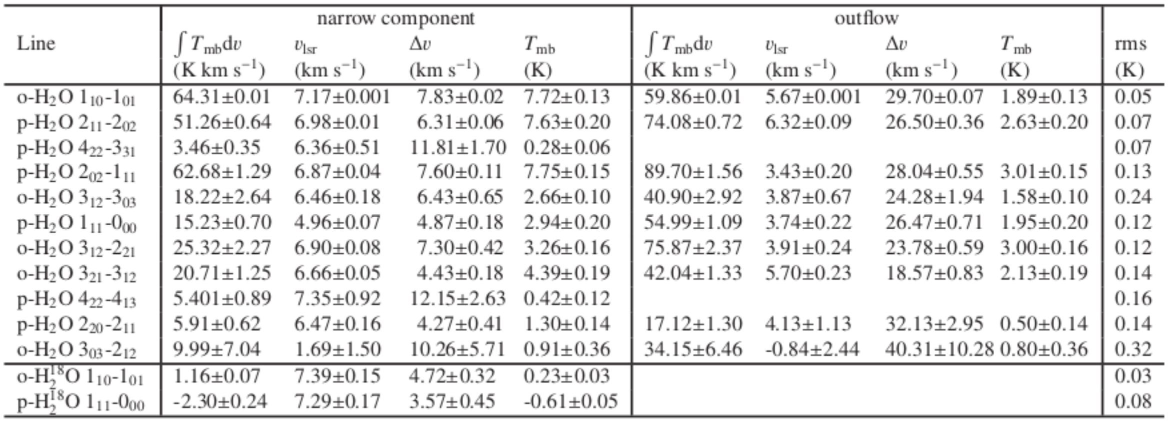

Line	narrow component				outflow				rms
	$\int T_{mb}dv$ (K km s^{-1})	v_{lsr} (km s^{-1})	Δv (km s^{-1})	T_{mb} (K)	$\int T_{mb}dv$ (K km s^{-1})	v_{lsr} (km s^{-1})	Δv (km s^{-1})	T_{mb} (K)	(K)
o-H_2O 1_{10}-1_{01}	64.31±0.01	7.17±0.001	7.83±0.02	7.72±0.13	59.86±0.01	5.67±0.001	29.70±0.07	1.89±0.13	0.05
p-H_2O 2_{11}-2_{02}	51.26±0.64	6.98±0.01	6.31±0.06	7.63±0.20	74.08±0.72	6.32±0.09	26.50±0.36	2.63±0.20	0.07
p-H_2O 4_{22}-3_{31}	3.46±0.35	6.36±0.51	11.81±1.70	0.28±0.06					0.07
p-H_2O 2_{02}-1_{11}	62.68±1.29	6.87±0.04	7.60±0.11	7.75±0.15	89.70±1.56	3.43±0.20	28.04±0.55	3.01±0.15	0.13
o-H_2O 3_{12}-3_{03}	18.22±2.64	6.46±0.18	6.43±0.65	2.66±0.10	40.90±2.92	3.87±0.67	24.28±1.94	1.58±0.10	0.24
p-H_2O 1_{11}-0_{00}	15.23±0.70	4.96±0.07	4.87±0.18	2.94±0.20	54.99±1.09	3.74±0.22	26.47±0.71	1.95±0.20	0.12
o-H_2O 3_{12}-2_{21}	25.32±2.27	6.90±0.08	7.30±0.42	3.26±0.16	75.87±2.37	3.91±0.24	23.78±0.59	3.00±0.16	0.12
o-H_2O 3_{21}-3_{12}	20.71±1.25	6.66±0.05	4.43±0.18	4.39±0.19	42.04±1.33	5.70±0.23	18.57±0.83	2.13±0.19	0.14
p-H_2O 4_{22}-4_{13}	5.401±0.89	7.35±0.92	12.15±2.63	0.42±0.12					0.16
p-H_2O 2_{20}-2_{11}	5.91±0.62	6.47±0.16	4.27±0.41	1.30±0.14	17.12±1.30	4.13±1.13	32.13±2.95	0.50±0.14	0.14
o-H_2O 3_{03}-2_{12}	9.99±7.04	1.69±1.50	10.26±5.71	0.91±0.36	34.15±6.46	-0.84±2.44	40.31±10.28	0.80±0.36	0.32
o-$H_2^{18}O$ 1_{10}-1_{01}	1.16±0.07	7.39±0.15	4.72±0.32	0.23±0.03					0.03
p-$H_2^{18}O$ 1_{11}-0_{00}	-2.30±0.24	7.29±0.17	3.57±0.45	-0.61±0.05					0.08